Doctoral Thesis ETH No. 16580

INVESTIGATION OF DEPOSITION AND ADSORPTION ON SOLID-LIQUID INTERFACES THROUGH OPTICAL WAVEGUIDE LIGHTMODE SPECTROSCOPY

A dissertation submitted to the
SWISS FEDERAL INSTITUTE OF TECHNOLOGY ZURICH
for degree of
Doctor of Technical Sciences

presented by

Marek Kroslak
MSc. Slovak Technical University, Bratislava 2000
born on December 5, 1976
citizen of Slovakia

accepted on the recommendation of

Prof. Dr. M. Morbidelli, examiner
Dr. J. Sefcik, co-examiner
Dr. R. Liardon, co-examiner

Zurich 2006

Doctoral Thesis ETH No. 16580

INVESTIGATION OF DEPOSITION AND ADSORPTION ON SOLID-LIQUID INTERFACES THROUGH OPTICAL WAVEGUIDE LIGHTMODE SPECTROSCOPY

A dissertation submitted to the
SWISS FEDERAL INSTITUTE OF TECHNOLOGY ZURICH
for degree of
Doctor of Technical Sciences

presented by

Marek Kroslak
MSc. Slovak Technical University, Bratislava 2000
born on December 5, 1976
citizen of Slovakia

accepted on the recommendation of

Prof. Dr. M. Morbidelli, examiner
Dr. J. Sefcik, co-examiner
Dr. R. Liardon, co-examiner

Zurich 2006

Abstract

Deposition of dissolved or suspended material from liquids at solid surfaces is present in various applications occurring not only in chemical process technologies, but also in many food, biomedical, environmental and mineral processing industries. Control of deposition phenomena through appropriate design of surface properties has been subject of much interest in recent years. For example, desire to properly control interfacial interactions governing the deposition is a long-lasting aim in medicine, where fouling resistant or deposition selective surfaces are of crucial importance for biocompatibility among various artificial surfaces and natural tissues. Sensors based on reflectance techniques, such as optical waveguide lightmode spectroscopy (OWLS), are among primary tools for studying deposition phenomena at nanometer scale and in real time, allowing one to obtain detailed insight into mechanisms governing the deposition process.

The main focus of the previous research work on deposition of biomolecules and biopolymers was on control of deposition at ambient temperature through various surface modifications. However, only very limited investigations of deposition at the elevated temperatures have been made. The aim of this work is to gain further understanding into the early stages of deposition occurring during the thermal treatment of various biologically based liquid systems, which are subject of fouling in industrial evaporators. OWLS was used as a tool to monitor and quantitatively characterize processes in early stages of deposition. Since many interactions among biomolecules are sensitive to temperature, the ability of OWLS to monitor deposition non-invasively, on-line at elevated temperatures brings novel insights into mechanisms of temperature driven deposition processes.

In the course of this work it was necessary first to understand the temperature response of the OWLS sensor in contact with electrolyte solutions and the stability of various surfaces at elevated temperatures. We also studied adsorption from electrolyte and surfactant solutions on variously modified surfaces at both ambient and elevated temperatures and we obtained measurements of corresponding adsorption and desorption kinetics as well as adsorption isotherms of simple model compounds representing liquid matrices of more complex biomolecular solutions.

β-lactoglobulin is the main protein in the milk whey solution and it is responsible for surface fouling in industrial evaporators during the milk thermal treatment. Kinetics of temperature driven deposition of β-lactoglobulin was measured over a wide range of temperatures, pH and ionic strengths. Activation energies of deposition were determined for pH between 5.5 and 7.4 and the observed trends were explained as resulting from interplay of denaturation and aggregation kinetics of β-lactoglobulin.

In the next part of this work we investigated temperature driven deposition from coffee extracts obtained by hot extraction of roasted coffee beans, containing a complex mixture of polysaccharides, melanoidines, proteins and organic acids. Such extracts cause intensive fouling in industrial evaporators which has significant effects on operating costs in production of soluble coffee, so that better understanding of the fouling mechanism could help to further optimize the evaporation process. Various surfaces were used to investigate the influence of the surface material on fouling process. Effects of the extract composition were examined over a wide range of temperatures and the measured activation energies indicated that different deposition mechanisms operate in concentrated and diluted extracts, respectively. This difference was also observed in bulk aggregation monitored by static light scattering. In addition to OWLS, we also used gravimetry to follow fouling processes over a longer time frame, where deposition rates observed by gravimetry were found to be in good agreement with those measured by OWLS at shorter deposition times.

Zusammenfassung

Die Ablagerung gelöster bzw. suspendierter Stoffe aus Flüssigkeiten an festen Oberflächen spielt in vielen Prozessen der chemischen sowie der Nahrungsmittel-, biomedizinischen, Umwelt- und mineralverarbeitenden Industrie eine wichtige Rolle. Besonderes Interesse galt in jüngerer Zeit der gezielten Beeinflussung von Ablagerungsvorgängen durch eine geeignete Gestaltung der Oberfläche. Beispielsweise ist die Biokompatibilität verschiedener künstlicher Oberflächen und natürlicher Gewebe entscheidend von der Resistenz gegen bzw. Selektivität für bestimmte Ablagerungen abhängig. Folglich ist man unter anderem in der Medizin seit langem bemüht, Wechselwirkungen von Akkumulationsvorgängen an Grenzflächen zu beherrschen. Echtzeitmessungen von Ablagerungsvorgängen im Nanometerbereich erlauben gezielte Einblicke in die Mechanismen von Ablagerungsvorgängen und sind mit Reflektionssensorik wie der Optical Waveguide Lightmode Spectroscopy (OWLS) möglich.

Den Schwerpunkt der vorliegenden Forschungsarbeit zur Ablagerung von Biomolekülen und Biopolymeren bildete die Charakterisierung der Ablagerung auf verschiedenen Oberflächen bei Umgebungstemperatur, weshalb nur wenige Untersuchungen bei erhöhter Temperatur durchgeführt wurden. In erster Linie sollte das Anfangsstadium von Ablagerungsprozessen erkundet werden, die bei thermischer Behandlung von Flüssigkeiten biologischen Ursprungs zu Verkrustungen in industriellen Verdampfern führen. OWLS diente als Online-Messwerkzeug zur quantitativen Charakterisierung des Anfangsstadiums solcher Prozesse. Da viele Wechselwirkungen zwischen Biomolekülen temperaturempfindlich sind, erlaubt die nicht-invasive Verfolgung von Ablagerungsvorgängen mittels OWLS neue Einblicke in die Mechanismen thermisch induzierter Ablagerungsprozesse.

Im Zuge dieser Arbeit war zuerst das Antwortverhalten des Sensors in Kontakt mit den eingesetzten Elektrolytlösungen und die Temperaturstabilität der verwendeten Oberflächen zu klären. Die Adsorption von Elektrolyten und Tensiden bezüglich der zu untersuchenden Oberflächen wurde sowohl bei Umgebungs- als auch bei erhöhter Temperatur studiert. Die entsprechenden Messungen lieferten neben den Adsorptionsisothermen auch die Kinetik der Adsorption und Desorption ausgewählter Modellkomponenten, die die Zusammensetzung der realen, mit Biomolekülen beladenen Lösungen repräsentieren sollten.

β-Lactoglobulin als Hauptbestandteil von Milchserum wird für Ablagerungen in industriellen Verdampfern bei der Milchverarbeitung verantwortlich gemacht. Die Kinetik der thermisch induzierten Ablagerung von β-Lactoglobulin wurde für einen weiten Bereich von Temperaturen, pH-Werten und Ionenstärken untersucht. Die im pH-Bereich von 5.5 bis 7.4 erhaltenen Aktivierungsenergien der Ablagerung wurden als Resultat des Zusammenspiels der Denaturierungs- und Aggregationskinetik von β-Lactoglobulin erklärt.

Ein weiterer Teil der Arbeit widmete sich der thermisch induzierten Ablagerung von Kaffeextrakten, welche ein komplexes Gemisch von Polysacchariden, Melanoidinen, Proteinen und organischen Säuren darstellen. Solche Extrakte gerösteter Kaffeebohnen rufen bei ihrer Verarbeitung zu löslichem Kaffee starke Verkrustungen in industriellen Verdampfern hervor. Daher kann ein besseres Verständnis der Ablagerungsmechanismen zur Optimierung des Trocknungsprozesses und der Betriebskosten beitragen. Verschiedene Oberflächen wurden eingesetzt, um deren Einfluss auf den Ablagerungsprozess zu untersuchen. Aktivierungsenergien wurden für verschiedene Extraktkonzentrationen in einem weiten Temperaturbereich ermittelt. Diese lassen darauf schliessen, dass unterschiedliche Ablagerungsmechanismen für konzentrierte bzw. verdünnte Extrakte vorherrschen, was durch Lichtstreuungsmessungen der Volumenaggregation bestätigt werden konnte. Die mittels Gravimetrie über einen langen Zeitbereich aufgenommenen Ablagerungsmengen korrespondierten gut mit den durch OWLS bestimmten initialen Ablagerungsraten.

Acknowledgement

At the end of all these years I spend here at the ETH, I have now opportunity to address my deep thank to all my colleagues and friends who have contributed to this thesis on scientific and on a personal level.

First of all, I would like to thank Prof. Massimo Morbidelli not only for giving me the opportunity to pursue my PhD in this institute, but also for his continuous encouragements, trust, critical reviews and scientific freedom during the project.
I would like to thank Dr. Jan Sefcik for introducing me in to the world of international science, for his constant interest in my project, many hours of discussions, as well as for his support.
Special thank goes to Dr. Remy Liardon from Nestlé Product Technology Centre for co-referencing my thesis and for generous financial support making this project possible. At this place I have to mention Dr. Valerie Leloup from the same company for her collaboration on the project.
I am very grateful for helpful discussion with ″OWLS master″ Prof. Janos Voros for his advices, suggestions, patient explanations, new ideas and material supplies.
Dr. Miroslav Soos for brain-storming discussions, helpfulness and many useful suggestions.
Dr. Frank Krumleich for SEM. Roland Mader for making the gravimetry channel.
Next I would like to thank my colleagues from the group for help with various, specially my lab-mates Cornelius Gauer, Lyonel Ehrl for having nice working environment and Andrea Vaccaro for solving any computer related tasks.

Finally, I would like to thank my dear wife Ivanka. I also deeply thank my family for their long-distance support from Slovakia.

Contents

List of Figures

List of Tables

1 Introduction

1.1 Outline of the Thesis

The original motivation of this work is the need of understanding the mechanisms underlying surface fouling during the concentration by evaporation of plant extracts, which is rather common procedure in the food industry. The term fouling refers to the undesirable formation of inorganic and/or organic deposits on surfaces. These deposits can lead to various problems such as contamination of the products, reduction of process efficiency, contamination from detergents used for cleaning, pipeline plugging, heat and mass transfer limitations and decrease in mixing efficiency. In addition the process has to be interrupted on a regular basis in order to remove the deposits. This leads to additional costs and losses in production. An overview of the possible occurrence and the consequent effects of fouling on various industrial processes is given in Table 1. It is also worth mentioning that biofilms created during fouling provide the ideal conditions for the growth of various microorganisms. For all these reasons it is needed to better understand the underlying mechanism of fouling so as to prevent or at least to strongly reduce it.

The main objective of this thesis is to investigate the early stages of deposition on various surfaces through Optical Waveguide Lightmode Spectroscopy. Special attention was given to the temperature driven deposition from various biological suspensions containing proteinaceous substances. The literature on the investigation of deposition and adsorption at solid-liquid interfaces by optical methods is reviewed in the section 1.4.1.1. Most of them refer to single layer deposition at ambient temperature. On the other hand the deposition during concentration by evaporation processes is temperature driven and leads to multiple layers. These are the aspects on which this work is focused.

Table 1. *Effects and occurrence of fouling films formation on different processes.*

Process → Result	Concerns
Effect: heat transfer reduction	
Biofilm formation on condenser tubes and cooling tower fill material → energy losses	Power industry, navy, chemical process industry, solar energy systems, food processes
Effect: increase in fluid frictional resistance	
Biofilm formation in water and wastewater conduits as well as condenser and heat exchange tubes. Results in increased power consumption for pumped systems or reduced capacity in gravity systems → energy losses Biofilm formation on ship hulls causing increased fuel consumption → energy losses	Municipal utilities, power industry, navy, chemical process industry, solar energy systems
Effect: equipment performance reduction	
Biofilm formation on remote sensors, submarine periscopes, sight glasses, etc. → reduced effectiveness	Navy, deep water data acquisition
Effect: mass transfer and chemical transformations	
Accelerated corrosion due to processes in the lower layers of the biofilm → material deterioration in metal condenser tubes, sewage conduits, and cooling tower fill	Municipal utilities, power industry, chemical process industry, solar energy systems
Detachment of microorganisms from biofilms in cooling towers → releases pathogenic organisms	Food processing, public health
Biofilm formation and detachment in drinking water distribution systems → changes water quality in distribution system	Water delivery network, public health
Biofilm formation on teeth → dental plaque and caries	Dental health
Attachment of microbial cells to animal tissue → disease of lungs, intestinal tract, and urinary tract, transplantate rejection	Human health
Extraction and oxidation of organic and inorganic compounds from water and wastewater → reduced pollutant load	Wastewater and water treatment
Biofilm formation in industrial production processes → reduction of product quality	Pulp, paper and food processing industry
Biofilm accumulation reduces effectiveness of ion exchange membrane process used for high quality water treatment → increased operating costs	Desalination

Chapter 1 summarizes the general principles governing the deposition processes in relation to the universal principles valid in colloidal science. Special attention is dedicated towards specific features of biological mixtures. Next the various experimental methods used to study surface interactions and deposition are reviewed with specific reference to the ones used in this work.

In chapter 2 an experimental study of sodium dodecyl sulfate (SDS) adsorption on water-polystyrene interface under a wide range of temperatures is discussed. Although SDS adsorption on polystyrene (PS) in aqueous solution at ambient temperature is well investigated in the literature, little information is available for higher temperatures and ionic strengths, although these conditions are very frequent in industrial applications. Two hydrophobic polymer films were considered: polystyrene and Teflon® AF. One relevant aspect of this study with respect to assessing the adopted experimental technique is that surfactant molecules represent the lower resolution limit.

The effect of the concentration of electrolytes on sensor response is studied in chapter 3. It is shown that porous oxide waveguides exhibit a strong optical response when exposed to electrolyte solutions. This response is consistent with oxide surface charging due to changes in ionic strength and pH of the solution in contact with the waveguide. The main contribution to the polarization density comes from highly polarized negatively charged oxygen ions, corresponding to the charge density of de-protonized sites at the internal surface of the porous waveguide.

The remaining part of the thesis is focused on the study of the deposition behavior from proteinaceous solutions. In chapter 4 temperature driven deposition of a model protein β-lactoglobulin is investigated for various temperature, pH and ionic strength values. The effect of temperature on sensor response as well as the deposition of protein on waveguide surface can be determined rather easily, since the model system is not affected by the presence of electrolyte effect. The protein deposition kinetics at elevated temperature has been measured using the developed technique on-line and in-situ.

In chapter 5 the early stages of the temperature driven deposition from an industrial coffee extract was studied. Due to its nature this is a very complex sample and the sensor response to the presence of electrolytes can be very significant. An experimental procedure is developed

in order to properly handle such systems and to obtain reliable deposition rates. The data obtained with the optical sensor in the early stages of the deposition process have been found to be in agreement with gravimetry measurements performed independently and over a longer period of time. Some important aspects of the early deposition mechanism were revealed and a comprehensive study is reported on the behavior of the extract and the model protein, with respect to both deposition and aggregation.

1.2 Adsorption and Deposition

Adsorption is a process that takes place, when molecules (adsorbate) accumulate on the solid surface (adsorbent) forming a molecular film. The type of the bound depends on the species involved. Two general classes can be distinguished: physisorption and chemisorption.

Physisorption, also called deposition further on, can be characterized by weak intermolecular interactions between colloids, low temperatures characteristic for the processes, low activation energies (below 20kJ.mol^{-1}) and creation of multilayers.

On the other hand, the chemisorption is a type of adsorption where molecules are adhered via chemical bonds. Next to the strong chemicals bonds, it can also be characterized by higher temperature of the process, high activation energies (~400kJ.mol^{-1}) and creation of monolayer.

Deposition (physical adsorption) is the process whereby colloidal particles are transported to a surface, where they become attached. In fact, deposition has several features in common with aggregation and can be considered as an extreme case of heterogeneous aggregation. Aggregation involves the association of particles to form clusters. An important feature of deposition which makes it different from aggregation is that particles, which are stable in liquid bulk, may readily deposit on a surface of a different type, because of missing electrostatic repulsion. For instance, most of the proteinaceous suspensions in contact with various surfaces spontaneously deposit and create primary coverage. As soon as the primary layer covers the surface, any further deposition is prevented by the same repulsion as acting between the colloids in a bulk. Overcoming the stabilizing repulsion forces and thus system destabilization leads to the further deposition accompanied by aggregation. Major topic of this dissertation is dedicated towards such subsequent deposition driven by heating of proteinaceous systems, which usually leads to a surface fouling. The deposition of colloids from suspension onto various surfaces is of great significance in many processes. In some

cases the deposition is desirable, in others, like in case of fouling in liquid evaporator, it needs to be prevented.

Surface Interaction Energies

Illustration of a colloidal process at solid-liquid interface can be found in Figure 1-1. From the theoretical point of view, deposition of particles onto a surface is just a special case of general two particles interaction. Colloidal particles can deposit on a surface and detach back to the bulk solution, or they can interact among themselves and aggregate. This process is conceptually divided into several steps. In the first step colloids are transported close to the surface either by convective flow, diffusion or by help of external forces like gravity. The second step is the interaction with surface forces acting over different ranges, therefore the boundary between two major steps is somewhat continuous and arbitrary from one system to another. A possible choice to define the interaction boundary is to set potential at boundary equal to $k_B T$.

There are several forces contributing to the total interaction potential energy V_T of colloidal particles deposited on surface. This can be formally written as follows:

$$V_T(h) = \sum_{1}^{n} V_i(h) \qquad (1.1)$$

Where h denotes distance between interacting surfaces. Two of them: *van der Walls attraction* (V_A) and *electrical double layer repulsion* (V_R) were base for the famous DLVO theory, described by Derjaguin and Landau (1941) [1] and Verwey and Overbeek (1948) [2]. Both forces contribute the most to the total interaction energy. Van der Walls attraction is always present and is hard to be manipulated from an experimental point of view. On the other hand, the electrostatic interactions are extremely sensitive to the ionic strength, ion valency, pH and presence of surfactant, thus they represent the first choice to actively control the interaction process.

There are two theoretical approaches used to evaluate van der Waals interaction. Hamaker [3] suggested so called classical approach (also called microscopic approach). He made pair-wise summation of all relevant intermolecular interactions, which he divided into purely geometrical part and interaction part. The interaction part is usually expressed as constant A_{Ham} (Hamaker constant), which can be determined from the optical properties of the colloids. The geometrical part is usually expressed as a function of distance between interacting bodies

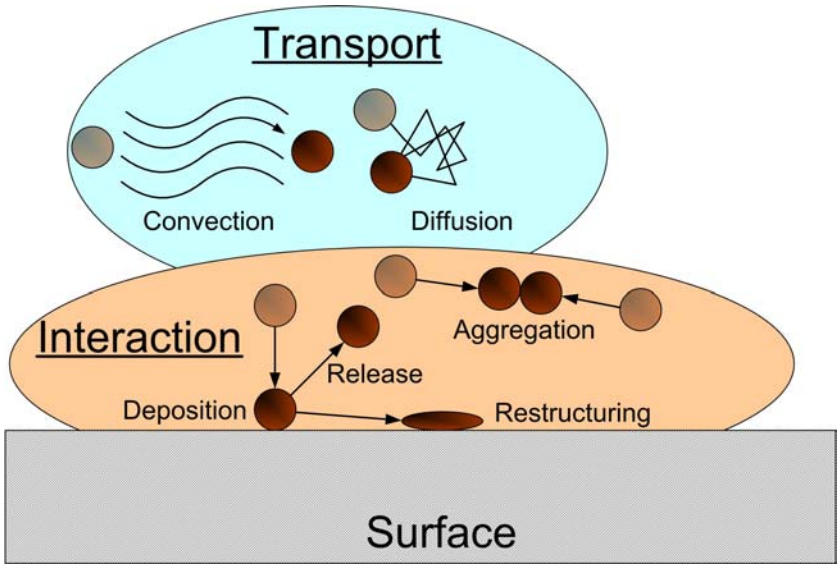

Figure 1-1. *Illustration of a colloidal process at solid-liquid interface. Colloids can be transported towards solid surface either by convective or diffusive transport, where they can deposit. Adsorbed on the surface they can be possibly reversibly released from the surface or they can restructure and become irreversibly attached. Next to the deposition on the solid surface, colloids can interact among themselves in the liquid bulk and aggregate. Processes where aggregation competes with deposition usually lead to the surface fouling.*

h and a radius of the interacting colloid *a*. Than van der Waals interaction energy can be formally expressed as follows:

$$V_A = A_{Ham} \cdot f(h,a) \tag{1.2}$$

Another approach, so called macroscopic, was suggested by Liftshitz [4]. He determined interaction entirely from the properties of macroscopic electromagnetic medium. However, the most used approach is that of Hamaker, with applied corrections to account for retardation effect.

In a case of deposition from liquid solutions, the long range electrostatic interactions play one of the dominant role in overall colloidal stability. The surface charge is usually partially balanced by counterions, forming Stern and Helmholtz layers. The rest of counterions and co-ions balancing the overall surface charge form so called Gouy diffuse layer. Poisson equation gives relationship between charge density ρ and potential φ:

$$\nabla^2 \varphi = \frac{\rho}{\varepsilon} \tag{1.3}$$

Where ε denotes dielectric constant. Assuming Boltzmann distribution of the ions with valence z on the local potential given as follows:

$$c_{h,i} = c_{\infty,i} e^{-z_i e \varphi_h / k_B T} \tag{1.4}$$

Under assumption of flat interface so that potential varies only in direction normal to the interface gives famous Poisson-Boltzman equation which describes the surface potential as a function of ion concentration and distance:

$$\frac{d^2\varphi}{dh^2} = -\sum_i \left(\frac{z_i e c_{\infty i}}{\varepsilon \varepsilon_0} e^{-z_i e \varphi_h / k_B T} \right) \tag{1.5}$$

Where ε_0 is permittivity of free space and e is electron charge. There are two useful approximations to the Poisson-Boltzman equation. For low surface potentials ($\varphi_0 < 25mV$) the Debye-Hückel approximation is used to estimate potential drop as function of a distance from the surface.

$$\varphi(h) = \varphi_0 e^{-\kappa h} \tag{1.6}$$

Where κ is co-called Debye-Hückel parameter giving a distance from surface equal to κ^{-1} [m], at which potential falls to value e^{-1} of the surface potential φ_0. For the general case of electrolyte solutions containing number of dissolved ions, κ can be calculated as follows:

$$\kappa = \sqrt{\left(\frac{\sum_i e^2 c_{\infty,i} z_i^2}{\varepsilon \varepsilon_0 k_B T} \right)} \tag{1.7}$$

Many expressions to calculate double layer interaction energies were derived for various geometrical systems and are summarized in comprehensive literature [5-7].

Next to them, non-DLVO forces significantly contribute to the total colloidal stability. Here belongs the short range *Born repulsion*, originating from interpenetration of electron shells over short inter-colloidal distances. *Hydratation effect* is another non-DLVO interaction, which is especially important for biomolecules carrying a surface charge, like proteins having a large amount of water molecules attracted to such hydrophilic sites, giving extra repulsion interaction over distances comparable to double layer interactions. Another non-DLVO interaction is the *hydrophobic effect*. If the surface has very low polarization, there is low affinity for water molecules, which are usually highly oriented in the bulk liquid due to hydrogen bonds. Limited ability of water to form clusters close to such surfaces results in access of free energy, and therefore, giving extra attraction for hydrophobic surfaces to

interact. Last of the forces, which belong to the group of non-DLVO interactions is the *steric effect*. This kind of interaction is often provided by polymeric molecules having one part strongly attracted towards surface, but still providing some polymer chain extended towards bulk liquid. Such chains can be hydrophilic, providing extra stability to interacting surfaces due to additional steric repulsion.

Now, returning back to the Eq. (1.1), where the total interaction energy V_T between interacting colloid-surface is given as a sum of all above described contributions, we end up with exact expression giving prediction for interacting energy V_T as a function of a separation distance. From conceptual point of view two different deposition cases can be distinguished from the shape of V_T. In transport limited deposition is V_T always attractive over arbitrary separation distance h. This is usually observed for higher ionic strengths. The deposition kinetics for such case is fast and limited just by transport. On the other hand, if repulsion term becomes dominant over the attractive forces, there is a repulsive barrier at certain separation distance creating reaction barrier, which has to be overcame by both interacting surfaces. This, so called reaction limited deposition, very often occurs between similarly charged molecules.

The same regimes can be observed for detachment step. Transport limited detachment can be observed in a case when V_T among two interacting surfaces is only repulsive over the whole separation distance. However, if repulsive energy barrier exists, than the detachment process becomes detachment limited. The theoretical models based on DLVO, which express the total interaction energies between interacting surfaces, were tested in many works about deposition, where prediction of deposition rates derived from theory were confronted with experimental observations. Such studies are usually done under well defined hydrodynamic conditions, with well characterized colloids (the homogeneous material, narrow polydispersity and size distributions) and well defined bulk liquid and depositing surface properties. Studies can be divided into two above mentioned groups: transport limited (attractive double layer presence) and reaction limited (repulsive double layer presence). Especially, in the case of the reaction limited deposition, the discrepancies between theoretical predictions and experimental observations are remarkable. In a comprehensive overview [5], very poor or no agreement between theoretical predictions and experimental observations are reported. None of the compared studies conclude a good agreement between predictions and experimental observations [8-21]. The quantitative failures of used predictions are related to the

simplifications made during model construction, like the ideal distribution of surface properties, surface charge homogeneity, ideally flat surface etc.
On the other hand, when repulsive forces are eliminated (for transport limited deposition), the agreement between theoretical predictions and experiments were found [22-25].

Interactions of Biomolecules

The primary structure of many biological molecules is simple as that of primary structure of monomers in synthetic polymers. From this point of view, the biomolecules do not differ from synthetic polymers. However, behind the relative chemical simplicity can be hidden rather complex and specific behavior. Secondary and tertiary structures of globular proteins often play an essential role in interaction mechanism. The concepts introduced above, used in colloidal chemistry are still relevant for understanding the behavior of biological macromolecules, even such biopolymers are more complex than synthetic polymers. Effects of conformational entropy, internal cohesion, electrostatic and intermolecular interaction have to be considered. Structure and stability of proteins in aqueous solution can be influenced by any interaction summarized below.
Conformational interactions: Most of the globular proteins contain a significant amount of ordered structural elements (~40-80%). They are stabilized by hydrogen bonds between peptide and polypeptide backbone. For protein of molar mass 10000Da the conformational entropy can be few hundreds of kJ/mol.
Hydrophobic interaction: Dehydration of non-polar components in aqueous environment leads to an increase of the entropy of the water molecules released from such components. This hydrophobic dehydratation attracts apolar parts of the protein to associate in aqueous environment. For globular protein of 10000Da the hydrophobic dehydratation contributes to the total interaction energy around 500 kJ/mol.
Electrostatic interaction: Charged amino acid residues are located on aqueous periphery of the molecules. Ion pairs on the protein surface stabilize the protein structure. Near isoelectric point the electrostatic interaction tend to stabilize compact protein conformation, while at extreme pH expanded and less compact conformation can be expected. Furthermore, the ionic strength affects the distance over which charged groups can interact. During unfolding of globular protein such ion pairs (preferentially localized in the interior of the protein) are ruptured, but hydratation of separated ionic groups helps to stabilize the unfolded molecule.

Van der Waals interactions are sensitive to the separation distance. Upon protein folding the dipolar interactions play significant role, because they must be first disrupted and after folding they must be newly formed.

Hydrogen bonds are mostly formed between amide and carbonyl groups of polypeptide backbone. Upon unfolding they may be compensated by peptide-other peptide of peptide-water bonds.

Steric interactions. It is estimated that steric interaction contributes to the overall interaction energy by several kJ/mol.

As can be seen the total interaction energy, thus stability of amphiphilic protein molecules, is strongly influenced by liquid media surrounding them. Changes in the liquid environment such as pH, ionic strength, heat, shear or presence of interface, can affect their stability. As a consequence the deposition/aggregation can occur. The most studied aggregating proteins are known to be insulin and β-lactoglobulin. The self association of insulin under various conditions can affect the efficiency of diabetes therapy [26-28] and β-lactoglobulin is the globular protein responsible for fouling during milk heat-treatment [29-32]. The temperature driven deposition from the proteinaceous solutions, studied in this work, belongs to the group of reaction limited depositions. The temperature is used to manipulate repulsion barrier among proteins or their complexes with other biomacromolecules. As a result of increased thermal motion of aminoacid residues in the polypeptide chain, the proteins undergo a major conformational changes at elevated temperatures. They retain their secondary structure, while the tertiary structure is modified. This effect of protein unfolding, which consists of many subsequent conformational changes, is explained by molten globule state theory [33]. Thermal unfolding leads to the modification of the heterogeneous steric structure of the proteins and as a consequence the surface fouling occurs.

1.3 Surface Modifications

Deposition of biomolecules onto various types of surfaces drives significant attention in many research fields. The most intensively studied systems are between proteins and variously modified surfaces. In a case of temperature driven fouling the primary deposited layer can influence the mechanical stability of the subsequently developed secondary deposits. As known from numerous studies dedicated to fouling [34-36], surface modification does not

necessarily prevent fouling, rather it can provide the specific interaction for the primary deposited layer, and therefore, the subsequently deposited layer can be removed easier.

Several surface modifications were done in order to study the initial deposition between the proteinaceous solution and the surface. Surfaces used in this work can be divided into two groups: oxide surfaces and polymer surfaces.

Various oxides differing in their isoelectric point (IEP) were used to monitor the primary deposition of the oxide surfaces by various proteinaceous solutions and monitoring various small electrolyte adsorptions. Here is short overview of used surfaces and their important characteristics:

Silica-Titania Sensors are original planar waveguide chips OW 2400 for OWLS measurements. They were purchased from Microvacuum Ltd. (Budapest, Hungary), and consists of a 1-mm-thick AF45 glass substrate and a 180-nmthick $Si_{0.75}Ti_{0.25}O_2$ waveguiding surface layer, with a dimensions of L=1.2cm, W=0.8cm and H=0.1 cm (see Figure 1-2). IEP of silica is 3.0 and the titania around 5.5 [37].

Silica Coated Sensors were purchased from Microvacuum Ltd. (Budapest, Hungary). The original planar waveguide chip is modified by 10 nm silica layer. The IEP of silica is 3 [37].

Alumina Coated Sensors were purchased from Microvacuum Ltd. (Budapest, Hungary). The original planar waveguide chip is modified by 10 nm alumina layer. The IEP of alumina is 8 [37].

Niobia Coated Sensors 10 nm of Nb_2O_5 were sputter coated onto original planar waveguide purchased from Microvacuum Ltd. (Budapest, Hungary), using reactive magnetron sputtering (PSI, Villigen, Switzerland). The IEP of niobia is 4.3 [37].

Three polymeric films were used to modify original oxide surface.

Poly(L-lysine)-3.5-poly(ethylene glycol) (PLL-3.5-PEG) Is a polycationic grafted copolymer, positively charged at neutral pH. PEG chains are grafted to amino-terminated side chains of a PLL backbone. The number 3.5 denotes PLL to PEG ratio. It was spontaneously adsorbed onto negatively charged original surface from aqueous solution. It belongs to the family of the polymers used to modify original hydrophilic surfaces. Such polymers have few common surface properties, such as hydrophobicity, charge neutrality and absence of hydrogen bond donor groups. The principle is based on generation of intermediate repulsive force, which prevents proteins from contact with the highly attractive oxide surface, minimizing the

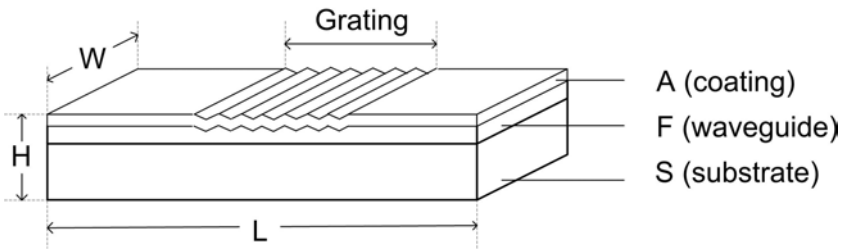

Figure 1-2. *Sketch of a coated sensor chip.*

protein-surface interaction due to mutual change of hydrophobic, steric and electrostatic interaction. Next to the used PLL-g-PEG and PS, variety of polysaccharides, polyacrylamide, poly(hydroxyethyl) methacrylate and other polymers can be found in literature about surface coatings.

Polystyrene (PS) The neutral polystyrene layer approximately 20 nm thick was spin coated on the silanized original waveguide using 1wt% polystyrene dissolved in toluene at rotation speed 3000RPM for 1 minute [38, 39]. PS used in this study was PS Standard 30'000 from Sigma-Aldrich (Product Number 81408) with Mp=32500, Mn=31000, Mw=32000, Mw/Mn=1.02.

TEFLON AF® Another neutral hydrophobic surface next to PS. The spin-coated layers were approximately 20nm thick. We were using 10wt% TEFLON AF® from DuPont (type 1601) dissolved in perfluortributylamine from DuPont (type AF-45).

1.3.1 Spincoating of Nanometer Thick Polymer Films

1.3.1.1 Introduction

Spin coating from dilute polymer solution is a common method to produce thin, uniform polymer film on planar substrates. It is often used in the microelectronics industry to produce circuit pattern to a semiconductors. The main purpose of the waveguide coating is to modify sensor interface, which can be used for monitoring of the colloidal deposition or adsorption on polymer surfaces. With respect to the overall concept of this work we tried to spincoat stable, thin, non-polar polystyrene (PS) and Teflon® AF layers that would resist higher temperatures, especially in the range 60-80°C to be afterwards used to study the proteinaceous deposition.

It will be shown in the chapter 3, that when oxide surface is contacted with an electrolyte solution it exhibits signs of surface modification. This is most likely caused by activation of accessible hydroxyl groups connected with slow solubilization of the surface and its accessible pores. Thus, a stable thin polymer layer can positively influence the problems of oxide interaction with electrolytes via effective insulation of the oxide layer from electrolyte solution.

Preparation of ultrathin polymer film is a delicate process. The film has to be thick enough to homogeneously cover the surface, but reasonably thin to give good sensor sensitivity. As mentioned in experimental methods section, the reflected electromagnetic wave senses the region about 100nm above the waveguide surface. Therefore, the reasonable thickness of polymer layer is around 10-20nm. For such a thin polymer layer, physical properties are very different from those of thicker layers or bulk polymer. Thin film differs from bulk material in many ways. Melting point of the film can be different, micro-pores, which are hardly detectable but permeable for small ions and molecules, may be present.
Polymers which are suitable as coating materials may be poly(methyl methacrylate) - PMMA, poly(styrene) - PS, poly(carbonate) – PC, poly(siloxane) and fluorinated polymers like Teflon® AF. General feature of such films is that they have quite small transmission losses (100dB/km – it means a transmition distance of 200 m if one assumes a detection limit of 1% of the initial light intensity). For comparison glass fibers (best waveguide material) have losses of 0.15 dB/km and Teflon® AF 10 dB/km.

Materials and Methods

Spincoating was performed by 8" Desk-Top Precision Spin Coating System (Model P-6708D) acquired from Specialty Coating Systems, Indianapolis. For waveguide coating we have chosen two non-polar polymers PS and Teflon® AF. Their structural formulas can be seen in Figure 1-3. PS is one of the most studied systems in colloidal science, therefore, a solid base of information exists. Based on work [38-42], as well as our experimental experience we have chosen as the optimal coating solution the Polystyrene Standard 30 000, from Fluka, (Lot. No. 440166/1 12802) solubilized in toluene, from J.T. Baker (Lot. No. 0100410001). The bulk polystyrene has refractive index ~1.59.

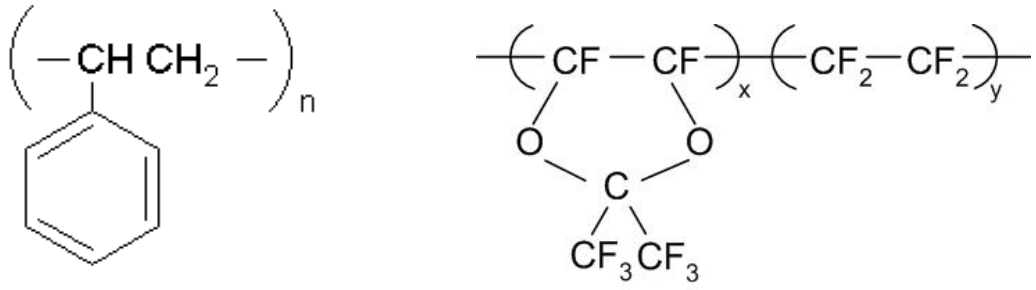

Poly(styrene)

Poly(perfluoroethylene-co-trifluorodioxol); Teflon® AF

Figure 1-3. *Structural formulas of polymers used for coatings*

Teflon® AF, from DuPont (type 1601) solved in perfluortributylamine (type FC-43) is very interesting coating material, not only because of its optical and electrical properties, but also due to its chemical resistivity. It can be coated onto waveguide substrate to enhance biocompatibility for optical sensing and diagnostic applications. It has very low refractive index 1.38. Teflon® AF may be an appropriate replacement for nowadays used corrosion-resistant coatings for electronics or replacement of current technology in other high-tech applications.

Pre-coating waveguide treatment: Original titania-silica waveguide surfaces were etched for ten hours in 1wt% aqueous solution of potassium monopersulfate triple salt (Riedel-de Haen®, Cas-Nr-37222-66-5). This process activates silanol sites at the accessible waveguide surface, thus make it homogeneously charged and hydrophilic. Activated oxide surfaces were rinsed by purified water and gently dried by air. Subsequently, they were placed into silanol atmosphere for 16 hours, using hexamethyldisilazane from Fluka, (Lot. No. 427155/1 44601).

The Silanization treatment makes the hydrophilic oxide surface hydrophobic, thus attractive for coating from non-polar solutions. Chips were baked at 150^{o}C in vacuum to stabilize the covalently adsorbed hydrophobic molecules. Silanization is essential procedure step, which is needed to improve the adhesion of the spin-coated polymeric layer on otherwise hydrophilic oxide surface. Such sensors were stored in the closed glassy vials to prevent any surface contamination before final coating step.

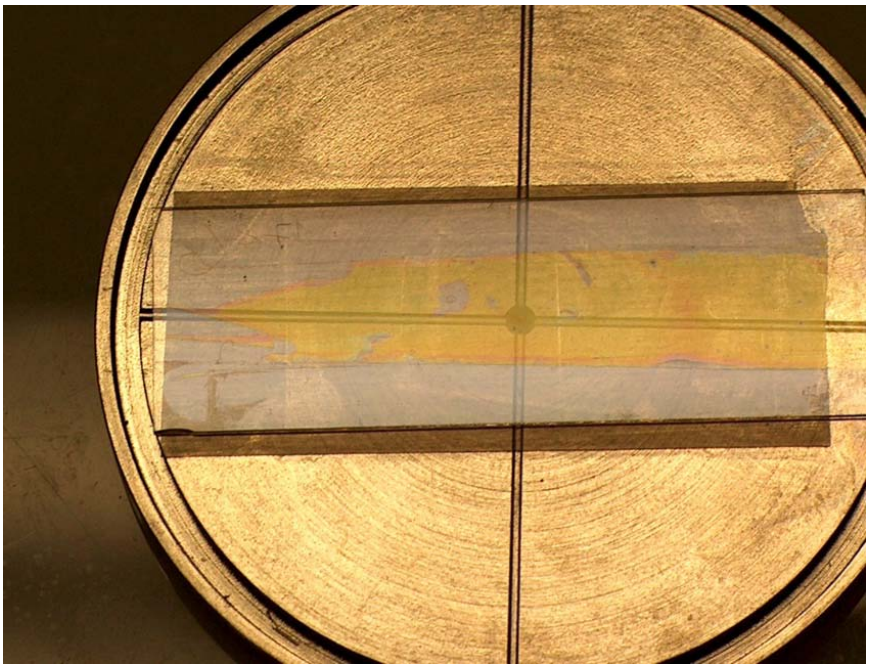

Figure 1-4. *Spin-coating apparatus. Sensor chip is placed on the top of the custom made spin-coater chuck. The sensor is held on the chuck by vacuum created by an external pump through the hole visible in the middle of the chuck. Whole coating was performed under nitrogen atmosphere.*

Spin-coating process: During the spin-coating process, solution is first deposited on the sensor, and then it is accelerated rapidly to the desired rotation rate (see Figure 1-4). Liquid flows radially, pushed by centrifugal force, and the excess liquid is ejected off the edge of the substrate. The film is continuously formed by disjoining pressure until it reaches an equilibrium thickness. The final thickness is given by solvent evaporation and post-coating heat treatment. After the initial heat treatment the waveguide is immediately placed on the spin-coating chuck and a drop of coating solution is spread in a thin layer on the top of the waveguide. The desired film is formed at a certain spinning speed (ω) for a certain spinning time (t_S).

The quality of the coating was always inspected by microscopical and spectral characterization. Moreover, the microstructure of coated layer was inspected closely by SEM and AFM as it is reported below.

1.3.1.2 Results and Characterization of Thin Spincoated Films

We were able to prepare a wide range of PS, and Teflon® AF coatings with thickness from 10 nm up to 100nm. Such values are hard to be found in literature about the spin coating, due to the fact that the thicknesses needed for sensor coating usually cover the bottom range of investigated conditions. The main reason is that the film thickness starts to be smaller than molecular dimension of used polymer chainlength, thus the physical properties of the film deviates from the polymer in a bulk as reported in literature [38, 39, 41-50]. This requires detail inspection of the film homogeneity, continuity and mechanical stability. On the other hand the thin coatings were needed due to physical principles of the optical waveguide lightmode spectroscopy. Generally, for the ultrathin PS layers decrease of a glass-transition temperature was observed in comparison with the bulk PS. Decrease depends on the thickness of the films as well as on the chain-length of PS molecules. Data available in literature for the PS films of the size comparable to the thicknesses produced by us are quite scattered and the transition temperatures can be found in a range of 25-150°C. In order to crystallize the coated polymer layer, the coated sensor was stored at 100°C under vacuum atmosphere followed by long (~10 hr) cooling to prevent film destruction.

Results of spin-coating are presented in a Table 1-2. The first column gives a reference sensor number. The second column provides a weight percent of the polymer (PS or Teflon® AF) solubilized in a corresponding solvent (toluene, perfluortributylamine, respectively). In the third column the spinning speed is given in rpm (rotations per minute) and the forth column reports to the spinning time duration. Finally, the fifth column gives a mean coated polymer layer thickness, which was measured by OWLS and evaluated by the linearized adlayer model [51]. The refractive indices used to evaluate the model are provided above, in the material and methods of this appendix.
After spin-coating, the sensor was heat-treated at 100^{o}C, under a vacuum atmosphere. To check the final quality of the coated films different methods were used, which gave us information about quality of prepared coated films.

Table 1-2. P*arameters of the spin-coating process and corresponding thicknesses obtained.*

Sensor Nr.	polymer - concentration	spinning speed	time	thickness
	[wt%]	[rpm]	[s]	[nm]
1	PS - 0.16	1200	19	40
2	PS - 0.5	1500	20	20
3	PS - 0.5	1500	20	16
4	PS - 0.5	1500	20	27
5	PS - 0.5	1500	20	17
6	PS - 0.5	1500	20	19
7	PS - 0.7	3100	60	18
8	PS - 0.7	2000	20	52
9	PS - 0.7	1500	20	72
10	PS - 0.7	2000	20	50
11	PS - 0.7	2000	20	46
12	PS - 0.7	2000	20	46
13	PS - 0.7	2000	20	46
14	PS - 0.7	2000	20	67
15	PS - 0.7	2000	20	51
16	PS - 0.7	2000	20	65
17	PS - 0.7	1500	20	50
18	PS - 0.7	2500	40	50
19	PS - 0.7	3200	40	27
20	PS - 1	1500	60	97
21	PS - 1	3100	60	61
22	PS - 1	1200	20	100
23	Teflon® AF - 10	1800	30	29
24	Teflon® AF - 10	2500	30	35
25	Teflon® AF - 10	1000	50	58
26	Teflon® AF - 10	1900	50	26
27	Teflon® AF - 10	2500	60	30
28	Teflon® AF - 16	2000	20	37
29	Teflon® AF - 16	2000	20	14

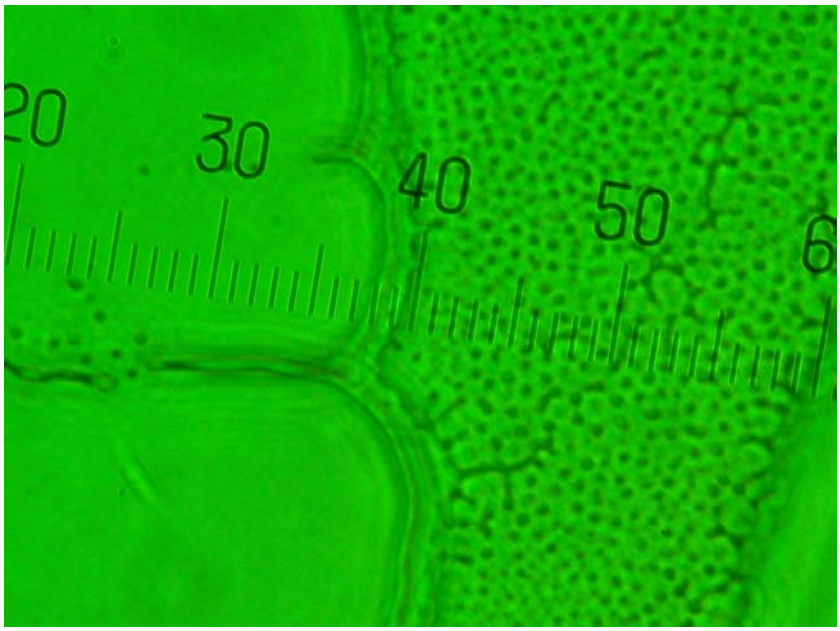

Figure 1-5. *Polystyrene film corrupted by heat treatment under vacuum, temperature starting at 150°C. The continuous coverage can be seen on the left, while dewetted droplets are formed on the right side of the image. Object is magnified 300 times, one unit in figure represents 1μm.*

1.3.1.3 Characterization of the Coatings

We used several approaches to examine the properties of the prepared coatings. First check was done by optical microscopy, where one can see whether the film is continuous or not. Secondly, the microstructures of coatings were inspected by high resolution imaging techniques SEM and AFM. Finally, OWLS spectra provide information about coated polymer layer homogeneity and quality.

Laser Scan Microscopy: An illustrative image of a PS film corrupted by dewetting during heattreatment can be seen in Figure 1-5. The good coating must be transparent for the light coming upon incident angle being close to perpendicular angle to the coated surface, for both polymers considered here. On the other hand, the droplets of dewetted polymer would cause the light dispersion, resulting in observed film translucency. Thus, translucent layers indicate corrupted coating, while transparent good one.

Visual Inspection: Another fast visual check of the coating continuity is based on total reflection, when areas covered by polymer film totally reflect the incoming light, while uncovered areas are transparent. An illustrative example can be seen in the Figure 1-4.

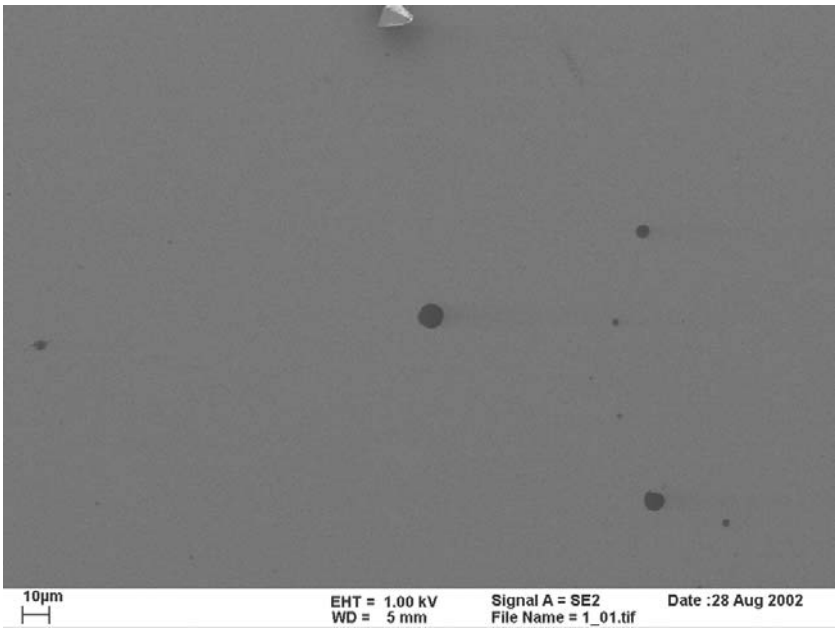

Figure 1-6. *Bare chip structure. Inhomogeneities in the waveguide film circles up to 10 microns in diameter are visible.*

The polymer layer covering the sensor surface reflects the light differently compared to the sensor surface. Therefore under certain angle of incidence, the light is reflected totally from the polymer film, while the rest of the sensor is transparent and almost invisible. Visual check is very quick and useful information about the coating quality and helps us to exclude corrupted coating without any further analysis.

However, the primary visual and microscopical inspection does not give much information about microstructure of the coating itself. That has to be done by other techniques with higher resolution. Scanning electron microscopy (SEM) and atomic force microscopy (AFM) were used to inspect the spin-coated films down to several tens of nm. Three different surfaces were checked by both SEM and AFM techniques: bare sensor, sensor covered by PS and Teflon® AF layer.

Scanning Electron Microscopy: Image of a bare sensor surface (Figure 1-6) shows large, black spots in a structure of bare sensor. The technique does not allow us to distinguish, if the structures are part of the waveguide or belong to glass substrate below the surface. The black spots are randomly distributed and their diameters differ from 10 microns down below the resolution limit. The holes in structure are still visible, even after the coating.

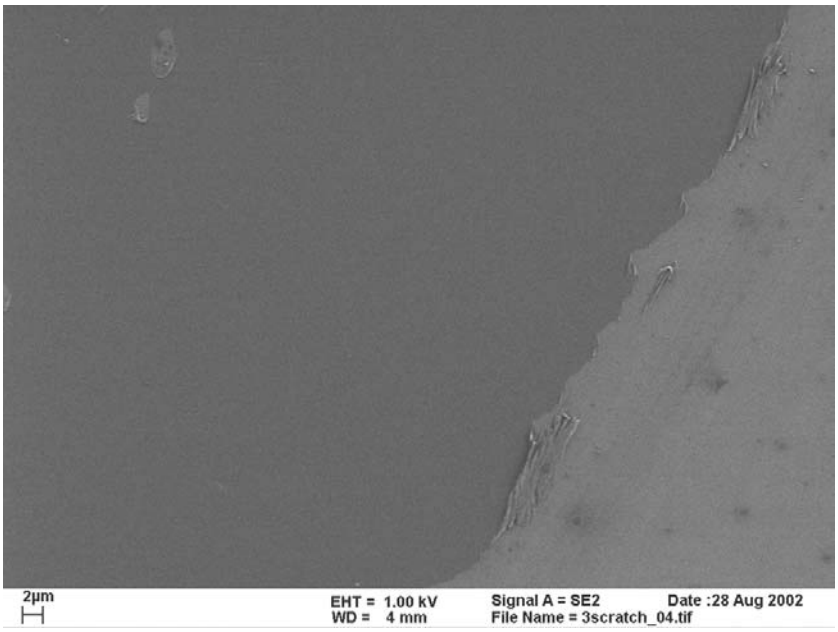

Figure 1-7. *20 nm PS layer has homogeneous coverage for whole scanned area. On the left side the scratch made to the PS layer create the contrast between polymer and substrate.*

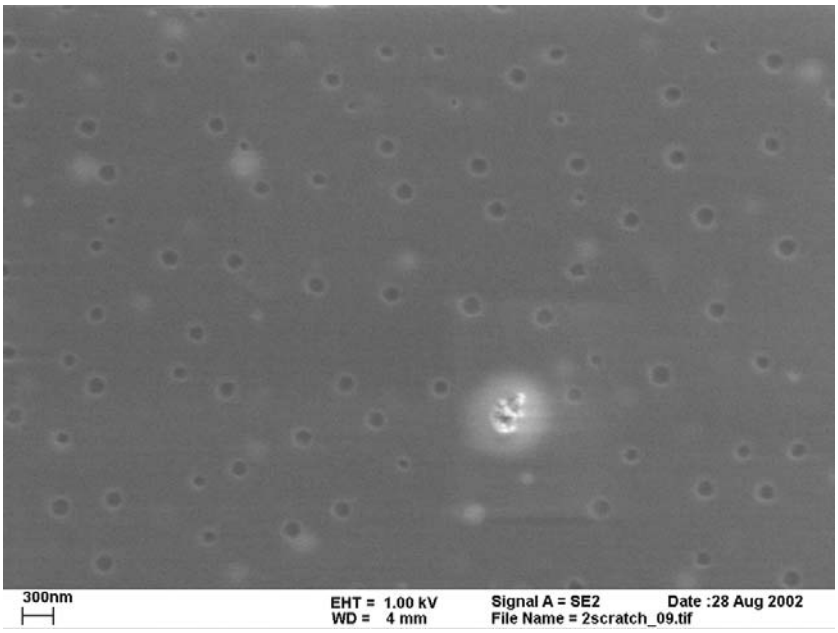

Figure 1-8. *20 nm Teflon® AF film has randomly perforated surface.*

The second inspected surface was spin-coated PS film of approximate thickness 20 nm shown in Figure 1-7. The PS layers are not visible by SEM and corresponding images look like that of bare oxide surface. However, the missing contrast between the original surface and PS layer provides the evidence about uniformity and homogeneity of the spin-coated layer.

The PS layer was visualized through SEM by scratching it to get the contrast between PS layer and substrate as can be seen in the figure. The spin-coated layer made of Teflon® AF with approximate thickness 20 nm, showed complete coverage of the surface with periodic pores clearly visible in the structure shown in Figure 1-8. The pores have narrow diameters approximately 200 nm.

Atomic Force Microscopy: The bare sensor surface was visualized by AFM in the air atmosphere. Three dimensional topography of the scanned area ($5\mu m^2$) is shown in Figure 1-9a. AFM image of the bare waveguide surface in a grating region of the sensor (see Figure 1-2) provides the evidence that there are no cylindrical holes on the waveguide film surface, which were observed by SEM. This would indicate that the hole like patterns observed by SEM (see Figure 1-6) belong to the glass substrate of the waveguide sensor and are not present in the waveguide film surface. In Figure 1-9b one can clearly follow the periodic grating structure of the bare oxide sensor (400nm) made from the cross section analysis of Figure 1-9a. SEM and AFM images scan comparably large area of the surface sensor.

In Figure 1-10 a PS layer of approximate thickness 20 nm (measured by OWLS) was inspected by AFM in the grating region of sensor. As can be seen from the figure, the PS film is homogeneous with roughness below 2nm. The grating pattern of the underneath oxide waveguide is still well visible, despite that PS layer is apparently filling the grating valleys visible in the figure of bare oxide surface. PS layer appears to be homogeneous and continuous, thus there is agreement between observations made by SEM and AFM.

A Teflon® AF layer of approximate thickness 20 nm was inspected by AFM in the grating region of sensor in Figure 1-11. Contact between AFM tip and scanned surface was sometime lost, what can indicate structure inhomogeneities. This would be supporting evidence of pores visible in SEM.

a)

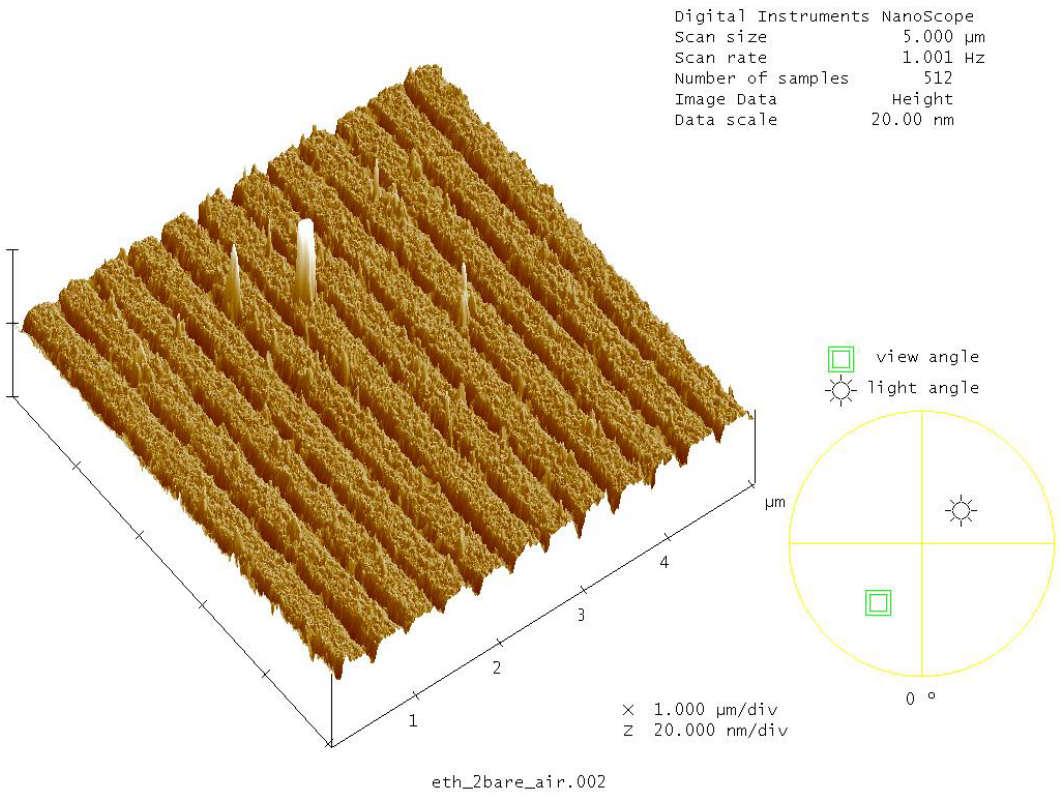

b)

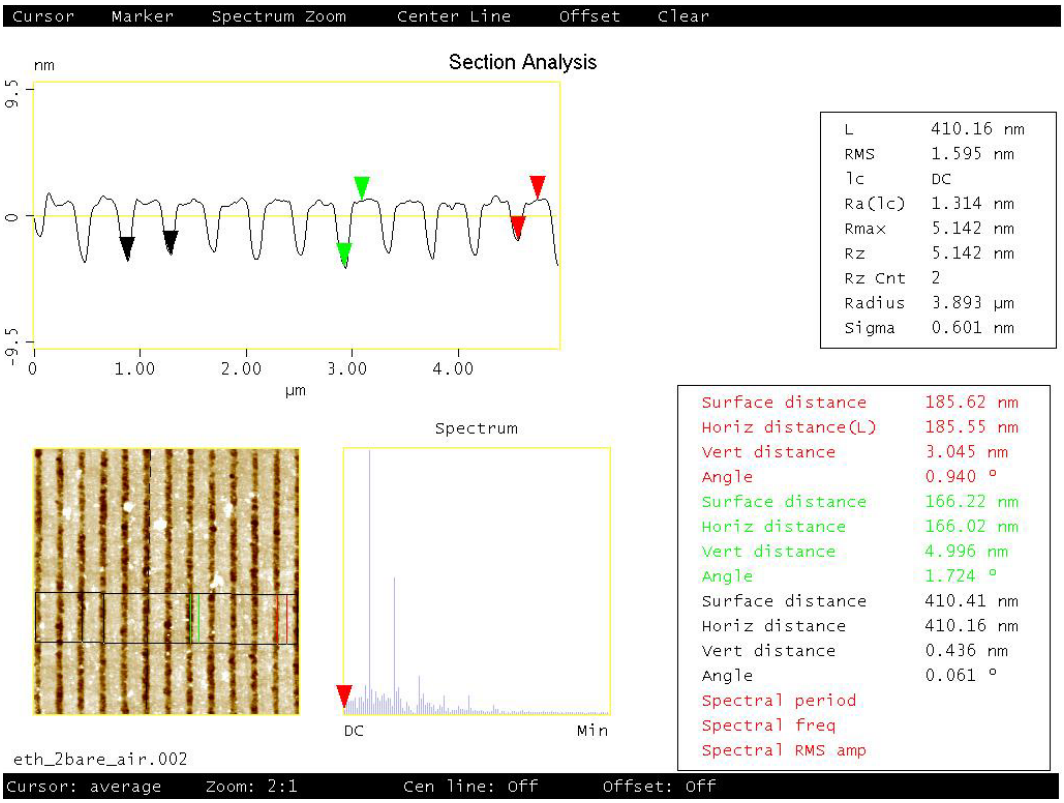

Figure 1-9. *AFM image of bare silica waveguide chip exposed to air.*

a)

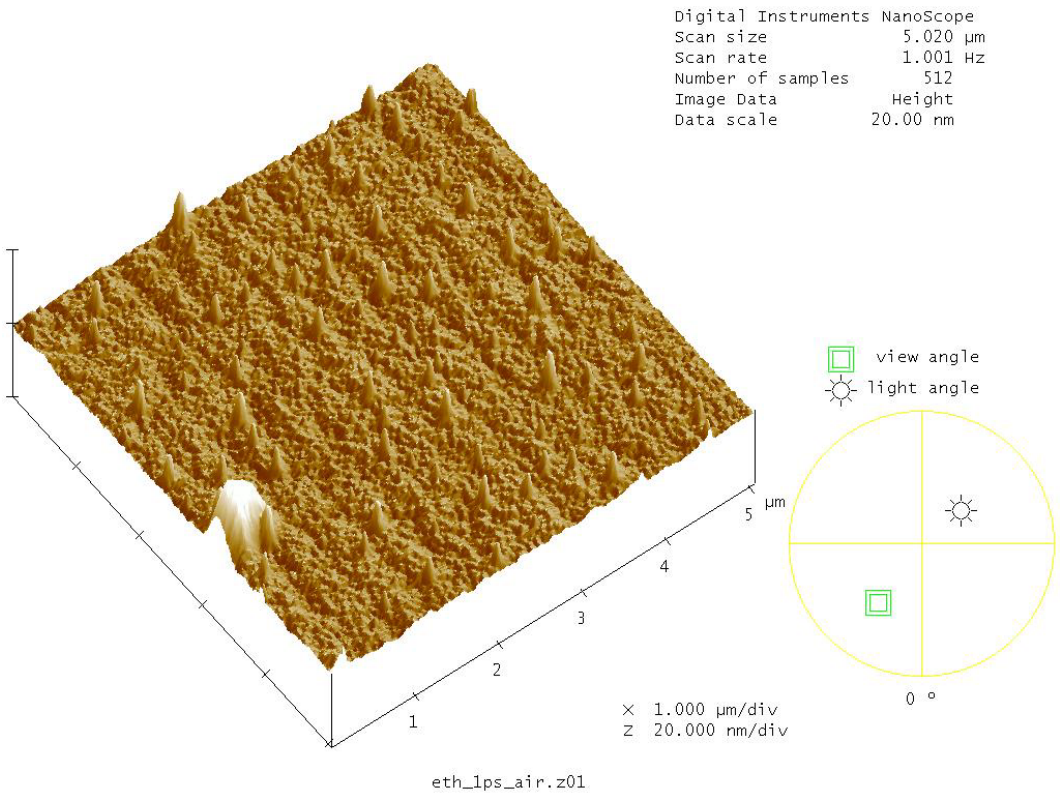

b)

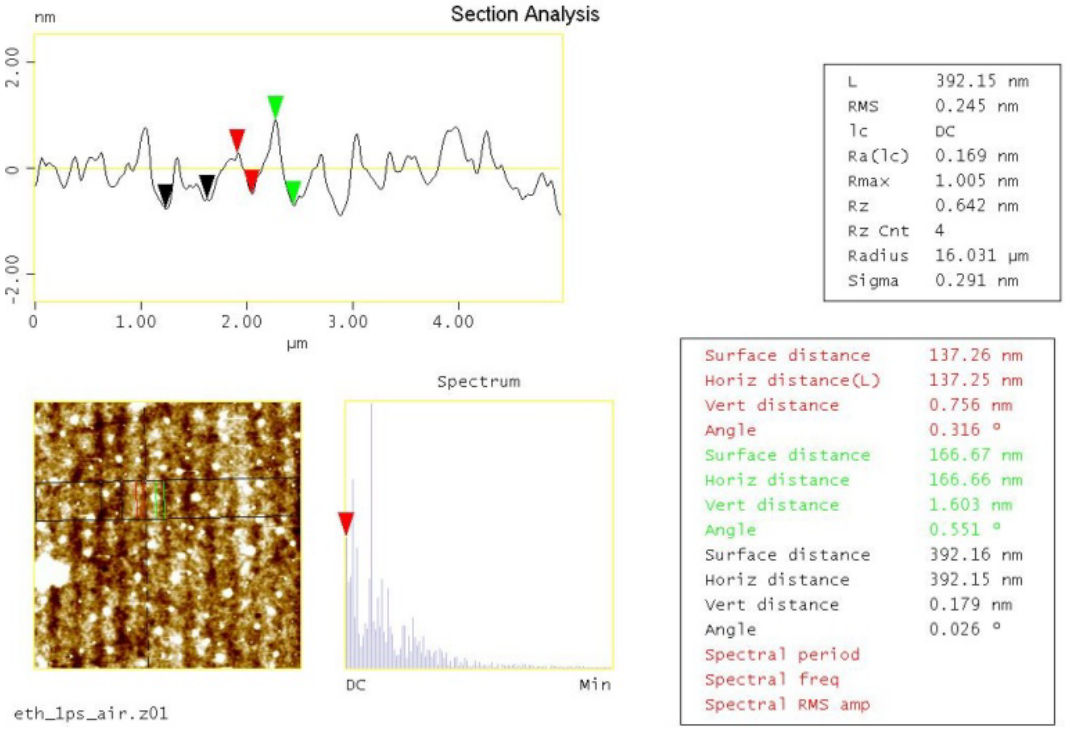

Figure 1-10. *AFM image of PS surface exposed to air.*

a)

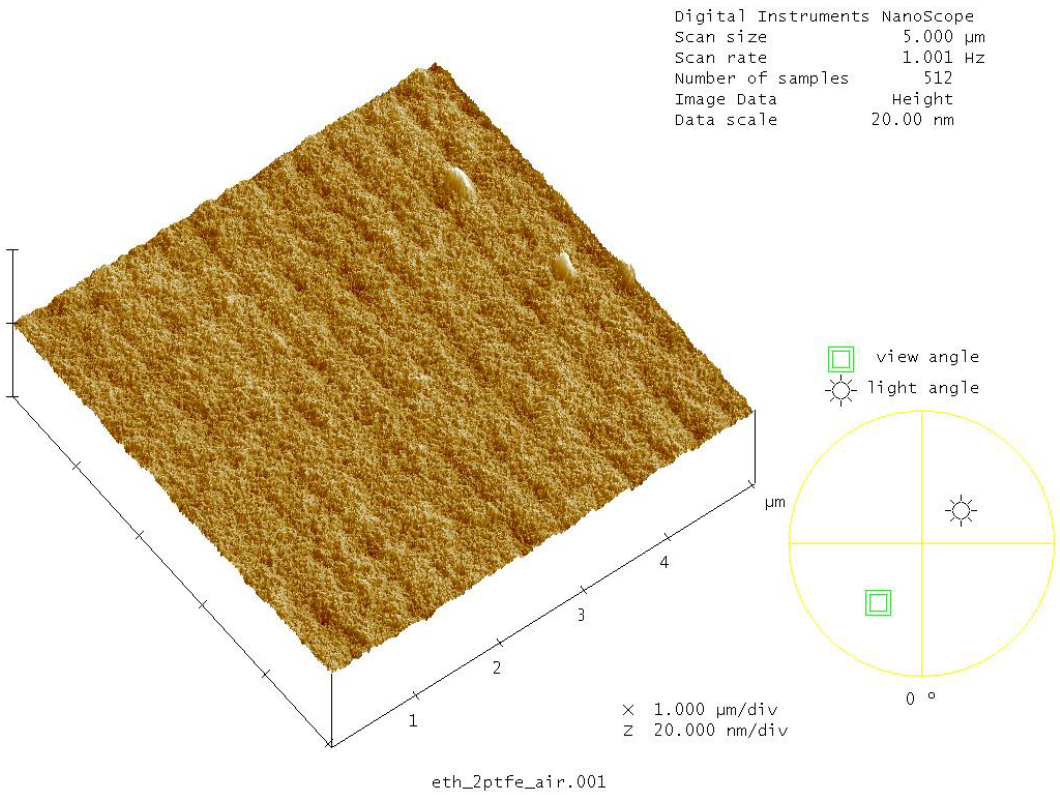

b)

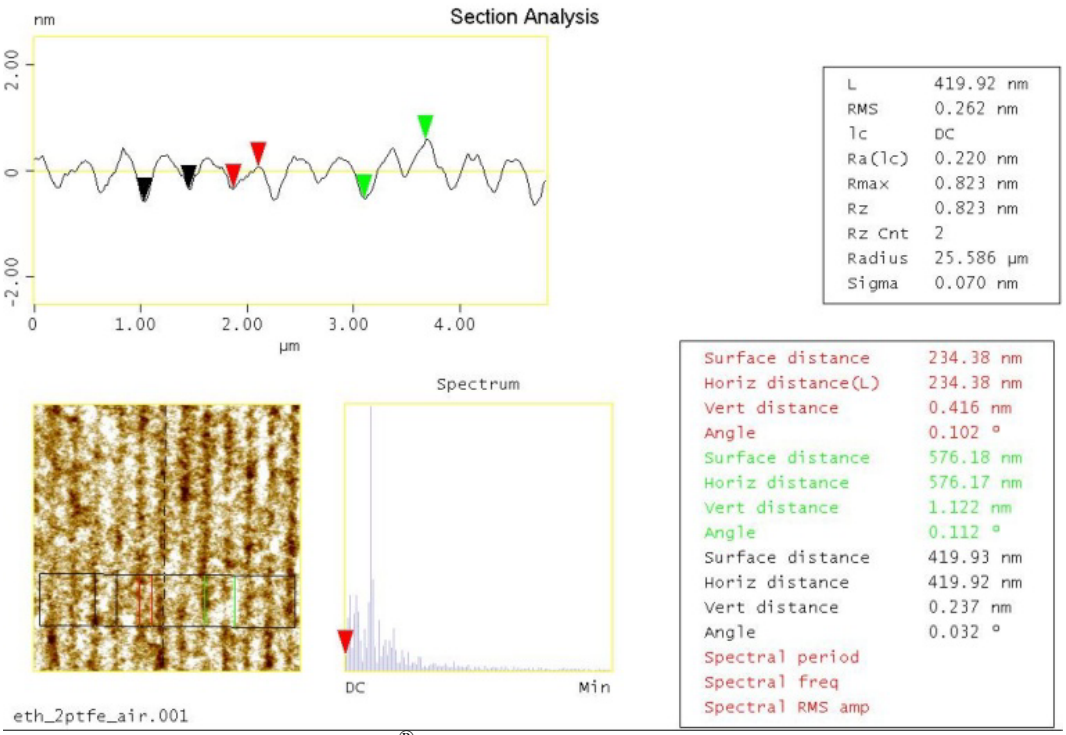

Figure 1-11. *AFM image of Teflon® AF surface exposed to air.*

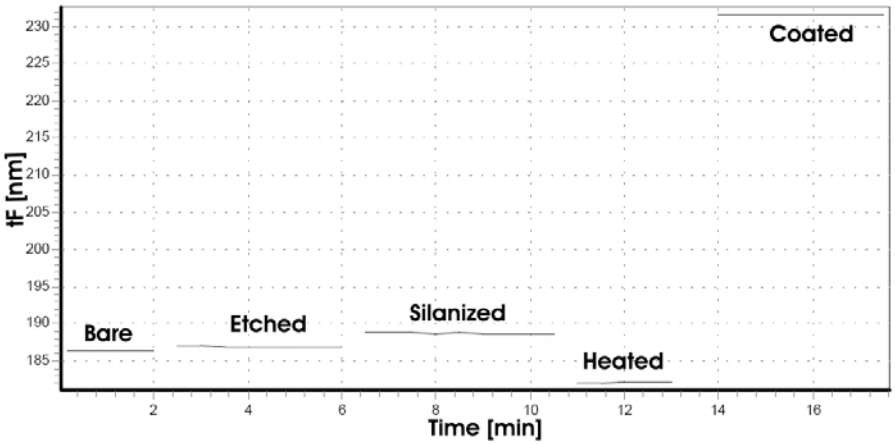

Figure 1-12. *History of the sensor thickness during spin-coating by Teflon® AF.*

Inspection by OWLS: Homogeneity of coated polymer layers can be tested by OWLS, as well. In Figure 1-12 the whole spin-coating process was followed by OWLS measuring the waveguide layer thickness in the air after each step of the spin-coating procedure described above. It needs to be mentioned, that the time ax in the figure does not correspond to the real experimental time, rather it follows the chronological subsequence of the process by steps indicated by the text labels in the figure. The initial thickness of the bare oxide sensor is approximately 186nm. The two subsequent steps (etching and silanization) slightly increase the waveguide thickness. On the other hand, the heattreatment at 150°C reduces the waveguide thickness. This thickness reduction is due to evaporation of water present in hygroscopic oxide layer. Coating should be done as soon as the waveguide is taken out from the oven, because the waveguides made of silica start to adsorb water from air rapidly, impacting the final coating quality. Therefore, it is not useful to scan every time the waveguide in this stage, but this heat shrinkage effect of the waveguide thickness has to be considered, when the final polymer thickness is calculated, especially in the case of very thin layers. The last measurement after the coating step shows the increase of the waveguide thickness, due to presence of the polymeric layer.

OWLS not only provides the thickness of the spin-coated layer, but from the shape of the resonance spectra information about the polymer layer homogeneity above the grating region can be extracted. In Figure 1-13 typical observation made on the coated surfaces is presented. The typical spectra of ideal homogeneous PS coating on the top of the oxide waveguide are shown in Figure 1-13a. The perfect coating is indicated by very narrow and symmetrical resonance peaks.

a)

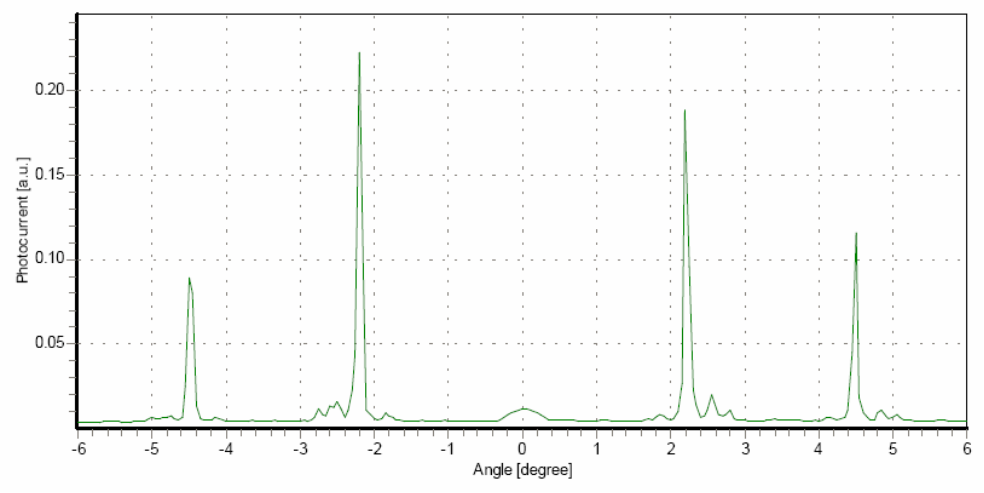

b)

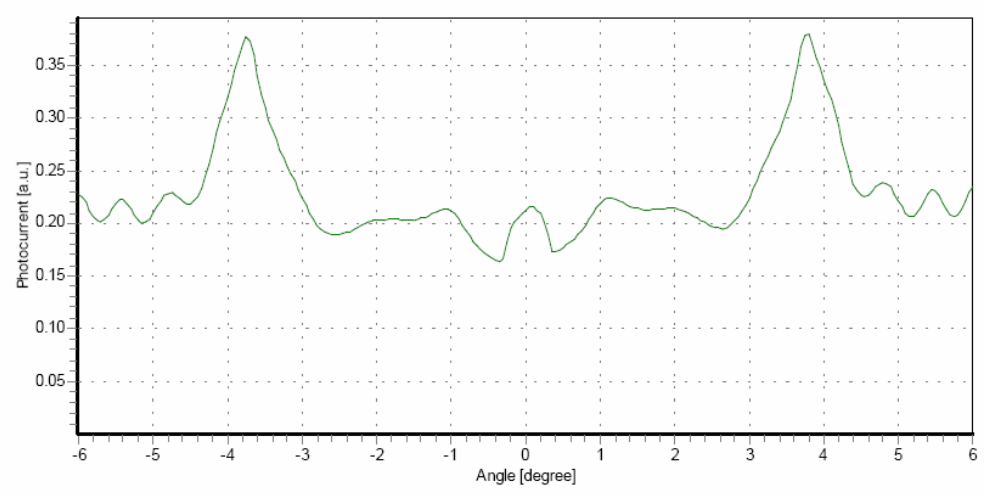

c)

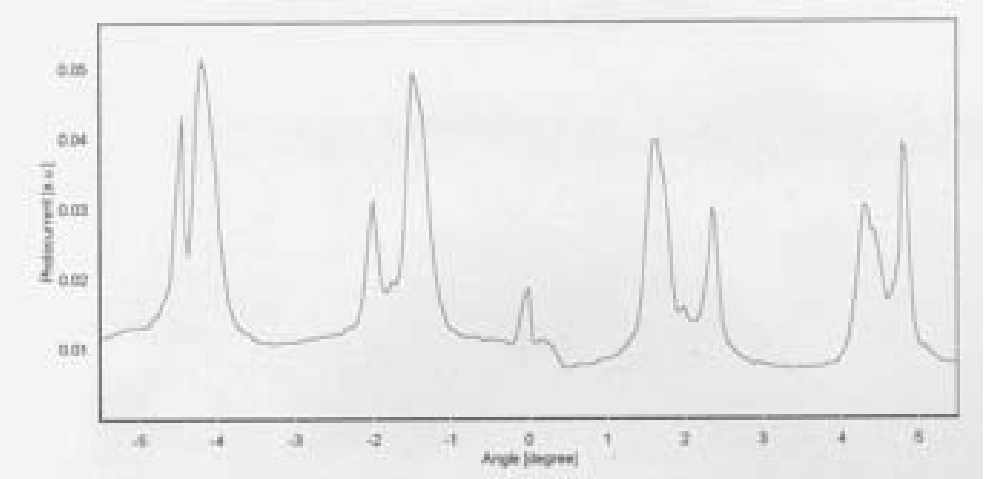

Figure 1-13. *OWLS spectra: Intensity of incoupled light (y ax) as a function of incidence angle (x-ax).a) Ideally coated PS layer b) the same layer destroyed by heat-treatment c) PS layer covers just part of the waveguide.*

Constant thickness is indicated by the symmetrical shape of the resonance peaks detected by both detectors. Symmetry of the peaks represents the equal distribution of the polymer on both sides of sensor, while narrowness of the resonance peaks indicate the reflection from very sharp interface between the polymer film and a liquid bulk. In Figure 1-13b is the very same PS layer destroyed by heat treatment at 150°C, which leads to the dewetting of the PS layer. Spectral peaks in this case are very broad due to reflection from a surface covered by scattering droplets of dewetted PS layer. The Figure 1-13c shows the extreme situation, when PS layer does not fully cover the reflecting surface above the grating area. Therefore, two different surfaces (oxide - liquid bulk, PS - liquid bulk) provide two different reflection interfaces, thus the number of resonance peaks is doubled in comparison with well covered surface showed in Figure 1-13a.

1.3.1.4 Conclusions

Spin-coating procedure was successfully performed and nanometer thick polymer films were coated on the top of silanized oxide surface. The silanization of 16 hours is needed to improve adhesion of the spin-coated layer. Wide range of PS and Teflon® AF coatings were prepared and tested. We were able to prepare coatings varying in thickness from several nanometers up to microns. Non-polar films are sufficiently continuous and homogeneous. Procedure to characterize coatings was established. Coating solution concentrations were compromised between layer homogeneity and a layer thickness suitable for OWLS investigation. Surface analyzed by imaging techniques shows that both considered polymers cover the silanized oxide waveguide. PS layer is homogeneous and continuous, but inspection of Teflon® AF surface reveals periodic occurrence of 200 nm pores in the polymer layer.

1.4 Analytical Methods

1.4.1 Techniques to Study Deposition

There are number of techniques used to measure the amount of mass deposited onto a surface in a several nanometers thin layer. Comprehensive comparison can be found in [52]. Some of these are based on optical principles of light reflected from solid-liquid interface. Here belong techniques like Optical Waveguide Lightmode Spectroscopy, Fourier transform infrared

absorption spectroscopy, Total Internal Reflection Fluorescence, Scanning Angle Reflectometry and Ellipsometry. These techniques are extremely useful by providing in situ characterization of the films at a small scale. Non-optical methods also exist, such as Quartz Crystal Microbalance, which is based on measuring the change of the piezoelectric quartz crystal frequency when a small amount of mass is attached. If the particles are bigger than one micron, the deposition rate can be studied by direct microscopic methods, where deposition rates are determined by counting the number of deposited particles at different time intervals. Direct particle counting by microscopic means is especially useful for studies of hydrodynamic conditions on deposition [13, 53-55].

Each of these methods or techniques offers various advantages and disadvantages. Total Internal Reflection Fluorescence requires molecules with either a natural or attached fluorescent label. Quartz Crystal Microbalance requires careful accounting of viscous drag of the contacting liquid. In contrast, Optical Waveguide Lightmode Spectroscopy suffers from neither of the problems and has been shown to provide accurate and precise kinetic adsorption data for several colloids/surface systems [51, 56].

In this work, Optical Waveguide Lightmode Spectroscopy is used to obtain continuous measurements of the deposition at elevated temperatures on variously modified surfaces. Gravimetry is used over longer time ranges to follow the temperature driven deposition, when deposited amount is above a detection limit of OWLS (~30mg.m^{-2}). The dynamic light scattering and static light scattering were used to follow aggregation in the bulk liquid phase. Finally, visualization of the deposits and inspection of surfaces was done by scanning electron microscopy (SEM), atomic force microscopy (AFM) or laser scan microscopy (LSM). In a recent work of Semmler et al. [25, 57], such imaging techniques are combined with reflection based technique to follow deposition of highly charged particles onto oppositely charged surfaces.

1.4.1.1 Deposition Studied by OWLS

Optical Waveguide Lightmode Spectroscopy (OWLS) was used to monitor deposition and kinetics driven by elevated temperatures. During the last decade, the interest in the field of sensor techniques has grown due to their ability to provide reliable and fast recognition of various colloidal substances as well as their ability to determine quantitatively the deposited mass. They monitor adsorption event and convert it into measurable signal. The range of

sizes which can be monitored by sensors is very broad. In principle, it can monitor adsorption of small molecules and ions, but they can be also used to monitor interaction of large polymer molecules or biomolecules.

A potential of thin monomodal planar waveguides to be used as optical sensors has been demonstrated by Lukosz and Tiefenhalter [58-61]. They demonstrated the ability of such sensors to be employed as humidity and gas sensors. Lately they have proposed and theoretically analyzed the sensitivity of the sensors to be applied as immuno- and affinity sensor for specific affinity reactions between ligand-receptor pair of molecules [62-65].

Nellen et al. [66-70] has further investigated the possibility to apply such sensor for specific immuno and affinity reactions. He has also tested the sensors as ion and pH sensors. OWLS technique achieved special recognition in a field of interactions among various proteins and surfaces, because of crucial importance for biocompatibility between different artificial surfaces and natural tissues in medical applications [56, 71-83].

New applications of sensors are focused on possibility to influence the specific interactions between interacting surfaces and colloidal suspensions. For instance, variously functionalized biopolymers are assembled on the oxide sensor surface in order to provide specific interaction for depositing colloid [72, 76, 84-91]. Other possibility to influence the interfacial interactions is to apply the electric field on the sensor surface [92-94].

On-line measurements made at elevated temperatures are not very common for optical based techniques. The presented work is first attempt to measure temperature driven deposition by OWLS. Next to the fact that a higher temperature usually modifies a native structure of biological molecules and as such is usually not wanted, the reason for lack of the work done with the optical methods at elevated temperatures can be connected with temperature dependence of system optical properties, which can make data analysis quite complicated. Even though, temperature driven fouling is quite common in nature and information provided are of great importance [34-36].

The primary aim of the presented work was to investigate the early deposition stages of various industrial proteinaceous plant extracts. As turned-out, the presence of electrolyte aqueous matrix of unknown composition makes the system rather complicated and characterization by OWLS is not straightforward. Before being able to explain such difficult depositing system, we had to understand response of a sensor , when exposed to electrolyte solutions of various composition. Accordingly, the thermodynamic equilibrium and kinetics of sensors responses for various electrolytes were monitored. The second step in systematic

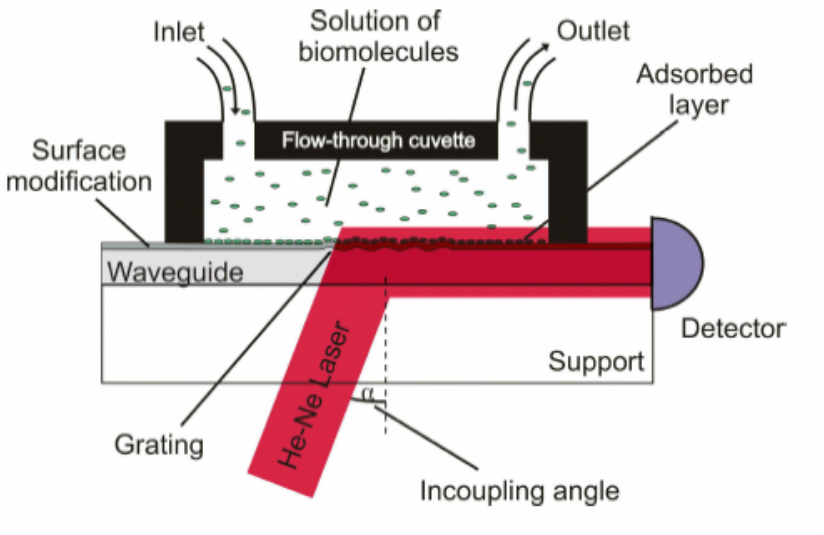

Figure 1-14. *OWLS flow-through deposition cuvette placed on the top of the waveguide. The incident polarized laser beam is coming from the bottom. The whole system is rotating left-right, and under incoupling angle* α *the beam is totally reflected and the light propagates along the waveguide plane. The maximum light intensities (resonance peaks) are recorded by detectors on both sides of the waveguides [95].*

investigation of the temperature driven deposition was to use well defined protein solution of a β-lactoglobulin. The kinetics of β-lactoglobulin deposition at elevated temperature prove ability of OWLS to monitor deposition for wide range of temperatures (25-80°C), pH (5.5-7.5) and IS (0-500mM). Finally, the knowledge of the model protein deposition and response of the sensor to electrolytes provide a solid base to investigate even challenging proteinaceous suspensions of unknown electrolyte composition during early stages of the process. Details about particular measurements are provided in corresponding sections of presented work.

Fundamental Principles

The fundamental principle of OWLS is based on the exponentially decaying electromagnetic field, which is probing the medium that covers the close vicinity of the planar waveguide surface (see Figure 1-14). The electromagnetic field carries information about the optical environment in which it propagates. Therefore, it probes all changes of the waveguide optical parameters and of the near distance from interface of the waveguide. Deposited material, due to its different optical properties from that of a bulk liquid, induces a change in measured effective refractive index *N*.

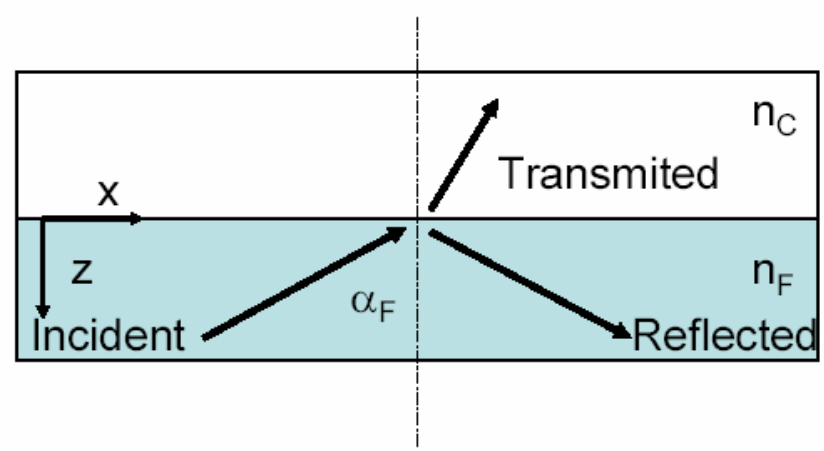

Figure 1-15. *Two different propagation of incident electromagnetic wave when impinging on optical interface.*

The planar optical waveguide (see Figure 1-2) consists of a waveguiding film F with refractive index n_F and thickness t_F, placed on a substrate S with refractive index n_S, and from the upper side of the waveguide is a cover medium with refractive index n_C (depositing solution). When polarized incident electromagnetic wave is impinging on optical interface F,C the boundary conditions of Maxwell's equation allows the wave to be transmitted or reflected from the interface, Figure 1-16. The angle of incidence can be related to the angle of transmition through Snell's law of refraction:

$$n_F \sin\alpha_F = n_C \sin\alpha_C \qquad (1.8)$$

As follows from Snell's Law, when $n_F < n_C$, the angle of the transmitted wave α_C is real, and the refracted wave will propagate in media C. On the other hand, if $n_F > n_C$ and incidence angle α_F becomes larger enough, the transmitted wave approaches tangency with the interfacial waveguide plane and more and more energy appears in the reflected wave. The incidence angle α_F, when transmitted angle α_C becomes 90º and the transmitted wave propagates parallel to the interfacial plane, is called critical angle ($\sin\alpha_{F,critical} = n_F / n_C$). Above the critical angle the total internal reflection from the interface occurs (see Figure 1-16). Even though the transmitted wave will not propagates in transmition media C and all incidence energy will be reflected back into the incidence media F, the amplitude of reflected electromagnetic wave will penetrate the close vicinity of the transmition media C, decreasing exponentially from the surface (see Figure 1-17).

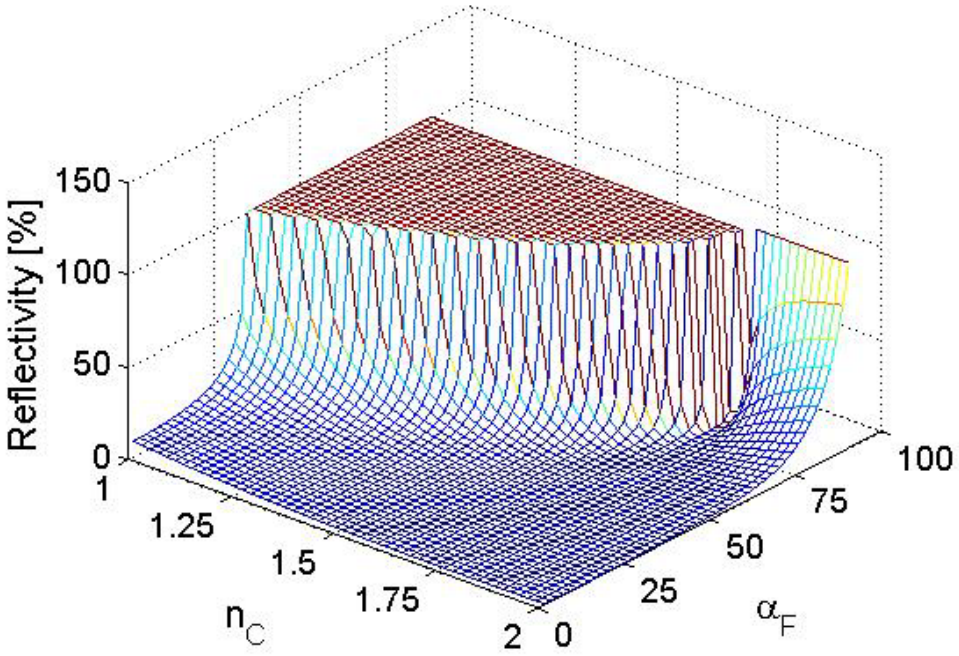

Figure 1-16. *Reflectivity from the optical interface as a function of incidence angle* α_F *for range of cover media refractive indices* n_C *typical for OWLS experiments (using typical* $n_F = 1.76$*).*

The penetration depth d_p of standing electromagnetic wave is defined as the distance required by electric field amplitude to fall to e^{-1} of its value at the surface, and is given by:

$$d_P = \frac{\lambda_0}{2\pi\left(\sin^2\alpha_F - \left(\frac{n_C}{n_F}\right)^2\right)^{0.5}} \qquad (1.9)$$

Where λ_0 denotes length of the electromagnetic wave in vacuum. The penetration depth gives an estimate of the sensed depth, which typically extends around 100~300nm from the surface for conventionally used silica-titania waveguide, covered by aqueous cover medium. The reflected wave will undergo a phase change Φ with respect to the incidence wave. The phase change is different for electric and magnetic component of the electromagnetic wave. However, there is mutual dependence between both components given by Fresnel's equations [96].

a)

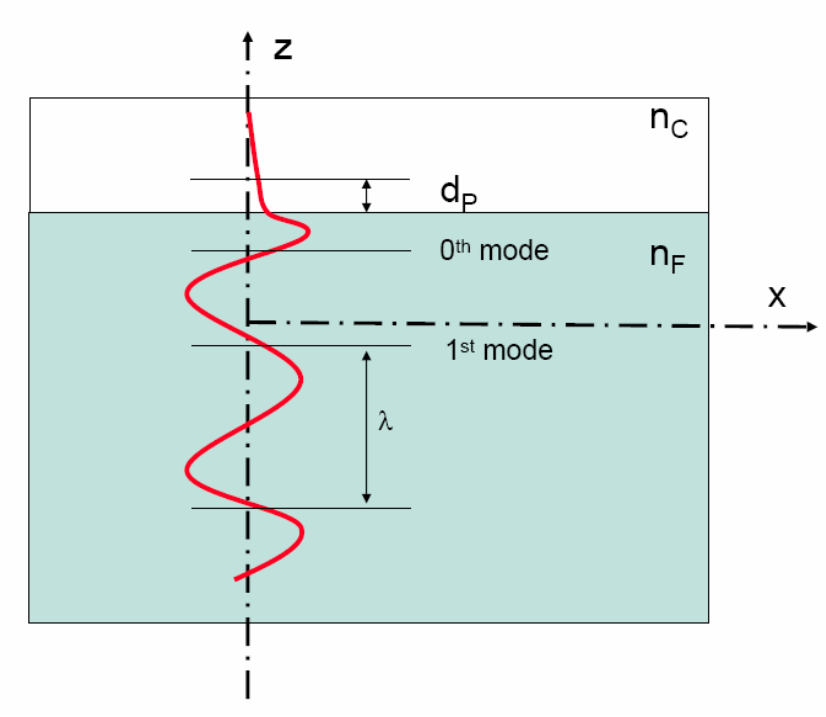

b)

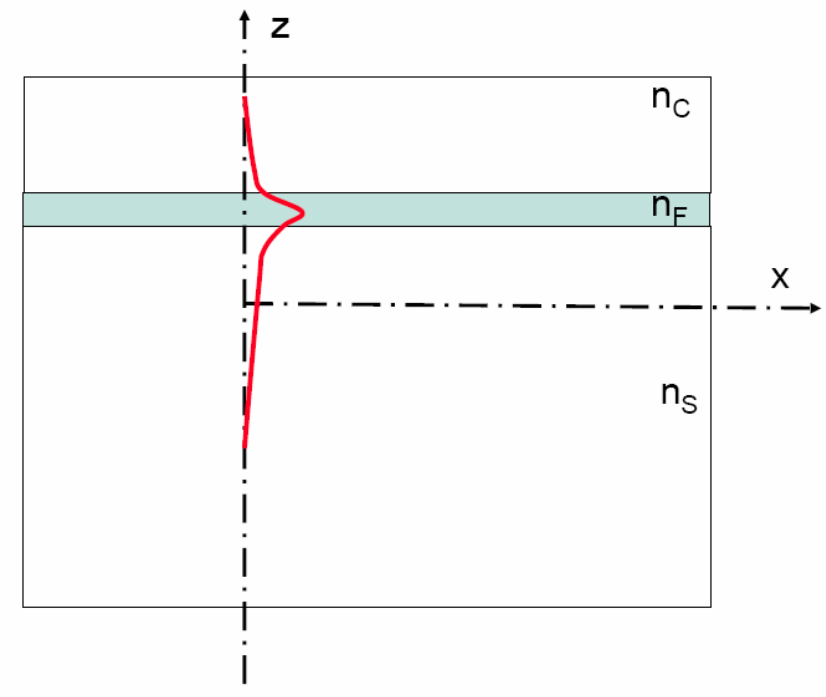

Figure 1-17a, b. *a) Standing wave amplitude established near totally reflecting interface. There is sinusoidal dependence of the amplitude on the distance in waveguiding medium F and is exponentially decreasing in rarer medium C. b) Depicts the situation for very thin waveguide, surrounded by two non-equal rare environments (like in a case of OWLS sensor), allowing only 0^{th} mode to be excited.*

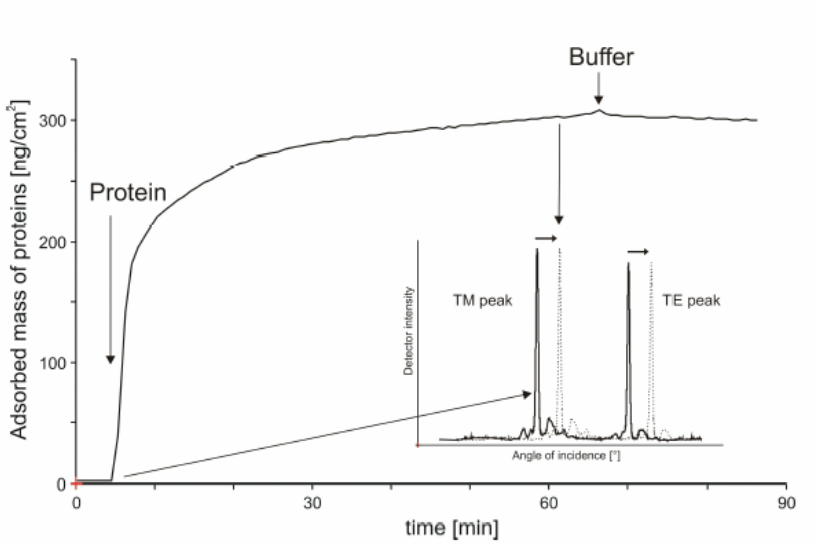

Figure 1-18. *Typical example of OWLS experiment. The measurement starts with baseline measurement, followed by introduction of depositing colloids (protein fibrinogen was used in this case). Adsorption of the colloids on the surface leads to the shift of the measured incoupling angle, which is recorded on-line. Et the end, the wash-out is done by blank buffer to follow desorption [73].*

Optical waveguide lightmode spectroscopy can monitor deposition starting from the molecular monolayer ranging up to the limit given by the saturation of the waveguide evanescent region. The OWLS was used in this work to track the deposition for surface coverage up to 30 $mg.m^{-2}$., which roughly corresponds to the thickness 30-50nm. As recently reported by Picart et al. [97], this upper bound is determined by the failure of the optical model which will be described below.

Optical waveguide lightmode spectroscopy is based on measurements of changes of the effective refractive index N of an optical waveguide when a thin film forms at the waveguide surface. Creation of the deposited layer is followed by polarizability increase at the solid-liquid interface. This consequently affects the phase shift of the electromagnetic wave reflected from F,C interface. Recorded α of resonance position is then detected under different angle of incidence (see Figure 1-18).

The measured angular position α of incident laser beam, where the maximum incoupling occurs, is the basic physical quantity provided by OWLS. By measuring the incidence angle α corresponding to the resonance maximum of the light incoupled into the waveguide it is

possible to determine an effective refractive index N of the light propagating along the waveguide as follows:

$$N = n_{air} \sin\alpha + l\lambda_0 / \Lambda \tag{1.10}$$

Where Λ is the grating period (2400 lines per mm for the sensor used in experiments), l is the diffraction order of the light ($l=1$), $\lambda_0=633nm$ is the wavelength of He-Ne laser beam, α is the incoupling angle for the resonance maximum and n_{air} is the refractive index of air [63].

Under resonance conditions, the phase change, that the electromagnetic wave undergoes during a round trip across the waveguide, is equal to an integer multiple of 2π. By round trip is meant the reflection at the interface (F,C), between the liquid bulk (C) and the waveguide film (F), crossing of the waveguide and then reflecting back at the opposite interface (F,S) , i.e. the interface between the waveguide film (F) and its glass support (S), as shown in Figure 1-17b. The zeroth order mode equation for such a standing electromagnetic wave propagating indefinitely along an asymmetric planar waveguide is given by:

$$0 = 2k_0 t_F \sqrt{n_F^2 - N^2} + \Phi_{F,S} + \Phi_{F,C} \tag{1.11}$$

The above equation gives a relation between the measured refractive index and the optogeometric parameters of the composite waveguide. Here $\Phi_{F,S}$ and $\Phi_{F,C}$ denote the phase shifts upon reflection from the waveguide surfaces, $k_0 = 2\pi / \lambda_0$ and n_F and t_F represent the refractive index of the waveguide film and its thickness, respectively. Assuming that all optical interfaces are abrupt and the layers are homogeneous and isotropic, the Eq. (1.11) can be written for two perpendicularly polarized components (transverse electric (TE) and the transverse magnetic (TM)) modes of the electromagnetic wave as follows:

$$\begin{aligned} 0 = {} & k_0 t_F \sqrt{n_F^2 - N^2} - \\ & \arctan\left[\left(\frac{n_F}{n_S}\right)^{2\rho}\left(\frac{N^2 - n_S^2}{n_F^2 - N^2}\right)^{1/2}\right] - \arctan\left[\left(\frac{n_F}{n_C}\right)^{2\rho}\left(\frac{N^2 - n_C^2}{n_F^2 - N^2}\right)^{1/2}\right] \end{aligned} \tag{1.12}$$

where $\rho = 0$ for the transverse electric mode TE and $\rho = 1$ for the transverse magnetic mode TM. We use the Eq. (1.12) expressed for two measured modes to calculate properties of the waveguide exposed to non-adsorbing media (water, buffer without protein). If the effective refractive indices N_{TE} or N_{TM} are measured and the refractive indices n_S and n_C of media surrounding the waveguide film are known, one can determine the refractive index of the waveguide film n_F and its thickness t_F.

When a thin film is present at the waveguide surface, its optical properties with respect to the reflected light can be represented by the excess polarization density γ [98]. The phase shift $\Phi_{F,C}$ at the waveguide surface can be also expressed in terms of γ, so that a generalized form of Eq. (1.12) is obtained [99], accounting for the presence of the thin film. This equation is then solved for γ, resulting in the following:

$$\gamma = \left(\frac{(n_F^2 - n_C^2)}{(n_F^2 - N(TE)^2)} \right)^{0.5} \left(\begin{array}{l} -k_o\, t_F (n_F^2 - N(TE)^2)^{0.5} + \\ +a\tan\left(\frac{(N(TE)^2 - n_C^2)}{(n_F^2 - N(TE)^2)} \right)^{0.5} + a\tan\left(\frac{(N(TE)^2 - n_S^2)}{(n_F^2 - N(TE)^2)} \right)^{0.5} \end{array} \right) \quad (1.13)$$

The excess polarization density is related to the distribution of optical density at the interface [99]:

$$\gamma = k_0 \int_0^\infty (\varepsilon_{\|}(z) - \varepsilon_0(z))dz = k_0 \int_0^\infty (n_{A\|}^2(z) - n_C^2(z))dz \quad (1.14)$$

Where the subscripts $\|$ all refer to the direction parallel to waveguide surface and the $n_{A\|}$ denotes the refractive index of adsorbed layer of an isotropic parallel plane at distance z from the waveguide surface. We note that the dielectric constant of the non-adsorbing medium is equal to the second power of its refractive index ($\varepsilon = n^2$). In the case of optically homogeneous isotropic film, the integral in the above equations simplifies to $M \cdot dc/d\varepsilon$, i.e. the total mass deposited per unit area M of the film multiplied by the derivative of the dielectric constant with respect to the mass concentration of deposits. Therefore, the deposited mass can be expressed in terms of the excess polarization density γ as follows:

$$M = \frac{\gamma}{k_0} \frac{dc}{d\varepsilon} \quad (1.15)$$

Using Eqs. (1.13) and (1.15) we can calculate the deposited mass per surface area, from the experimentally measured value of *N(TE)*. The term $dc/d\varepsilon$ is determined experimentally from the optical properties of particular studied system as a function of temperature as will be described later.

1.4.1.2 Deposition Studied by Gravimetry

Gravimetry measurements were used as complementary experiments for OWLS measurements. Gravimetry is probably the most conventional method to study macroscopic deposition. It is based on weighing the difference between adsorbent weight before and after the adsorption process, and therefore, its sensitivity is limited by the accuracy of the

weighting procedure. Studied silica, and steel surfaces in a form of thin plates were placed into deposition channel, paying special attention that velocity gradient at the surface would be comparable to conditions in industrial evaporator and OWLS experiments. More about gravimetry and fluid dynamic conditions inside the measurement device can be found in a chapter about hydrodynamic conditions 1.5. Deposited mass was determined as a difference between plate weight before and after the deposition using balance METLER TOLEDO UMT5 with declared accuracy of 0.5μg.

1.4.2 Techniques to Study Aggregation

Light scattering techniques are very popular tool to study bulk aggregation. When a beam of light passes through a colloidal dispersion, the particles or droplets scatter some of the light in all directions. When the particles are very small compared with the wavelength of the light, the intensity of the scattered light is uniform in all directions (Rayleigh scattering); for larger particles (above approximately 250nm diameter), the intensity is angle dependent (Mie scattering). Static light scattering (SLS) monitors the averaged intensity of scattered light as a function of scattered angle. On the other hand, dynamic light scattering (DLS) measures the time evolution of the intensity fluctuation of the scattered light at a fixed scattering angle. Fluctuation of the intensity in time can be related to the diffusion coefficient of colloids.

1.4.2.1 Static Light Scattering

In this work we were using SLS to follow the temperature driven aggregation of proteinaceous extracts in a liquid bulk. All measurements were performed with a small angle light scattering instrument (Mastersizer 2000 by Malvern). It allows monitoring the size, structure and kinetics of the aggregation. The advantage is the non- invasiveness of the technique. On the other hand, it requires the particles concentration to be sufficiently low. In order to avoid multiple scattering, measured samples have to be sufficiently diluted. This restricts the on-line monitoring only to diluted systems. The dynamic aggregation of the system was monitored by static light scattering (SLS), which measures intensity of the scattered light I as a function of scattering angle θ. The scattered light intensity can be expressed as [100].

$$I(q) = I(0)\,P(q)\,S(q) \tag{1.16}$$

where $I(0)$ is the zero angle intensity, $P(q)$ is the form factor depending on a particle size and shape and $S(q)$ is the structure factor depending on special arrangement of the primary particles in aggregate, and q is the scattering angle amplitude defined as:

$$q = 4\pi \frac{n}{\lambda} \sin\left(\theta/2\right) \tag{1.17}$$

where θ is the scattering angle, n the refractive index of the dispersant and λ the laser wave length in vacuum.

To extract the square radius of gyration $\left\langle R_g \right\rangle = \left\langle R_g^2 \right\rangle^{1/2}$ and the zero angle intensity $I(0)$ from the measured scattered intensity $I(q)$ as a function of scattering angle q, one can use several approximations of the structure factor $S(q)$ in the Guinier region ($qR_g < 1$). In our analysis the following approximation of $S(q)$ will be used:

$$S\left(q\right) \simeq \exp\left(-q^2 R_g^2/3\right) \tag{1.18}$$

If the primary particles are sufficiently small, so that $P(q)$ is very close to unity within the investigated range of q, then one can substitute the structure factor $S(q)$ by the intensity $I(q)$, since they are proportional. Validity of the assumption $P(q)$=1 can be verified by calculating the form factor from the Mie theory for the investigated particles, or it can be determined experimentally. Contributions to the average squared radius of gyration $\left\langle R_g^2 \right\rangle$ from, both the form factor $P(q)$ and the structure factor $S(q)$, are additive, so that:

$$\left\langle R_g^2 \right\rangle = \left\langle R_g^2 \right\rangle_{S(q)} + R_{g,p}^2 \tag{1.19}$$

Substituting $S(q)$ from Eq.(1.16) into Eq.(1.18) yields to the following expression:

$$\ln\left(\frac{I(q)}{P(q)}\right) = \ln\left(I\left(0\right)\right) + \frac{q^2}{3}\left\langle R_g^2 \right\rangle_{S(q)} \tag{1.20}$$

where $\left\langle R_g^2 \right\rangle_{S(q)}$ is the root mean square radius of gyration (and can be determined form the slope of the linear relation between $\frac{q^2}{3}$ and $\ln\left(\frac{I(q)}{P(q)}\right)$).

Besides the approximation of the $S(q)$ in the Guinier region (Eq. (1.18)), used in this work, there exist other two approximations, which can be used to relate $I(q)$ with q^2 resulting in the following forms [100]:

$$\frac{I(q)}{P(q)} = I\left(0\right) - \frac{q^2}{3}\left\langle R_g^2 \right\rangle_{S(q)} \tag{1.21}$$

$$\frac{P(q)}{I(q)} = \frac{1}{I(0)} + \frac{q^2}{3}\frac{\langle R_g^2 \rangle_{S(q)}}{I(0)} \tag{1.22}$$

It is understandable, that the three approximations which can be used to determine the average R_g will provide slightly different values of R_g. In this work we have chosen Guinier way of approximation to evaluate the average hydrodynamic radius of the sample aggregates.

1.4.2.2 Dynamic Light Scattering

DLS experiments were performed at the scattering angle 90º using the BI-200SM instrument (Brookhaven) with argon laser (Lexel 95-2, wavelength 514.5 nm) and a BI-9000 AT digital autocorrelator. In a case of a dynamic light scattering the time evolution of the intensity fluctuation of the scattered light is monitored at a fixed scattering angle. The fluctuation of the scattered light originates from the Brownian diffusion motion of colloids, and can be analyzed by constructing the intensity autocorrelation function $g^{(2)}(\tau)$, which has the following form:

$$g^{(2)}(\tau) = 1 + Ae^{(-2\langle D \rangle g^2 \tau)} \tag{1.23}$$

where τ is dimensionless time, A is a constant depending on the experimental set-up, and $\langle D \rangle$ is the average diffusion coefficient. The average hydrodynamic radius R_h can be determined using the Stokes-Einstein relation:

$$\langle D \rangle = \frac{kT}{6\pi\eta R_h} \tag{1.24}$$

Here one should note, that both obtained averaged R_g (from SLS) and R_h (from DLS) measured by different scattering methods are two independent moments of the colloidal size distributions, therefore, additional information about the broadness and the shape of the aggregates size distribution can be extracted.

1.4.3 Imaging Techniques

1.4.3.1 Scanning Electron Microscopy

SEM was used to visualize thin deposited layers on various surfaces, as well as to inspect continuity of the spin-coated polymer layers. In a typical SEM electrons are emitted from a

cathode and are accelerated towards an anode. The electron beam, which typically has an energy ranging from a few hundred eV to 40 keV, is focused by one or two condenser lenses into a beam with a very fine focal spot (nm-range). The beam passes through pairs of scanning coils in the objective lens, which deflect the beam in a raster fashion over a rectangular area of the sample surface. As the primary electrons strike the surface they are scattered by atoms in the sample. Through these scattering events, the primary electron beam effectively spreads and fills a teardrop-shaped volume, known as the interaction volume. Interactions in this region lead to the subsequent emission of electrons, which are then detected to produce an image. The most common imaging mode monitors low energy (<50 eV) secondary electrons. Due to their low energy, these electrons originate within a few nanometer from the surface. Using this technique, resolution of about 1nm is possible. Disadvantage of the method is possible destruction of the specimen structure by heat generated by electron beam and the technique is not compatible with liquid samples.

1.4.3.2 Atomic Force Microscopy

The AFM was used to visualize various sensor surfaces and spin-coated layers. The AFM consists of a cantilever with a sharp tip at its end, typically composed of silicon or silicon nitride with tip sizes in the order of nanometers. The tip is brought into close proximity of a sample surface. The Van der Waals force between the tip and the sample leads to a deflection of the cantilever. Typically, the deflection is measured using a laser spot reflected from the top of the cantilever into an array of photodiodes. In the contact mode operation, the force between the tip and the surface is kept constant during scanning by maintaining a constant deflection. In the non-contact mode, the cantilever is externally oscillated at or close to its resonance frequency.

The AFM has several advantages over the electron microscope. Unlike the electron microscope which provides a two-dimensional projection or a two-dimensional image of a sample, the AFM provides a true three-dimensional surface profile. Additionally, samples viewed by an AFM do not require any special treatment that would actually destroy the sample. While an electron microscope needs an expensive vacuum environment for proper operation, most AFM modes can work perfectly well in an ambient or even liquid environment. The main disadvantage in comparison to the scanning electron microscope (SEM) is the image size.

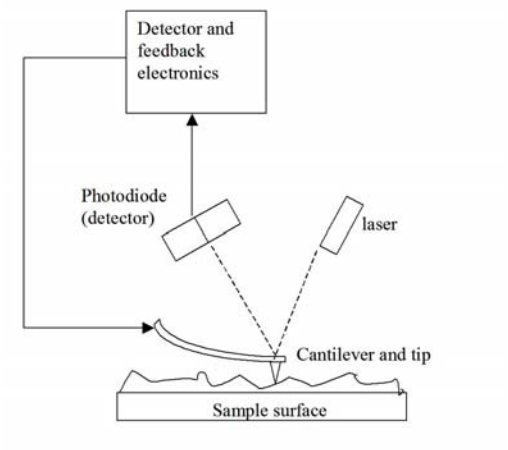

Figure 1-19. *Atomic force microscope block diagram.*

The SEM can show an area on the order of millimeters by millimeters and a depth of field on the order of millimeters. It may take several minutes for a typical region to be scanned with the AFM.

1.4.3.3 Laser Scan Microscope

Confocal LSM 410 from Zeiss Germany was used to visualize the structure of thicker deposited layers or to inspect spin-coated layer homogeneity. Confocal LSM is a valuable tool for obtaining high resolution images and 3-D reconstructions. In a laser scanning confocal microscope a laser beam passes a light source aperture and then is focused by an objective lens into a small focal volume. A mixture of emitted as well as reflected laser light from the illuminated spot is then recollected by the objective lens. A beam splitter separates the light mixture by allowing only the laser light to pass through and reflecting the emitted light into the detection apparatus. After passing a pinhole the emitted light is detected by a photo-detection device transforming the light signal into an electrical one which is recorded by a computer.

This optical technique has a resolution limit down to 400nm. Its advantage is the straightforward data interpretation and non-invasiveness. However, the typical dimension of proteinaceous colloid is below 10nm. Such dimensions can be resolved by SEM or AFM, but sample is often required to undergo manipulation or drying. Thus, the sensing techniques like OWLS are then often required to follow on-line deposition formation.

1.5 Hydrodynamic Conditions

As already sketched in Figure 1-1, next to the surface interaction forces, which usually act over very short distances, there are also transport forces, which bring particles close towards surfaces, where they can possibly deposit via surface interactions.

Table 1-3. *Scale-up comparison between important parameters influencing the hydrodynamic conditions in used experimental conditions and in industrial conditions.*

Scale-up / Parameter	OWLS Cell	Gravimetry Channel	Industrial evaporator
dimension	mm	cm	m
flow rates	$\mu l.min^{-1}$	$ml.min^{-1}$	$l.min^{-1}$
process duration	minutes	hours	days
mass deposited	$mg/\mu g.m^{-2}$	$g/mg.m^{-2}$	$kg/g.m^{-2}$
sample consumption	cm^3	dm^3	m^3

Here belongs Brownian diffusion, convective transport and various external forces like gravitational force, external electromagnetic force etc. In aqueous solutions, whose viscosity and density are constant, the Navier-Stokes equation is used to describe the transport of incompressible fluid. Since hydrodynamic conditions are among the crucial factors influencing the deposition [5, 6, 53, 54, 101] we had to take them into account while designing laboratory experiments. In Table 1-3 the most important characteristic parameters influencing the hydrodynamic conditions are summarized for three various apparatuses used to study the fouling.

Design of laboratory deposition experiments for different scale-ups required to assess the hydrodynamic conditions for used experimental devices (OWLS deposition cell, gravimetry channel, industrial evaporator). With OWLS one can measure deposited amounts from molecular level up to 30 $mg.m^{-2}$ during a time scale of minutes. Gravimetry experiments were designed in a way to follow deposition above 50 $mg.m^{-2}$ and runs lasted several hours. For industrial conditions deposited amounts reached several $g.m^{-2}$ during the process runs lasting a few days. To calculate liquid velocity profile close to the industrial evaporator surface the model of free falling laminar film was used [102]. Subsequently, for determined industrial

conditions we had to calculate the flow rate profile above depositing surfaces in laboratory conditions adopting a model of laminar flow between two infinite parallel planes [102], using dimensions of OWLS deposition cell and gravimetry channel.

1.5.1 Laminar Flow in a Free Falling Film.

To evaluate hydrodynamic conditions in the industrial evaporator we considered the flow of aqueous liquid suspensions along inclined flat surface (see Figure 1-20). The viscosity and the density of the liquid was assumed to be constant. Under assumption of the steady flow the momentum balance is:

$$\{rate\ of\ momentum\ in\} - \{rate\ of\ momentum\ out\} + \{sum\ of\ forces\} = 0 \qquad (1.25)$$

In a case of evaporator, the forces entering the third term may be gravity and pressure force. Using dimensions provided in Figure 1-20, the general form of Eq.(1.25) can be rewritten:

$$LW\tau_{xz}\big|_x - LW\tau_{xz}\big|_{x+\Delta x} + W\Delta x\rho v_z^2\big|_{z=0} - W\Delta x\rho v_z^2\big|_{z=L} + LW\Delta x\rho g\cos\beta = 0 \qquad (1.26)$$

Where L is length of evaporator [m], W is the width [m], ρ is liquid density [kg.m^{-3}], v liquid velocity [m.s^{-1}], g is gravitational acceleration [9.8 m.s^{-2}], τ_{xz} is shear force per unit area and β is the angle [°] between evaporator surface plane and vertical ax. Because the v_z profile is the same along the evaporator for each value of x the third and fourth term in equation just cancels each other. After dividing by $LW\Delta x$ and for Δx approaching zero we obtain differential equation for momentum flux τ_{xz}.

$$\frac{d}{dx}\tau_{xz} = \rho g x\cos\beta \qquad (1.27)$$

Integration of the equation, applying boundary condition of liquid-air interface, assuming zero velocity gradient:

$$B.C.1:\quad at\quad x = 0,\quad \tau_{xz} = 0 \qquad (1.28)$$

Gives the momentum-flux distribution linearly depending on distance from the free surface:

$$\tau_{xz} = \rho g x\cos\beta \qquad (1.29)$$

Further we assumed, that the Newtonian liquid is a good approximation to the extract falling down the evaporator surface.

$$\tau_{xz} = -\mu\frac{dv_z}{dx} \qquad (1.30)$$

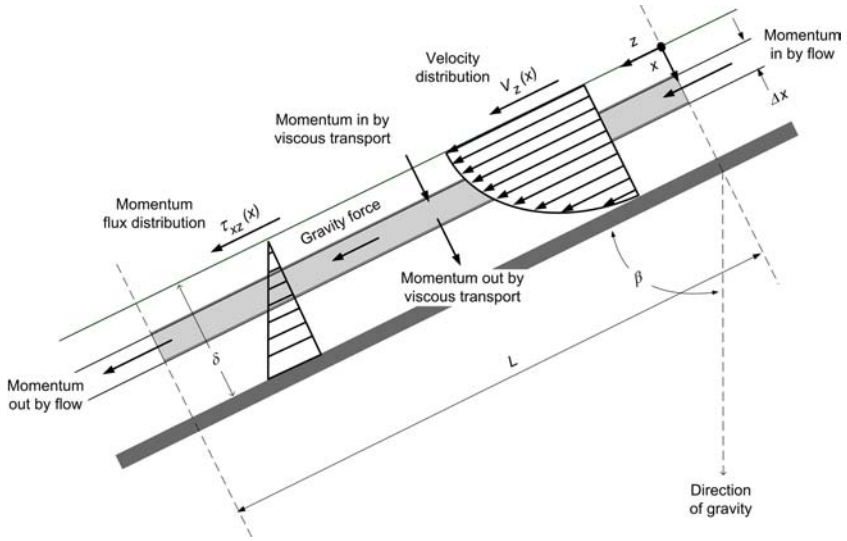

Figure 1-20. *Flow of laminar viscous isothermal liquid film under influence of gravity. Slice of thickness Δx over which momentum balance is made. The y-axis is pointing outward from the plane of figure.*

This states that the shear force τ_{xz} per unit area is proportional to the negative of the local velocity gradient $\frac{dv_z}{dx}$. Proportionality is given by dynamic viscosity of the fluid μ [Pa.s]. Substitution of this equation to the Eq. (1.29) gives differential equation for the velocity distribution in the film:

$$\frac{dv_z}{dx} = -\left(\frac{\rho g \cos\beta}{\mu}\right) x \tag{1.31}$$

The integration of the equation using boundary condition

$$B.C.2: \quad at \quad x = \delta, \quad v_z = 0 \tag{1.32}$$

leads to the expression for the velocity distribution in the free falling film:

$$v_z = \frac{\rho g \delta^2 \cos\beta}{2\mu}\left[1 - \left(\frac{x}{\delta}\right)^2\right] \tag{1.33}$$

The position of evaporator is usually vertical so the $\cos\beta = 1$. The thickness of the free falling film δ can be estimated from the volume rate of the flow Q [$m^3.s^{-1}$].

$$\delta = \sqrt[3]{\frac{3\mu Q}{\rho^2 g W \cos\beta}} \tag{1.34}$$

The validity of the model is only satisfied for the laminar flow. For the vertical walls the Reynolds number is used as criterion.

- laminar flow without rippling $\mathrm{Re} < 25$

- laminar flow with rippling $25 < \mathrm{Re} < 2000$
- turbulent flow $\mathrm{Re} > 2000$

Where Re number is given as

$$\mathrm{Re} = \frac{4\delta v_{z,ave}\rho}{\mu} \tag{1.35}$$

And averaged velocity is

$$\mathrm{v}_{z,ave} = \frac{\rho\, g \cos\beta}{3\,\mu}\,\delta^2 = \frac{2}{3}\mathrm{v}_{z,max} \tag{1.36}$$

Using model described above, we have made the estimation of the velocity gradient above the evaporator surface for range of possible conditions. In Figure 1-21 we have calculated velocity gradient for typical dimensions of industrial evaporator used to concentrate a proteinaceous liquid suspensions. For the calculation we took the width of evaporating surface to be W=2.15m (dimension of evaporator surface shown in Figure 1-20 in y direction), wide range of expected mass flows (5-60kg.min^{-1}) and wide range of viscosities (0-0.1Pa.s). Velocity gradients inside the black circle determine the values of surface gradient to be designed in gravimetry channel and OWLS cell. Those values are reasonably close to the values measured for the native proteinaceous plant extract with concentration 13%, which is investigated later. At temperature around 65°C is the density of the extract 1049kg.m^{-3} and dynamic viscosity 0.02Pa.s. In Figure 1-22 Reynolds numbers are evaluated, corresponding to the gradient data points shown in Figure 1-21.

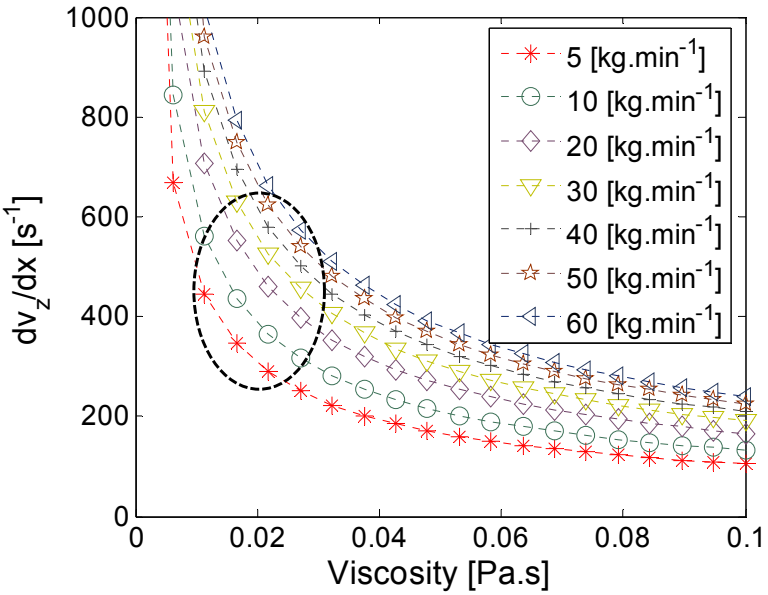

Figure 1-21. *The range of velocity gradients expected in the industrial evaporator. Black circle determines the range of gradients to be reached in gravimetry channel and OWLS cell.*

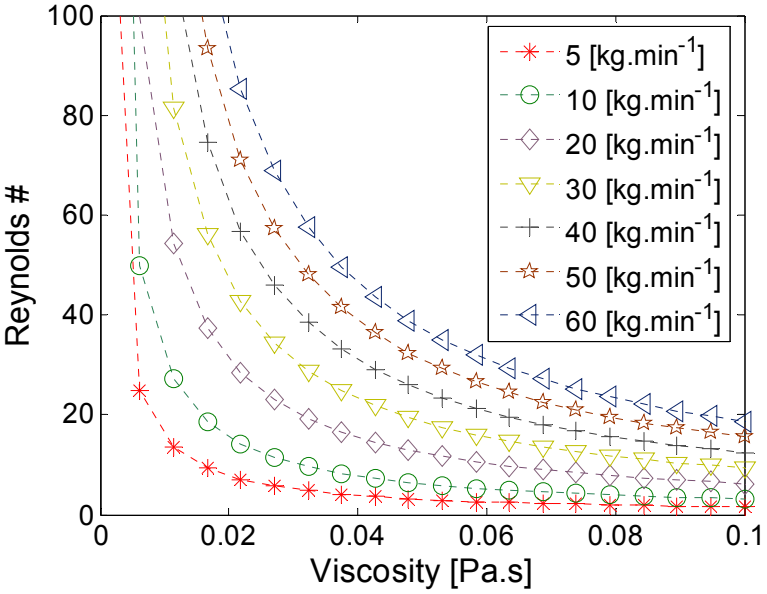

Figure 1-22. *Reynolds numbers for the range of conditions occurring in industrial evaporator used to evaporate plant extract. Data points correspond to those showed in Figure 1-21.*

1.5.2 Laminar Flow in a Narrow Slit Between Parallel Plates

In comparison to the industrial evaporator, which is well described by free falling laminar flow model, the liquid in laboratory experiments will flow between two parallel plates in a narrow slit (see Figure 1-23). The laminar flow of fluid in a narrow slit may be analyzed in the same fashion as a momentum balance described in a chapter about laminar flow in a free falling film (see section 1.5.1). Again we consider constant density in very long slit surrounded by two plates. Using dimensions provided in Figure 1-23, the general form of the steady flow momentum balance Eq.(1.25) can be rewritten:

$$LW\tau_{xz}\big|_x - LW\tau_{xz}\big|_{x+\Delta x} + W\Delta x\rho v_z^2\big|_{z=0} - W\Delta x\rho v_z^2\big|_{z=L} + LW\Delta x\rho g\cos\beta + WL\Delta x(p_0 - p_L) = 0 \tag{1.37}$$

Where $(p_0 - p_L)$ is the pressure drop along the evaporator. Following the same procedure as described in a previous chapter 1.5.1 the expression for momentum flux distribution is obtained.

$$\tau_{xz} = \left(\frac{P_0 - P_L}{2L}\right)x \tag{1.38}$$

Where $P = p - \rho gz$. Under assumption of Newtonian liquid, the substitution of Eq. (1.38) into (1.30) gives the following differential equation for the fluid velocity:

$$\frac{dv_z}{dx} = -\left(\frac{P_0 - P_L}{2\mu L}\right)x \tag{1.39}$$

Integration of the Eq. (1.39), applying boundary conditions:

$$B.C.2: \quad at \quad x = \pm B, \quad v_z = 0 \tag{1.40}$$

Leads to the expression of the velocity distribution along the narrow slit:

$$v_z = \frac{(P_0 - P_L)B^2}{4\mu L}\left[1 - \left(\frac{x}{B}\right)^2\right] \tag{1.41}$$

To derive relation between velocity profile and the rate of the flow we have applied the Hagen-Poiseuille law. The volume flow rate Q is product of the cross-section area and the averaged velocity. From Eq. (1.36) we get:

$$Q = \frac{dV}{dt} = v_{z,ave}WB = \frac{4}{3}v_{z,\max}WB = \frac{4}{3}\frac{(P_0 - P_L)B^3W}{2\mu L} \tag{1.42}$$

Expressing term $(P_0 - P_L)$ from the Eq. (1.42) and substituting it into the velocity distribution Eq.(1.41), the final form of the velocity profile in a narrow slit is obtained:

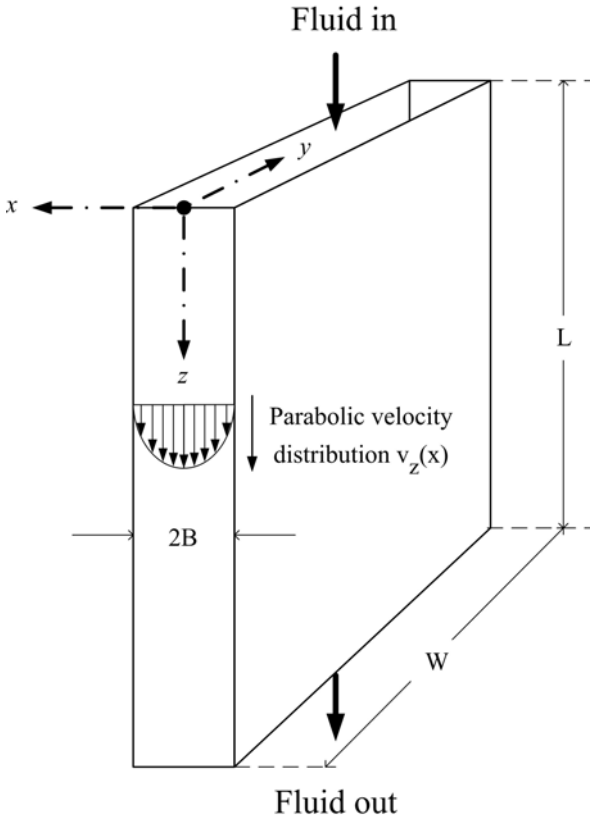

Figure 1-23. *Laminar flow in a narrow slit.*

$$v_z = \frac{3Q}{4BW}\left[1-\left(\frac{x}{B}\right)^2\right] \tag{1.43}$$

Here we can summarize the assumptions which are implied in the used model. The flow is laminar and the Re number has to be below 2100. For this system it is customary to define Reynolds number by:

$$\mathrm{Re} = \frac{2B\left\langle v_{z,ave}\right\rangle \rho}{\mu} \tag{1.44}$$

Liquid is Newtonian and its density is constant. The flow is in steady state and any end effects are neglected. Actually, the entrance length $L_e = 0.07B\,\mathrm{Re}$ is usually the criterion required for build-up of the flow parabolic profile. To prevent the effect of non-steadiness of the flow entering the gravimetry channel, the first deposition plate was not involved for deposition study, thus was used to establish the steady flow conditions.

1.5.2.1 Design of Gravimetry Channel

Experimental set-up to study the deposition is based on assumption of a laminar flow between parallel planes, which occurs in two rectangular channels shown in Figure 1-25. The two

channels are formed by an intermediate plane, depicted as blue plates in the figure, constituted by the samples under investigation and by two aluminum surfaces of the instrument body. These two surfaces form two narrow slits of gravimetry channel and have well defined dimensions (to provide well defined stress on the surface). The detail of the gravimetry channel cross section is provided in the figure. The suspension is fed at one side of the channel and goes out at the opposite one. The sample plates are in contact with liquid on both sides. The channel thickness can be easily modified if needed. The channel can be positioned between horizontal and vertical position to simulate different flow conditions, with respect to gravity. The body of the instrument can be heated/cooled between 0-100°C in a temperature-controlled bath. Pre-heating/pre-cooling compartments taking the investigated suspensions at the desired experimental temperature. The peristaltic pump delivers the suspension at various flow rates.

To design the gravimetry channel we had to choose "reasonable" sizes of the W (channel width) and B (half of the slit width), see Figure 1-23 for details. From practical point of view the size of gravimetry channel was limited by the amount of extract necessary to be consumed for each experiment, which increases from microliters for the sensor experiments to several hundreds of milliliters needed for the gravimetry measurements (see Table 1-3). The experimental scale-up, of course, multiplies the sample consumption by several orders of magnitude for the equivalent duration of the experimental run.

Based on the chosen channel dimensions, the velocity profile along the slit and the velocity gradient close to the surface were evaluated using Eq. (1.43) for range of volumetric flowrates. The physical properties of liquid taken for calculation were the same as described in section 1.5.1. The ranges of volumetric flowrates providing the surface velocity gradients similar to the one calculated for the industrial evaporator were determined (see Figure 1-24 for determined velocity gradients in gravimetry channel and Figure 1-21 for condition in industrial evaporator). Finally, considering the acceptable sample consumption for the channel with $W=18mm$, we have chosen slit thickness to be $B=0.25mm$. For the selected dimensions of the gravimetry channel we were able to achieve the required velocity gradients at the surface within reasonable range of flowrates (5-60 $ml.min^{-1}$), which are easy to be achieved by a common peristaltic pump (see Figure 1-24). Deposited plates have a shape of squares 18x18mm and a thickness of the plates is 0.15mm. Two materials used to produce the depositing plates were silica glass (IEP=3) and stainless steel (IEP=5). The both materials are widely used for transport of biological fluids. Moreover, the silica glass is material comparable with oxide sensor material, therefore, the gravimetry measurements can be

compared with OWLS measurements and at the same time the stainless steel plates can be compared with industrial evaporator measurements, where stainless steel is used as surface material.

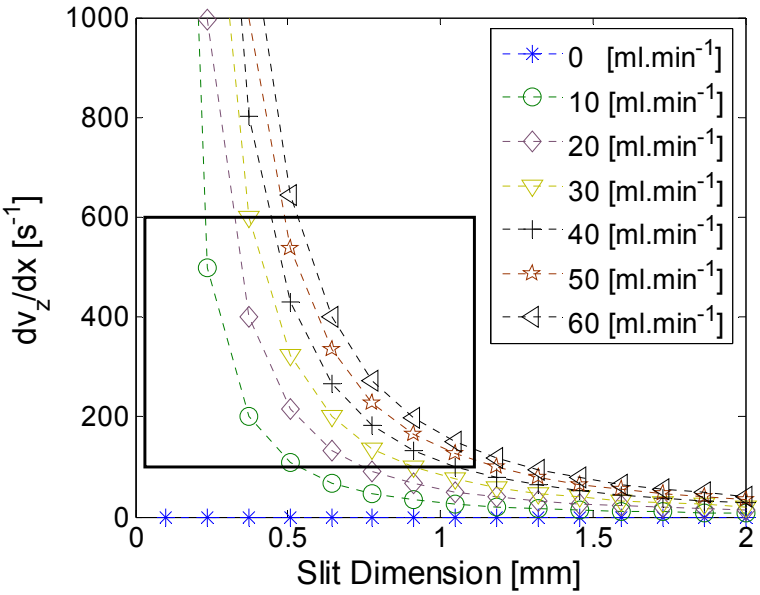

Figure 1-24. *The range of the velocity gradients expected in the narrow slit of the gravimetry channel. Black square determines the range of gradients calculated for operating conditions in the industrial evaporator.*

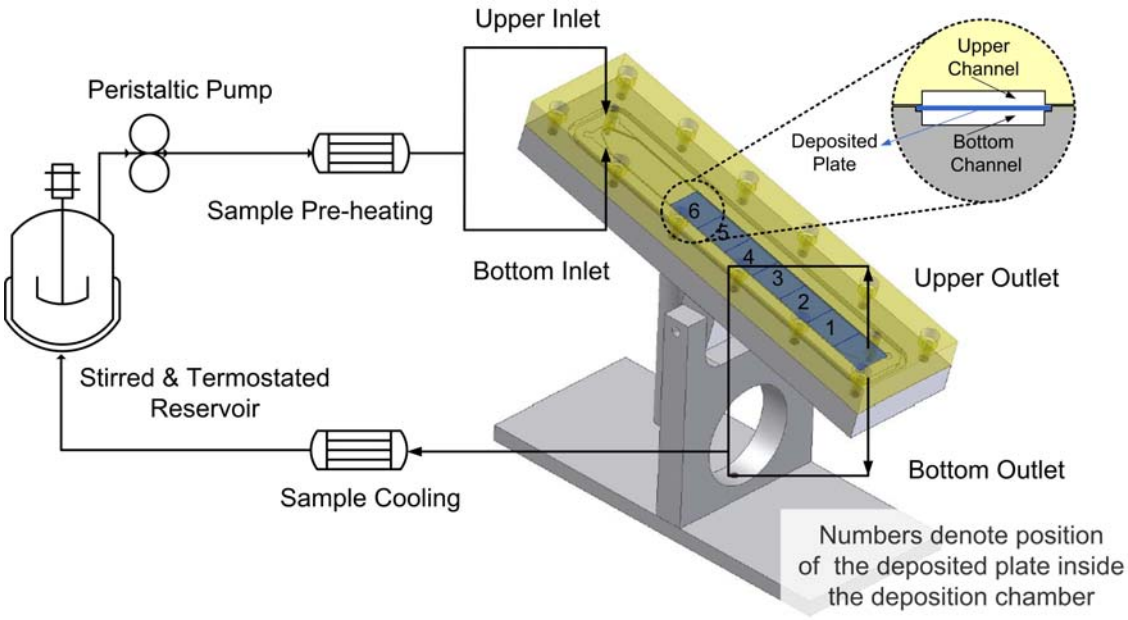

Figure 1-25. *Flow chart of gravimetry experiments.*

1.5.2.2 Design of OWLS Deposition Cell

Under assumption, that the flow inside OWLS deposition cell can be considered as the flow in a narrow slit, described in section 1.5.2, the velocity gradients close to the sensor surface can be estimated for various flowrates. The dimensions of the OWLS deposition cell are *B=0.4mm, W=1mm and L=8mm*. Again, the physical properties of a liquid considered for hydrodynamic conditions in the OWLS deposition cell are the same as for the liquid used for industrial evaporation which is described in section 1.5.1. The flowrates providing the required velocity gradients at the sensor surface can be read-out from the Figure 1-26. Such flowrates can be easily achieved in OWLS deposition cell.

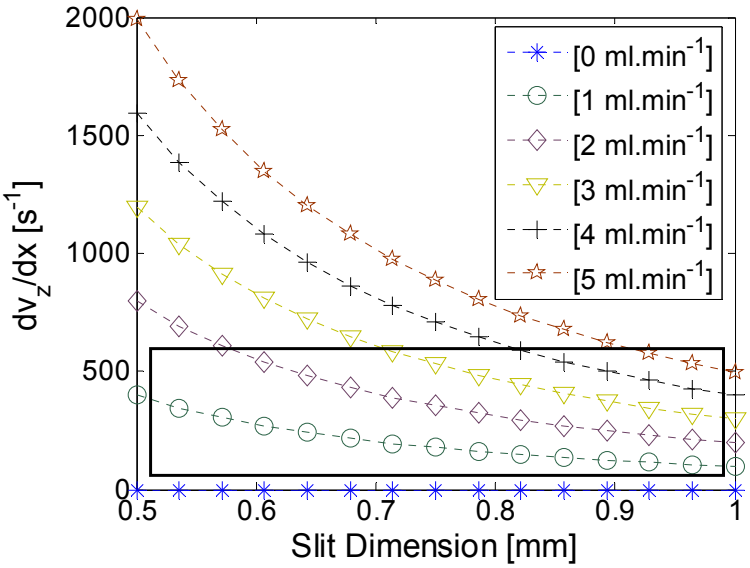

Figure 1-26. *The range of the velocity gradients expected in the narrow slit of the OWLS deposition channel. The black square determines the range of gradients calculated for operating conditions in the industrial evaporator.*

2 Measurements of Surfactant Isotherms Using Optical Waveguide Lightmode Spectroscopy

Abstract

Experimental study of sodium dodecyl sulfate (SDS) adsorption on water-polystyrene interface under a wide range of temperatures is presented. Although there is a lot of information about SDS adsorption isotherm on polystyrene (PS) in aqueous solution at ambient temperature, a lack of information is available for higher temperatures and ionic strengths, which are often used in industrial applications. We used optical waveguide lightmode spectroscopy (OWLS) to measure SDS adsorption isotherms on PS thin films for solution concentration up to the critical micelle concentration (CMC), in a range of temperatures between 25-65°C. Knowledge of these adsorption isotherms should allow better control of latex aggregation processes.

2.1 Introduction

Characterization of surfactant adsorption to water-polymer interfaces has practical importance in many applications, including polymer processing, detergency, coatings or metal treatment. Kinetics of adsorption is of interest in dynamic systems, where variations of the ionic strength, pH or temperature in a liquid phase significantly influence the rate of adsorption, such as in unsteady separations or colloidal deposition systems.

Understanding the adsorption equilibrium leads to better appreciation of surfactant distribution in a given system. A general feature of surfactant aqueous solutions is that surfactant molecules are distributed among micelles, bulk solution and available surface interfaces. Adsorption at solid-liquid interface is influenced by many factors, such as properties of polymer surface (hydrophobicity, ionic function groups, geometry of surface), structure of surfactants, bulk phase properties (electrolyte concentration, pH) and temperature. Previously reported isotherms for sodium dodecyl sulfate on polystyrene were mostly based on material balance of the system in equilibrium, using analytical methods such as titration or ion chromatography [103, 104].

The use of optical methods, which study properties of the adsorbed film directly, is an alternative approach. Turner [105] used neutron reflection and attenuated total reflection infrared spectroscopy to measure SDS adsorption on spin-coated ultrathin polystyrene films. Other optical methods like the reflectometry [106], small angle x-ray scattering [107] have been used for surfactant adsorption investigation on latex particles.

2.2 Theoretical Background

OWLS is based on monitoring the resonance spectra of linearly polarized light, coupled by diffraction grating into the waveguide. Positions of resonance peaks are measured for transverse magnetic and transverse electric modes. When small polarized molecules are adsorbed on a waveguide surface, reflection of polarized laser beam from the interface is changed, resulting in the shift of a resonance peak.

Details about the technique, as well as physical principles and model used to calculate the signal can be found in the background section 1.4.1.1. We use an optical model proposed recently by Mann [99], in order to determine the adsorbed amount of surfactant. The model is based on the concept of optical invariants, which describe the adsorbed layer in analogy with Gibbs interface, as a difference between response of the Fresnel optical interface and the true optical response in terms of the surface excess polarization densities γ [108] Eq. (1.13).

Compared to the model used for thin isotropic homogeneous films [51], this approach avoids specifying the adsorbed film thickness and its optical density, given by film refractive index, while the excess polarization density is directly proportional to the adsorbed mass of the solute. Since the optical density (refractive index) of adsorbed SDS layer is not known quantitatively, it is not possible to express measured surface excess polarization densities in terms of absolute adsorbed amount. The refractive index of surfactant bulk solution is different from the refractive index of the solution close to the interface, because the oriented surfactant molecules at the interface change the refractive index in close vicinity of the surface. Thus the usual experimental approach to determine the deposited mass through bulk refractive index increment as a function of concentration can not be used. Hence, to interpret such data correctly the orientation of molecules had to modeled and used to determine the deposition data in terms of mass.

2.3 Experimental

Experiments were performed using the OWLS 110 instrument and OW 2400c waveguides supplied by Micro Vacuum Ltd., Budapest, Hungary. Waveguides deposited on a glass substrate were films approximately 175 nm thick, made of mixed oxide titania-silica (Ti/Si=3) and coated with a thin layer (20 nm) of polystyrene. Parameters of the waveguides provided by the manufacturer were: refractive index of the glass substrate 1.5258, grating period Λ = 416.7 nm, wavelength of laser light λ = 632.8 nm. Refractive index of the air was taken as 1.000267. Refractive index of the bulk solution was measured by differential refractometer at 298K. Adsorption experiment was carried out under constant temperature at 25, 45 and 65°C. Since the refractive indices are dependent on temperature we analyzed the influence of the expected refractive index changes on calculated excess polarization density. Used values did not significantly influenced results.

Sodium dodecyl sulfate was obtained from Sigma-Aldrich (CAS number 151-21-3). SDS was purified by recrystalization from ethanol four times to remove impurities. It was previously observed [105], that SDS hydrolyzes in a few days and the hydrolysis product - dodecanol, is a competitive adsorbate to SDS.
The polystyrene used in this study for the spin-coating was Polystyrene Standard 30'000 from Sigma-Aldrich (Product Number 81408) with Mp=32500, Mn=31000, Mw=32000. Before spin coating the PS film, sensor chips were pretreated as follows: Chips were etched in 30mM aqueous solution of Potasium Monopersulfate Triple Salt (Cas # 27222-65-5) during four hours. They were silanized in Hexamethyldisilazane atmosphere for one hour and left to relax at 150°C over night. Pretreatment of the sensor chips prevents dewetting of the spin-coated polystyrene layer. PS films were prepared by spin-coating from 1wt% of polystyrene solution in toluene at 3500 rpm for 30 seconds [38]. Thickness of prepared ultrathin PS film measured by OWLS was approximately 20 nm.

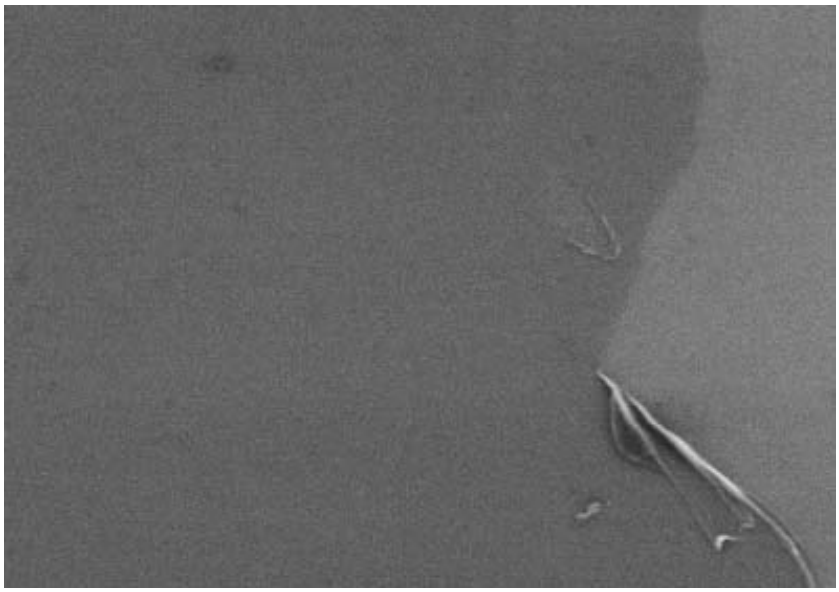

Figure 2-1. *SEM picture of the coated polystyrene film. The left side of the image is the homogeneous polystyrene film, the right side is the edge of scratch made to the film. The area of the image is 6x10 micrometers*

Re-crystallization of the PS films is recommended to unify and smooth polystyrene surface. There are many papers, referring to properties of the ultrathin PS films, which are quite different from the bulk polystyrene [39, 41, 44, 45, 48, 50, 109]. Generally, for the ultrathin PS films decrease of the glass-transition temperature was observed compare to the bulk polystyrene. Decrease depends on the thickness of the films and on the chain-length of used PS molecules. Data available in literature for polystyrene films comparing with our system are quite scattered and the transition temperatures are in wide range 293-373K. Therefore we used 100°C under vacuum atmosphere and left the film to cool down over night until it reached the ambient temperature. The homogeneity and the complete coverage of coated films were checked by Optical Microscopy and in some cases by Scanning Electron Microscopy (see Figure 2-1).

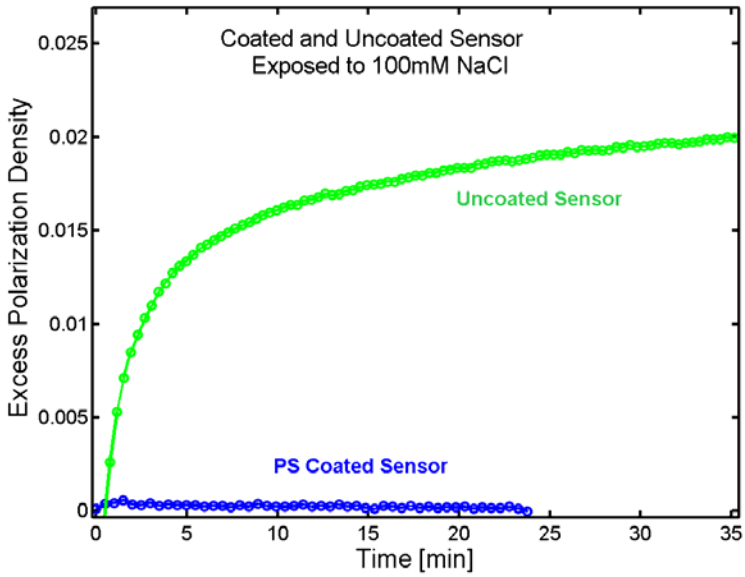

Figure 2-2. *On-line, in- situ measurement of the waveguide deprotonation kinetic for the bare uncoated oxide and for the PS coated surface. The PS layer creates insulation, protecting underneath oxide to be charged.*

To verify whether the coverage of polystyrene is complete, the comparison between response of the bare uncovered chip and the coated one to the sodium chloride solution was made (Figure 2-2). Uncoated bare porous oxide waveguides show a strong optical response when exposed to electrolyte solutions [110] and this response is consistent with the waveguide charging. We observed long lasting charging kinetic, presumably due to the surface charging inside of the waveguide nanopores.

Since spin-coating of the thin polymer layer is very delicate process, the continuity of such nanometer thick layers had to be verified by means of imaging techniques like SEM, AFM or LSM, which are beyond the scope of this chapter. More details about spin-coating of thin polymer layers are provided as an Appendix at the end of this chapter.

On the other hand, the waveguides coated by ultrathin polystyrene film show a much smaller optical response to the same electrolyte solution, which corresponds to the change in cover media refractive index, but waveguide itself remains uncharged, since is protected by the barrier of the hydrophobic polystyrene film.

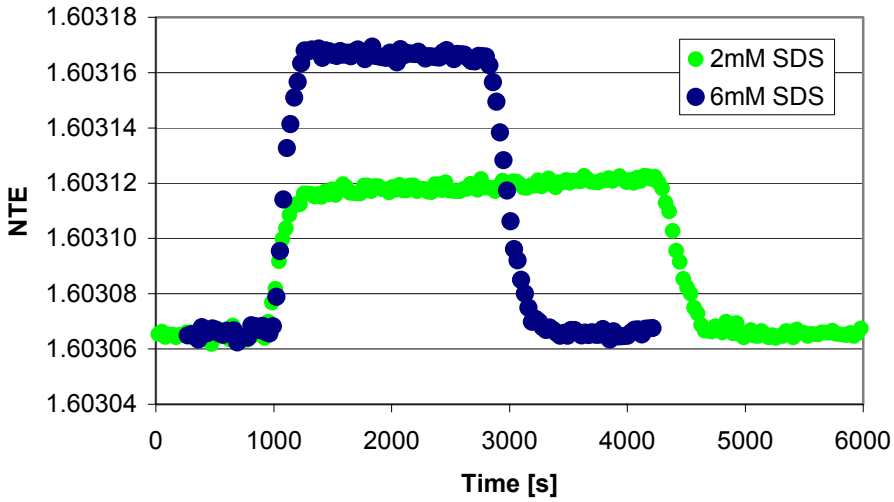

Figure 2-3. *On-line in- situ measurement of SDS adsorption kinetic on PS. Effective refractive index for transverse electric mode plotted versus time. For the first 1000 seconds PS film is exposed to water. Than solution replacement occurs (shown for two SDS concentrations at 25°C). Equilibrium is reached within 5 minutes and saturation remained constant for a long time. Than we desorbed SDS reversibly.*

The peristaltic pump was used to push the surfactant solutions through a cuvette attached to the waveguide surface. The flow through the measuring cuvette was in the laminar regime with the flow rate 1 ml/min. When the surface was saturated by SDS, the flowrate was set to zero and several measurements of the saturated surface were performed. Concentration of the bulk SDS solution varied in a range from 1.10^{-4} up to 5.10^{-3} mol.dm^{-3}. The refractive index of the bulk solutions at room temperature was measured by the differential refractometer MERCK-La Chrome RI detector, type L-7490.

The coated polystyrene film was left at least 30 minutes in Millipore water before each experiment in order to establish stable signal, used to determine the thickness and refractive index of the waveguide. SDS solutions were stored in the plastic bottles and were pushed by the pump into the cuvette where adsorption took place. Consequently, the SDS solution was sampled for at least 10 minutes until the adsorption equilibrium was reached. The equilibrium occurred in a few minutes as can be seen from the illustrative record of two effective refractive index measurement shown in the Figure 2-3. After measuring the equilibrium saturation, the surface was desorbed by Millipore water until the steady response was obtained and surface was left to relax in double distilled water for the next experiment.

2.4 Results and Discussion

When anionic SDS with a hydrophobic tail was added to the water, strong response of the coated sensor surface was measured. It is caused by creation of concentrated, negatively charged surfactant layer.

The composition and spatial orientation of the adsorbed molecules in a close vicinity of the surface could have significant impact on the refractive index of the adsorbed layer, when compared to the bulk solution. The orientation of the molecules in the bulk solution bellow critical micelle concentration is essentially random. Moreover, polarizability of molecules may be different in compact adsorbed layer. For this reason we present relative adsorbed mass, rather than absolute adsorbed amounts, where the adsorbed amount was scaled by the plateau value.

Comparison between the relative adsorption isotherms measured by four different techniques at the ambient temperature, shows that the isotherm measured by OWLS agrees well with other results for the same system published in literature (see Figure 2-4). For SDS concentration above 5.10^{-3} $mol.dm^{-3}$ adsorbed amount reaches a plateau. Reported absolute values of plateau surface coverage were measured to be around $4\mu mol.m^{-2}$ [105, 111].

When we compare the isotherm measured here with those determined by other optical methods ATR-FTIR and NR spectroscopy measured by Turner et al., we see that in agreement with our results, the amount of SDS adsorbed from 1mM aqueous solution is approximately half of the amount adsorbed at the isotherm plateau, measured at the ambient temperature. Plateau is reached well before the CMC concentration in the bulk.

Further increase of SDS concentration in the bulk solution leads to micelle formation and the adsorbed plateau remained constant or decreased slightly, which was suggested to be due to SDS impurities. However, we always observed a certain decrease for concentrations above CMC, even we purified SDS by recrystallization as suggested. This may be due to certain internal dynamics between micelles and saturated surface.

Coated polystyrene film is sufficiently stable for the presented range of SDS concentrations and temperatures. It is stable for at least several hours, when exposed to 100mM NaCl solution. However, when we exposed the film to the 100mM NaCl solution in presence of SDS, the polystyrene layer became unstable for SDS concentrations higher than 1mM. We observed a gradual decrease in PS layer thickness and eventually the measured spectra were corrupted, indicating there was a heterogeneous coverage of the waveguide. Thus, the

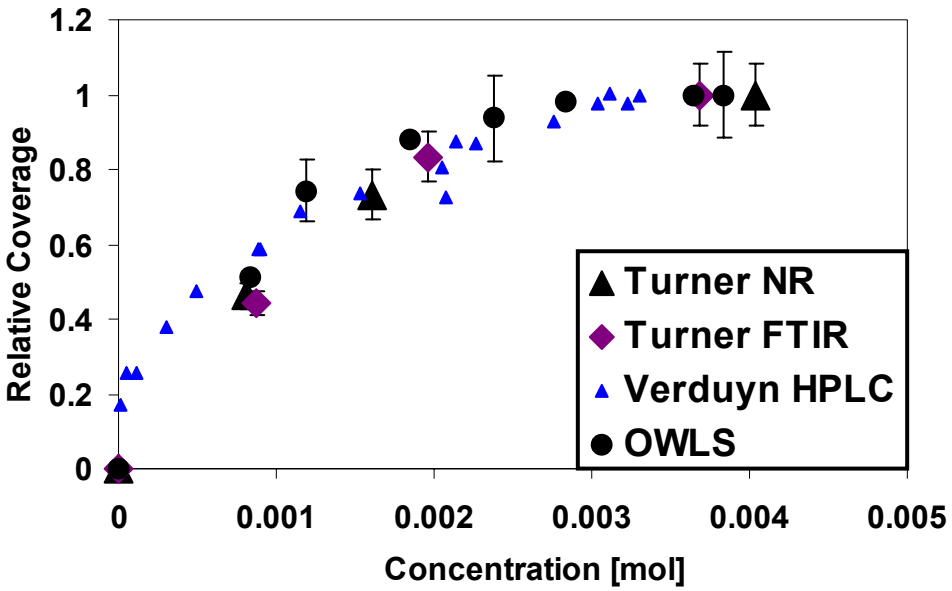

Figure 2-4. *Relative adsorption isotherms measured by different techniques. Relative coverage is plotted versus bulk SDS concentration.*

NR-Neutron Reflection, **FTIR** - Fourier Transform Infrared Spectroscopy, **HPLC** –High Pressure Liquid Chromatography, **OWLS** – Optical Waveguide Lightmode Spectroscopy

depletion of the polymer is acting opposite to the sensor response due to adsorption of surfactant molecules. Since both effects are comparable in the terms of sensor response and can not be decoupled from each other, data are not reported here.

Finally, the temperature effect of SDS deposition on polystyrene is presented in Figure 2-5. We measured isotherms for three different temperatures. Increase in temperature from 25°C to 45°C clearly reduced the amount of surfactant molecules adsorbed on the surface. Further increase of the temperature to 65°C shows the same trend, however decrease is not so significant compared to the previous one. The temperature 65°C appears to be upper boundary for polystyrene film stability in aqueous media. Above this temperature, dewetting of the polystyrene film was observed.

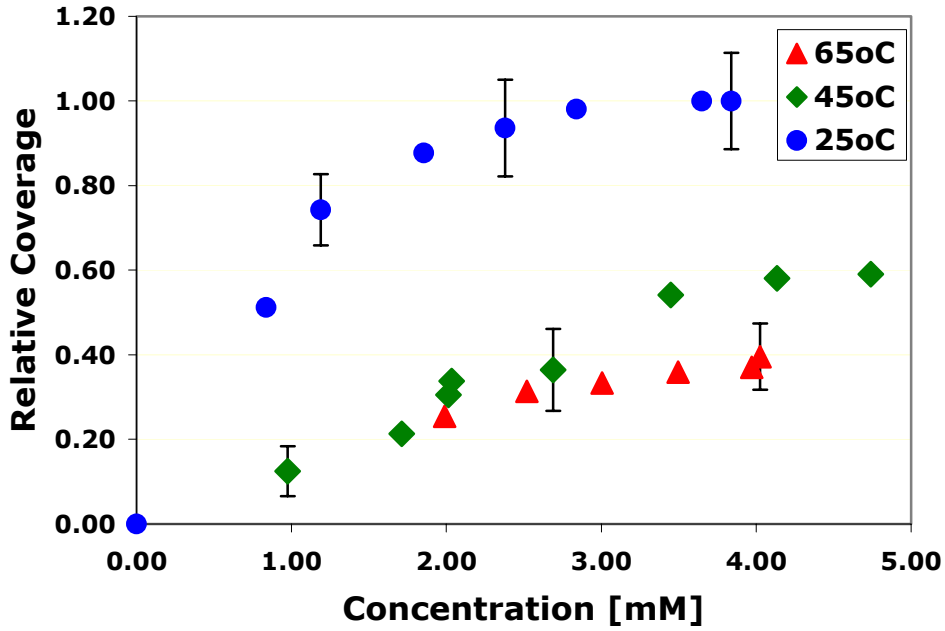

Figure 2-5. *Influence of the temperature on adsorbed amount of SDS measured by OWLS. Relative coverage is plotted versus bulk SDS concentration.*

2.5 Conclusions

Optical Waveguide Lightmode Spectroscopy was used to measure relative adsorption isotherm for SDS on polystyrene. Comparison between four different methods for SDS adsorption on polystyrene was made. From comparison we verify that OWLS describes relative adsorbed amount in agreement with other methods. The temperature was found to significantly reduce the adsorbed amount of SDS, as expected. The adsorption of SDS in a presence of salt shows significant shift of isotherm plateau towards lower concentration, however resulting in the film instability.

3 Optical Response of Porous Titania-Silica Waveguides to Surface Charging in Electrolyte Filled Pores

Abstract

In this work we present a novel method for in situ investigation of surface charging and ion transport inside nanopores of titania-silica waveguide by means of the waveguide optical response. Porous oxide waveguides show a strong optical response when exposed to electrolyte solutions and this response is consistent with oxide surface charging due to changes in ionic strength and pH of the solution in contact with the waveguide. The optical response to pH or electrolyte concentration change is stabilized within several minutes when the solution ionic strength is sufficiently high (0.1 M), while it takes two orders of magnitude longer to reach stable optical response at very low ionic strengths (< 0.1 mM). The relaxation times at the high ionic strength are still several orders of magnitude slower than expected from bulk diffusion coefficients of electrolytes in water. Our results indicate that diffusion of electrolytes is severely hindered (and more so with decreasing ionic strength) in charged pores inside waveguides.

3.1 Introduction

Sol-gel based silica-titania mixed oxides are important materials in catalysis [112, 113] and optical applications [114-116]. Sol-gel synthesis typically involves one or more metal alkoxides undergoing hydrolysis in aqueous solutions and subsequent condensation eventually forming particles or gels [117]. Resulting materials are usually nanoporous with substantial internal surface areas on the order of 100 $m^2.cm^{-3}$ and even higher when pore filling surfactants or molecular templates are used. Water can be removed from wet gels by supercritical drying to produce low density aerogels or at ambient pressure with various heating protocols. Ambient pressure drying causes further condensation and collapse of nanopores due to capillary pressure, resulting in densification and internal surface loss. Heat treatment promotes phase changes such as nucleation and growth of crystalline phases and phase separation, also leading to densification and decreased porosity. Microstructure of mixed oxides is thus influenced in early stages when small metal oxide oligomers have a

chance for heterocondensation to achieve molecular scale homogeneity in the wet gel, as well as in later stages when porosity and homogeneity can be severely modified during drying.

Planar optical waveguides can be prepared by coating silica-titania sols on appropriate substrates to obtain wet gel films, into which diffraction gratings are embossed and followed by further heat treatment in order to achieve required film hardness and stability [118, 119]. The final waveguide thickness is on the order of few hundred nanometers. Depending on temperature and duration of drying the film porosity can be as high as 20%. For standard drying procedures (few hours at 500 °C) typical porosity was found to be around 15% [120]. Using temperatures as high as 900 °C the porosity of silica-titania films can be reduced below 1% [121].

In Optical Waveguide Lightmode Spectroscopy (OWLS) the effective refractive index of the waveguide for both electric and magnetic modes is measured [63]. The laser light propagates along the waveguide by total internal reflection accompanied by an evanescent wave outside the waveguide surface, so that the optical properties of both the waveguide film and the surrounding environment determine the waveguide effective refractive index. Therefore OWLS is suitable for monitoring of processes leading to changes in the optical density inside and within about 100 nm of the surface of the optical waveguide. OWLS has been used extensively to study kinetics and equilibria of protein adsorption and structure of adsorbed layers [73, 79, 122, 123].

While compact waveguides with negligible porosity were prepared and showed almost negligible response to electrolyte solutions, standard porous waveguides exhibit strong optical response when exposed to electrolyte solutions [70]. This was interpreted as being due to ion adsorption on the internal surface of porous waveguides. In order to clarify the origin of this optical response, we conducted a series of experiments exposing porous waveguides to NaCl and NaOH solutions and estimated the resulting changes in polarization densities. Our measurements indicated that the main contribution to the waveguide optical response to electrolyte solutions comes from negatively charged sites at aqueous oxide interface inside electrolyte filled pores of the waveguide.

3.2 Theoretical Background

OWLS is based on monitoring the resonance spectra of linearly polarized light, coupled by diffraction grating into the waveguide. Positions of resonance peaks are measured for transverse magnetic and transverse electric modes. When small polarized molecules are adsorbed on a waveguide surface, reflection of polarized laser beam from the interface is changed, resulting in the shift of a resonance peak.

Details about the technique, as well as physical principles and model used to calculate the signal can be found in the background section 1.4.1.1. We use an optical model proposed recently by Mann [99], in order to determine the adsorbed amount of surfactant. The model is based on the concept of optical invariants, which describe the adsorbed layer in analogy with Gibbs interface, as a difference between response of the Fresnel optical interface and the true optical response in terms of the surface excess polarization densities γ [108] Eq. (1.13).

When effective refractive indices N_{TE} or N_{TM} are measured and refractive indices n_S and n_C of media surrounding the waveguide film are known, one can calculate the refractive index of the waveguide film n_F and its thickness t_F. Dependence of n_C on electrolyte concentration is available for common electrolytes [124].

Refractive index of the waveguide film can be changed due to adsorbed ions or charged groups at aqueous solid interface in the pores. The relation between the refractive index n of a multicomponent system and the effective electronic polarizabilities of its components is given by the Lorenz-Lorentz equation [7]:

$$\frac{4\pi}{3}\sum_{i=1}^{n}\alpha_i c_i = \frac{n^2-1}{n^2+2} \qquad (3.1)$$

where α_i and c_i denote the electronic polarizability (in units of m^3) and the number concentration (in units of m^{-3}) of the component i.

The electronic polarizability indicates how easy the molecular electron cloud is deformed by an applied electrostatic field. Ions in aqueous solutions have different electronic polarizability from those in the gas phase or in an ionic crystal. Water molecules in the ionic hydration shell have more stable spatial orientation compared to the bulk, due to strong electrostatic charge – dipole interaction, and they screen the electronic polarizability of ions. The polarizabilities of hydrated ions can be found in terms of the effective electronic polarizabilities [125]. Experimental observations showed that the electronic polarizability of cations is about one order of magnitude smaller than the electronic polarizability of anions for similar atom sizes.

This is because the cloud of electrons surrounding a cation is smaller and therefore less deformable by an applied external electric field. For the same reason, bigger cations have higher polarizability than the smaller ones with the same charge.

3.3 Experimental

Experiments were performed using the OWLS 110 instrument and OW 2400c waveguides supplied by Micro Vacuum Ltd., Budapest, Hungary. Waveguides deposited on a glass substrate were films approximately 175 nm thick, made of mixed oxide titania-silica (Ti/Si=3) and coated with a thin layer (10 nm) of SiO_2. Parameters of the waveguides provided by the manufacturer were: refractive index of the glass substrate 1.5258, grating period Λ = 416.7 nm, wavelength of laser light λ = 632.8 nm.

Waveguide treatment procedure was as follows: The waveguide was exposed to the HCl solution at pH = 2.5. Then it was exposed to deionized doubly distilled water in order to stabilize the optical signal. When the optical response was constant over several hours, the surface was taken to be in the reference state. A set of experiments was then performed by bringing the waveguide into contact with a series of electrolyte solutions of increasing ionic strength and/or pH. Each solution was flowed through a cuvette attached to the waveguide surface and the optical signal was recorded until a steady state was achieved, and then the next solution was introduced. After each set of experiments the waveguide was treated with the HCl solution until the same response was obtained as before the experiment and then the surface was left exposed to pure water for the next experiment.

Experiments were carried out at 298 K under nitrogen atmosphere. The ionic strength of aqueous solutions was varied by adding sodium chloride or sodium hydroxide. Sodium hydroxide solutions were stored in plastic bottles under nitrogen atmosphere in order to avoid the adsorption of CO_2 from the ambient air. A peristaltic pump was used to push solutions through the cuvette attached to the waveguide surface. The flow through the cuvette was in the laminar regime with the flow rate 1 ml/min. pH was monitored by Sure–Flow ROSS combination pH electrode by ORION, type 8172BN. The electrode was calibrated before each experiment. Refractive index of bulk solutions at room temperature was measured by the differential refractometer MERCK-La Chrome RI detector, type L-7490.

Two sets of experiments are reported here. The first set of experiments was performed with a series of NaCl concentrations between 10^{-6} and 10^{-1} M without pH adjustment (measured pH

values were between 6.3 and 7.0). The second set of experiments was conducted with a series of solutions with pH values between 6 and 10 at a constant ionic strength due to 0.1 M NaCl.

3.4 Results and Discussion

Porous waveguides exposed to pure water were equilibrated for about one day in order to eliminate observable downward drift of their refractive index, which is likely due to washing and possibly minor hydrolysis and dissolution of oxides constituting the waveguide. When a waveguide equilibrated with pure water was exposed to electrolyte solutions, the observed refractive index increased and gradually reached a steady value. Characteristic time for reaching steady state optical response varied from about 100 minutes at lowest ionic strengths ($< 10^{-4}$ M) to 1-2 minutes at 0.1 M NaCl. In Figure 3-1 we show the measured steady state refractive index increment as a function of NaCl concentration in liquid phase in contact with the waveguide. These results for the silica coated waveguide are in a very good agreement with data obtained for uncoated waveguides [70]. However, characteristic times for reaching steady state optical response in uncoated waveguides were about 10 minutes, i.e. one order of magnitude faster than for silica coated waveguides used in this study.

Next we compare measured waveguide refractive index increments to those corresponding to the bulk NaCl solution filling the waveguide pores. With typical values of the waveguide porosity $\phi = 0.15$ [79], the refractive index of waveguide equilibrated with pure water $n_F = 1.77$, and [NaCl] = 1 mM ($\Delta n_C = 1.0 \times 10^{-6}$ compared to pure water) we get the refractive index increment $\Delta n_F = \phi \Delta n_C = 1.5 \times 10^{-7}$, assuming that the bulk NaCl solution replaced pure water in the whole pore volume of the waveguide. The calculated refractive index increment is more than three orders of magnitude smaller than the measured value of the refractive index increment 4×10^{-4} for 1 mM NaCl (Figure 3-1) and below the resolution of the current instrument. Therefore the observed increase in the refractive index cannot be explained by NaCl uptake in waveguide pores alone. Thus we postulate that the observed optical response is due to changes induced by the electrolyte solution at the internal aqueous oxide interface in waveguide pores.

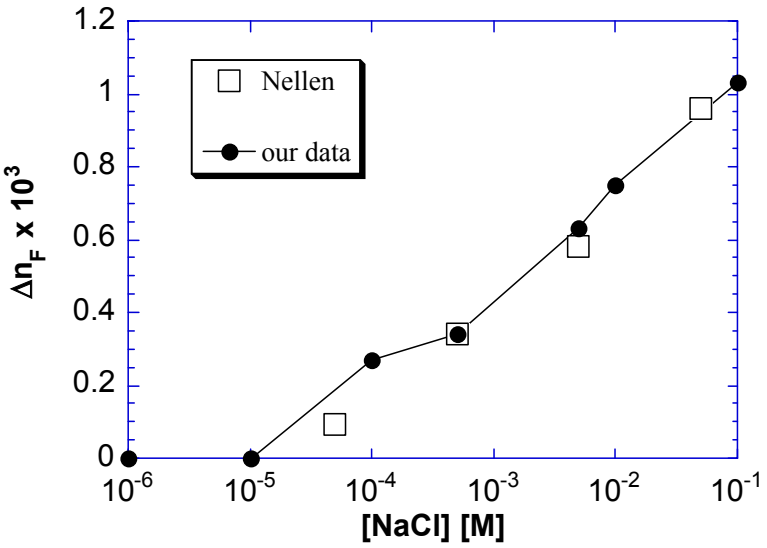

Figure 3-1. *Measured increment in film refractive index vs. NaCl concentration at neutral pH.*

It is well known that proton dissociation equilibria at aqueous oxide surfaces are shifted towards dissociation with increasing solution ionic strength. At pH (6.3-7.0) values in the first set of experiments both silica and titania are negatively charged, and their surface charge increases with concentration of an indifferent electrolyte, such as NaCl [126]. For example, the measured values of surface charge on both silica and titania for 0.1 M NaCl and pH = 7 were found to be around 5 x 10^{-2} C/m^2 [37]. Note, however, that the isoelectric point of silica is 2-3, while the isoelectric point of titania is 6.0. Now let us use the Lorenz-Lorentz Eq. (3.1) to estimate the refractive index increment due to negative charged oxygen sites at internal surface of the porous waveguide. Let us take a typical value for the effective (hydrated) polarizability difference between the oxo-anion and the neutral molecule, e.g. $\Delta\alpha_i = \alpha_{H2O} - \alpha_{OH^-} = 0.9 \times 10^{-30}$ m^3, the internal surface area of the waveguide film to be 25 times larger than the outer film surface (corresponding to the film thickness 175 nm and a reasonable internal surface area 1.5 x 10^8 m^2/m^3) and the surface charge density 5 x 10^{-2} C/m^2 (i.e. 5 x 10^{-7} mol/m^2 assuming charge -1 per anion). Then the anion concentration in the waveguide is c_i = 2 x 10^{25} /m^3 and from Eq. (3.1) we get the polarization density increment $(4\pi/3)c_i \Delta\alpha_i$ = 2 x 10^{-4}, which is of the same order of magnitude as the measured optical response $\Delta((n_F^2-1)/(n_F^2+2))$ = 6 x 10^{-4} for 0.1 M NaCl and pH = 7. It is therefore quite reasonable to suggest

that the waveguide optical response comes from negatively charged internal pore surface of the waveguide.

When the waveguide equilibrated with NaCl solution is exposed to pure water again, only a partial recovery of the refractive index is observed within few minutes, followed by a very slow further decrease. Thus the complete removal of NaCl from the waveguide is much slower than its entry at near neutral pH of pure water. The observed behavior of NaCl uptake in waveguide pores indicates that most of NaCl that diffused in is essentially immobilized at pH > 6. Although both titania and silica are negatively charged at pH > 6, and more so with increasing ionic strength, specific sodium binding is negligible at this pH for silica [127] and titania [128] as well. However, the diffusive mobility of ions in nanopores can be hindered due to surface charge at pore walls.

In order to achieve a complete removal of NaCl from the waveguide we used the acid treatment with HCl at pH = 2.5. During the acid treatment the waveguide refractive index decreased rapidly to values equal or lower than those measured at the previous equilibration with pure water. This indicates that NaCl was removed from the waveguide pores, its transport being likely facilitated by neutralization of negative surface charge on pore walls. After the HCl treatment the waveguides were exposed to pure water and there was no significant difference in the optical response between HCl solutions of pH 2.5 and pure water, even though both media differ slightly in the refractive index. This means that there is a negligible change of the polarization density of the waveguide exposed to pure water compared to that exposed to HCl solution at pH = 2.5.

In the second set of experiments at the higher ionic strength (0.1 M NaCl) and a range of pH values up to 10, we found a stronger optical response than at low ionic strength and pH, consistent with charging behavior of the aqueous oxide interface. Two important differences were observed compared to experiments at lower ionic strengths. Characteristic time of achieving a steady state optical response was shorter (about 1-2 minutes), and the optical response was nearly reversible on the same timescale. Similar qualitative observations were previously made on plain titania-silica waveguides exposed to a phosphate buffer [70], although in their case a substantial variation in the film refractive index was also observed when pH was changed between 3 and 6.

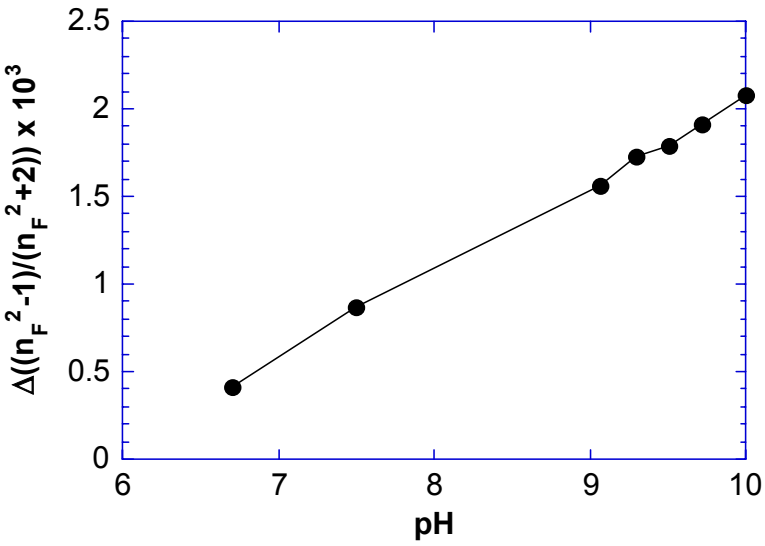

Figure 3-2. *Measured increment in polarization density vs. pH for 0.1 M NaCl solutions.*

Both of these observations can be explained by considering the screening effect of the background electrolyte on the electrical double layer at charged pore walls, which would reduce electrostatic repulsion between pore walls and diffusing ions, increasing their mobility. Since measurements of surface charging for both titania and silica surfaces as a function of pH in 0.1 M NaCl solutions are available, we can compare these data to the observed optical response under the same conditions, as measured in the second set of experiments.

In Figure 3-2 we plot the polarization density increment calculated from the measured film refractive index as a function of solution pH. From the analysis above, we expect that this quantity is proportional to the surface charge density within the porous waveguide, composed of mixed amorphous silica and microcrystalline anatase titania [129]. In Figure 3-3 we show a collection of experimental data on surface charges on titania (anatase) and silica (amorphous) [37]. We see that the observed optical response trend is more similar to that observed for titania (Figure 3-3a) than that for silica (Figure 3-3b).

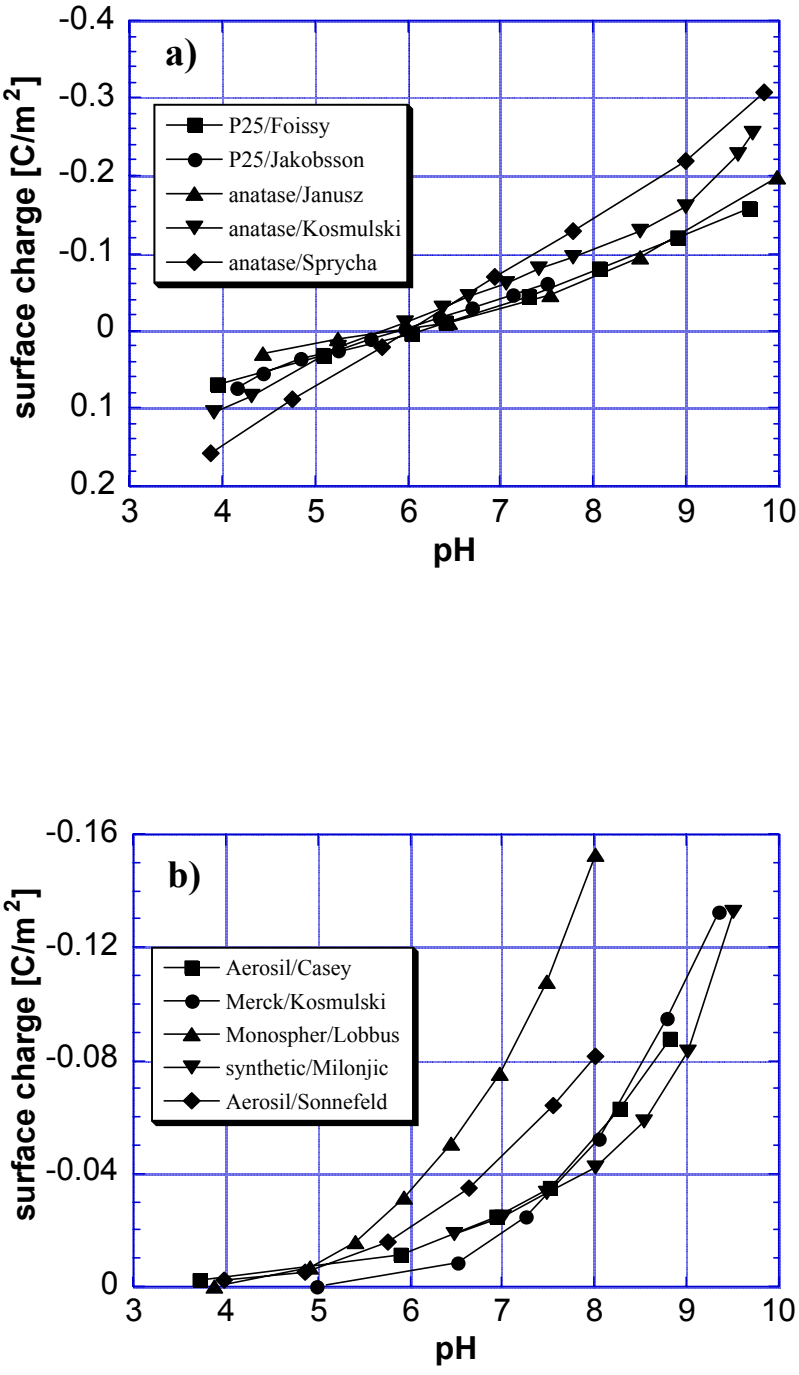

Figure 3-3. *Literature data on oxide surface charge vs. pH for 0.1 M NaCl solutions. a) titania (anatase), b) silica (amorphous).*

Finally we estimate the effective diffusion coefficient for NaOH inside the porous waveguide, using the observed characteristic time 1 minute and the characteristic length 175 nm equal to the waveguide thickness, we obtain D_{eff} = length^2/time = 5 x 10^{-12} cm^2/s. This value is about five orders of magnitude smaller than the expected effective diffusion coefficient based on infinity dilution diffusivity of NaOH in water (D = 1 x 10^{-6} cm^2/s) and accounting for pore volume fraction and tortuosity. Thus even at the ionic strength 0.1 M the diffusion of small electrolytes inside the waveguide pores is severely hindered, with diffusivities about 10^5 times smaller than those in water.

3.5 Conclusions

We used Optical Waveguide Lightmode Spectroscopy to study optical response of porous titania-silica waveguides exposed to electrolyte solutions. The observed optical response is consistent with aqueous oxide surface charging and can be due to either the polarizability of the negatively charged surface sites or the polarizability of counterions in the electrical double layer. However, the calculated contribution to the polarization density from the sodium salt present in waveguide pores was found to be several orders of magnitude smaller that the measured quantities. Therefore the influence of sodium cations is not a dominant factor determining the value of the measured optical response signals. We conclude that the main contribution to the polarization density comes from highly polarizable negatively charged oxygens, corresponding to the charge density at the internal surface of porous waveguides.

4 Effect of temperature, pH and salt concentration on β-lactoglobulin deposition kinetics studied by OWLS

Abstract

Deposition kinetics of β-lactoglobulin at a solid-liquid interface was studied with optical waveguide lightmode spectroscopy (OWLS) over a range of temperatures between 61°C and 83°C. A new temperature-controlled cell for OWLS was used for the deposition measurements. This technique allows fast, on-line monitoring of the deposit formation over a wide range of temperatures. Primary protein layers were deposited at 25°C in order to precondition and stabilize the waveguide surface. Sustained deposition rates at elevated temperatures lasting from few minutes (around 80°C) to hours (below 70°C) resulted in multilayer deposits up to several tens of nanometers thick. The measured deposition rates were strongly influenced by temperature as well as by pH and NaCl concentration. Deposition rates were decreasing with increasing pH from 5.5. to 7.4, in a trend similar to that for non-covalent aggregation of β-lactoglobulin in the bulk solution. Activation energies for deposition rates were decreasing with increasing pH, from 340kJ/mol at pH=5.5 to 230kJ/mol at pH=7.4, and were similar to the activation energies for denaturation of β-lactoglobulin in the bulk solution.

4.1 Introduction

β-lactoglobulin (β-LG) plays a crucial role during heat treatment of milk. It is the main protein in whey, comprising about 50% of the total whey proteins in bovine milk. At room temperature and at pH between 5.2 (the isoelectric point) and 7 it is well soluble in water, where it exists mainly as a dimer stabilized by hydrogen bonds [29]. At these conditions β-LG spontaneously adsorbs on most surfaces from aqueous solutions, resulting in an irreversibly bound single layer film. Further deposition on primary β-LG layers is very slow unless heat treatment is applied. At temperatures typical for milk processing (such as pasteurization) between 60°C and 90°C, voluminous deposits are rapidly formed at solid surfaces, leading to serious fouling problems. It is well known that fouling phenomena at this range of temperatures is related to thermal denaturation of β-LG [35].

During thermal exposure at pH above the isoelectric point, the unfolding of native globular structure exposes the hydrophobic region of β-LG, containing disulphide bonds as well as one free thiol group [130]. Moreover, at pH between 7 and 9 there is a gradual conformational change so that at pH=9 the thiol groups are exposed even at the ambient temperature [131, 132]. As a consequence of this reversible unfolding, the chemical reaction of the thiol group with disulphide bonds results in protein aggregation and thus irreversible denaturation. In addition to the covalent bridging via disulphide bonds, there is also physical (non-covalent) aggregation due to exposure of the hydrophobic residues, resulting in a complex aggregation mechanism influenced by temperature, pH, salt concentration, surfactant presence and protein concentration [29, 30, 131, 133-137].

Denaturation and aggregation of β-LG can thus be described in two successive, yet interlinked steps. The first step is a reversible transformation between the protein native state and the unfolded state, where unfolding follows a simple first order kinetics. Upon unfolding the inert hydrophobic part and the thiol group are exposed and become reactive, which allows for irreversible denaturation of the unfolded protein to proceed. The second step is then aggregation of unfolded proteins through covalent (irreversible reaction of thiol groups) and non-covalent mechanisms resulting in protein denaturation. Kinetics of denaturation is usually experimentally determined by monitoring time evolution of the fraction of protein remaining

in its native state. Depletion of the native protein concentration in time is customarily described in literature [30, 136, 138, 139] using the n-th order kinetic expression

$$\frac{dN}{dt} = -k_{den} N^n \qquad (4.1)$$

where N is the concentration of native protein and k_{den} is the corresponding denaturation rate constant. Depending on the experimental conditions, the apparent reaction order n obtained by fitting experimental data was found to vary between 1 and 2. Since the overall process involves the first order unfolding followed by multiple reaction and aggregation steps, it is not surprising that a complex dependence of denaturation kinetics on temperature, pH and protein concentration is observed.

Denaturation temperature of β-LG (i.e., the temperature where unfolding and subsequent depletion of the native form becomes observable) decreases from about 75°C at pH~5 to 60°C at pH~5, 50°C at pH=8 and 25°C at pH=9 [29]. Measured denaturation rates increase with increasing pH between 5 and 8, while the activation energy corresponding to the denaturation rate constant in Eq. (4.1) decreases with increasing pH [140]. It was found that denaturation rates of β-LG are closely related to the availability and reactivity of the free thiol groups, which increases with pH [141], so that denaturation kinetics is primarily driven by covalent bonding of unfolded proteins. On the other hand, formation of large β-LG aggregates as monitored by light scattering was found to be primarily driven by non-covalent physical aggregation. Kinetics of physical aggregation of β-LG becomes slower with increasing pH between 5 and 8, due to increasing negative charge of the protein as pH is moving away from its isoelectric point [141, 142].

Although there have been numerous studies on thermal stability, aggregation and fouling in β-LG solutions, there has been only few experimental studies addressing kinetics of early stages of β-LG deposition at solid surfaces at elevated temperatures. It was noted early on that the macroscopic fouling by β-LG becomes faster as pH is decreased from 7 to 5, in opposite to the trend observed for β-LG denaturation, and it was suggested that the deposition kinetics of β-LG essentially follows its aggregation kinetics in the bulk [143]. Ellipsometry and reflectometry was used to study early stages of deposition kinetics of β-LG on chromium oxide, stainless steel and modified stainless steel surfaces. Elofsson et al. [144] studied deposition of rather concentrated solution of β-LG (48g/L) in phosphate buffer with 0.1 M NaCl at pH=6.9 and temperatures 65-68°C at chromium oxide. Jeurnink et al. [35] used

reflectometry to study effects of preheating on deposition of whey protein isolates and β-LG at various concentrations in water at pH=7.1 at temperatures 70-95°C on chromium oxide surfaces. Santos et al. [36] used ellipsometry to study deposition of whey protein isolates at various concentrations in water at pH=6.7 and 7.8 at temperatures 85°C. Variously modified stainless steel surfaces were used, including one with a sol-gel based silica surface. They found that while most surface modifications did not change the deposition rate very much compared to the original stainless steel, some modifications resulted in about twofold reduction in the long term deposition rate, while the silica surface showed an about twofold increase. This also confirms that there is only a limited effect of the original surface properties on long term fouling rates after a multilayer deposit is formed on the solid surface.

In this work we present measurements of heat induced deposition rates of β-LG using optical waveguide lightmode spectroscopy (OWLS). OWLS belongs to a class of optical reflection techniques including also ellipsometry and reflectometry. It is an established technique to follow in-situ adsorption and deposition at solid-liquid interfaces, especially for proteins at ambient temperature. We use OWLS to determine the kinetics of β-LG deposition at the silica-titania waveguide surface over a broad range of temperatures and pH values.

4.2 Experimental Section

β-LG from bovine milk used in this study was from Fluka (β-Lactoglobulin A and B, purity ~80%, Lot # 1087564). Protein solutions were prepared by proper addition of β-LG into 10mM HEPES buffer from Acros Organics (Lot # A019289801). Buffers were adjusted to target pH and salt concentration by NaOH and NaCl addition, respectively. Protein solutions were left to equilibrate for at least two hours before being used or stored at 4°C for a maximum of three days. Ultra pure water (Millipore, 18mΩ) was used for solution preparation. All solutions were degassed under vacuum before use in order to reduce creation of bubbles in the OWLS cell.

Deposition experiments were performed using the instrument OWLS 110 made by Microvacuum Ltd, Budapest, Hungary, with the integrated temperature control unit OWLS TC. The OWLS waveguides (75% SiO_2, 25% TiO_2) were supplied by Microvacuum. The waveguide layer of thickness $t_f \approx 180nm$ and refractive index $n_f \approx 1.76$ (at 25°C) is supported by

glass substrate of refractive index $n_s=1.52578$ with dimensions $12\times8\times0.5mm$. The waveguides were stored in a NaOH solution at pH=11 for 3 hours to uniformly activate hydroxyl groups on the surface prior to protein deposition. They were subsequently rinsed with water and dried with nitrogen. The waveguide was placed adjacent to the flow-through cell in the shape of a rectangular channel (8mm long, 0.8mm high, 2mm wide) with the total volume of 12.8µl, with entrance and exit ports. All delivery tubes and the measuring cell were made of Teflon®.

Details about the technique, as well as physical principles and model used to calculate the signal can be found in the background section 1.4.1.1. We use an optical model proposed recently by Mann [99], in order to determine the adsorbed amount of surfactant. The model is based on the concept of optical invariants, which describe the adsorbed layer in analogy with Gibbs interface, as a difference between response of the Fresnel optical interface and the true optical response in terms of the surface excess polarization densities γ [108] Eq. (1.13).

Prior to the β-LG deposition, a buffer solution was flowed through the deposition cell and the waveguide parameters were determined. The flow rate was held constant at $2ml.hr^{-1}$ (corresponding to a residence time of about 30s in the deposition cell) by the programmable syringe pump Vit-Fit (Lambda, Czech Republic). The syringe pump provided steady injection of the sample without flow rate pulses, which is particularly important for temperature measurements, because fluctuating flow rates induce oscillations of the fluid temperature, resulting in substantial noise in the experimental data. The response of the bare waveguide at elevated temperature was recorded prior to the deposition measurements.

4.3 Results and Discussion

4.3.1 Primary layer creation at ambient temperature

Primary exposure of oxide surfaces to protein solutions typically leads to spontaneous adsorption of thin protein layers. In this work, bare silica-titania waveguides were first equilibrated at 25°C with the blank buffer solution at the flow rate of $2ml.hr^{-1}$. Then the waveguide was exposed to a β-LG solution in 10mM HEPES, pH 5.5, at the standard flow rate for 60 minutes to create a primary protein layer. In Figure 4-1 we show the time evolution of the deposited mass of β-LG on the bare waveguide surface for two subsequent exposures to $0.5mg.ml^{-1}$ solution of β-LG followed by rinsing with the blank buffer.

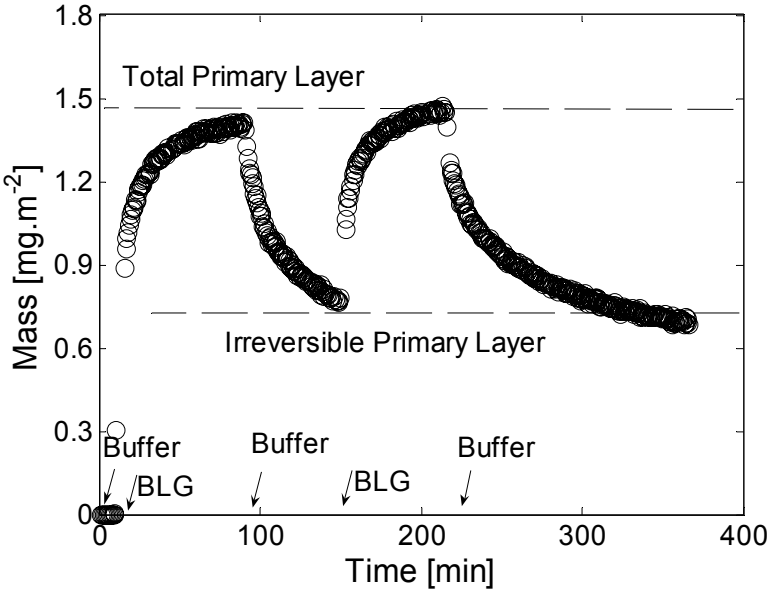

Figure 4-1. *Primary exposure of bare waveguide to 0.5 mg.ml^{-1} β-LG in 10mM HEPES, pH 5.5, at 25°C. Arrows above the time axis indicate change in liquid phase.*

The first exposure to the β-LG solution for 60 minutes resulted in the total primary layer coverage of 1.4mg.m^{-2}. After reaching this coverage a further growth of deposited mass becomes very slow. Subsequent desorption in the blank buffer for 60 minutes resulted in a decrease of the deposited mass to 0.7mg.m^{-2}. The subsequent exposure to the same β-LG solution for another 60 minutes resaturated the surface to the same total coverage as observed in the first exposure. Also, the second desorption resulted in the same deposited mass as in the first desorption. This mass of 0.7mg.m^{-2} corresponds to the irreversible primary layer, where the protein is irreversibly bound to the waveguide surface so that it cannot be removed from the surface by desorption in the blank buffer at 25°C.

The density of the primary layer depends on various factors like pH, salt concentration, protein concentration, and surface properties. We examined the effect of solution pH on the primary layer deposition from 10mg.ml^{-1} β-LG in 10mM HEPES for the range of pH 5.5-7.4. Experiments showed the same deposition pattern as discussed in Figure 4-1, i.e., alternating between the total primary layer coverage and the irreversible primary layer coverage, as for 0.5mg.ml^{-1} β-LG solution discussed above. The values of mass corresponding to the total primary layer coverage after one hour deposition at ambient temperature as well as to the

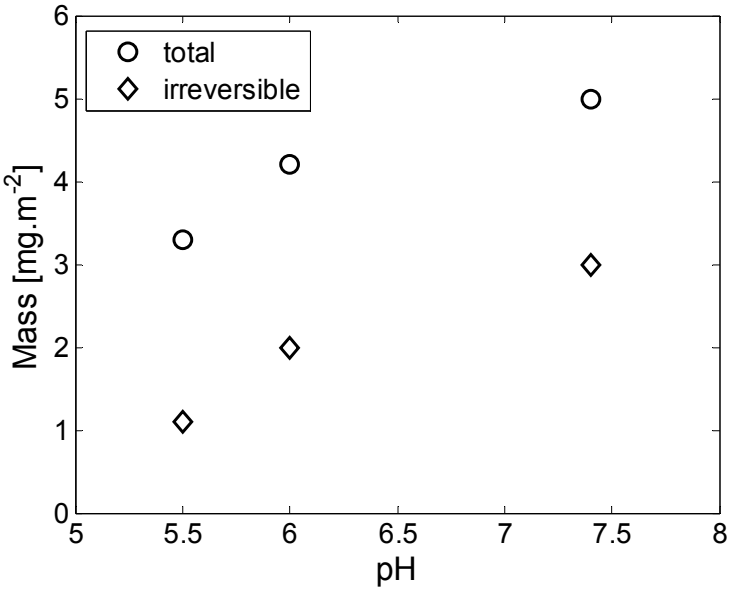

Figure 4-2. *Effect of pH on total deposited mass (circles) and irreversibly deposited mass (diamonds). 10 mg.ml^{-1} β-LG in 10mM HEPES at 25°C.*

irreversible primary layer coverage after one hour rinsing with the buffer are shown in Figure 4-2 as a function of pH.

The observed adsorption behavior of β-LG is consistent with the classical protein deposition mechanism [145, 146]. The adsorbed protein is present in two states: one irreversibly and the other reversibly adsorbed. Proteins slowly undergo conformational changes after being adsorbed on oxide surfaces and these changes result in a stronger interaction between protein and surface. Such strongly bounded proteins loose their native structure, spread in time over the surface thus hindering further protein irreversible deposition. Reversibly bound proteins are weakly attracted to the surface, which results in their accumulation at the interface, but they can be relatively easily removed by washing.

4.3.2 Deposition at elevated temperatures

4.3.2.1 The temperature response of the bare waveguide in pure buffer

Exposure of the bare waveguide to aqueous solutions at various temperatures leads to changes of the measured incoupling angle α and the corresponding effective refractive index N. This is due to the temperature dependence of the system optogeometric parameters: refractive indices of the substrate n_S and cover medium n_C, as well as the thickness t_F and refractive index n_F of

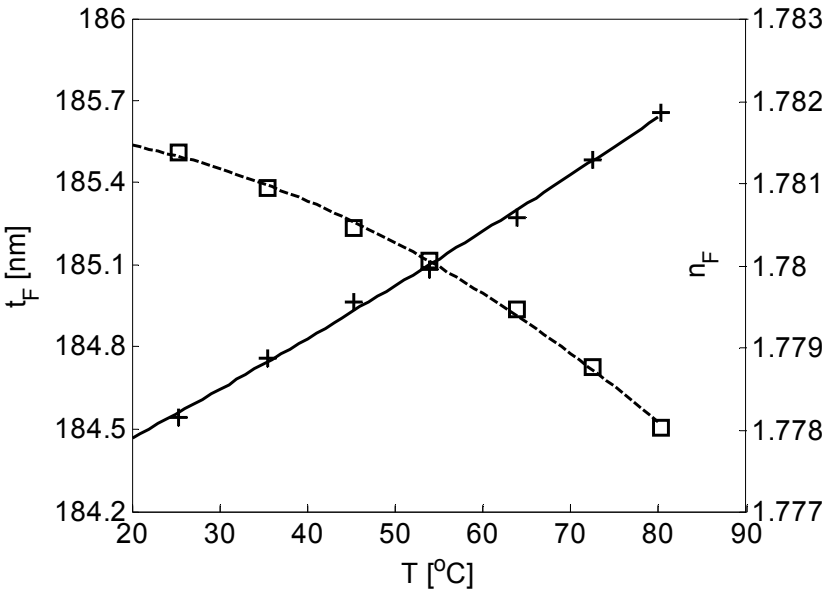

Figure 4-3. *Waveguide parameters measured in 10mM HEPES, pH 5.5 as a function of temperature. Crosses represent the measured thickness t_F and squares the refractive index n_F. Lines represent the fit given by Eq.* (4.2).

the waveguide itself. We can calculate the waveguide parameters t_F and n_F as a function of temperature from the Eq. (1.12) for TE and TM modes, using the measured values of *N(TE)* and *N(TM)* at the corresponding temperatures. The expressions used to describe the temperature dependence of n_S (glass substrate) and n_C (10mM HEPES solution at pH=7.4 and water) are reported in Table 4-1. It is worth noting that calculations of the deposited mass using the cover medium refractive index either for HEPES ($n_{C,HEPES}$), or for water ($n_{C,water}$), shown in Table 4-1, resulted in virtually identical results. This means that for the diluted aqueous solutions used here, the OWLS response, Eq. (1.13), is insensitive to changes of n_C due to the cover medium composition.

The temperature response of the bare waveguide was in the presence of the buffer solution (10mM HEPES, pH 5.5). Flow rate through the heated deposition cell was kept constant at 2ml.h^{-1}. The set of two nonlinear Eq. (1.12) for the TE and TM modes was solved to obtain the waveguide parameters t_F and n_F, using the values of n_C and n_S in Table 4-1.

Table 4-1. *Refractive indices as a function of temperature. T denotes temperature in °C.*

Parameter	25°C	T [°C]	Source
$n_{C,water}$	1.331144	$n_{C,H_2O}^{25^oC} - \frac{75453.41\Delta T + 2340.431\Delta T^2 + 6.363191\Delta T^3}{T.10^7 + 65.7081.10^7}$; $where \quad \Delta T = T - 25$	[147]
$n_{C,HEPES}$	1.333699	$1.33156 - 5.89189 \cdot 10^{-5} T - 1.06617 \cdot 10^{-6} T^2$	[148]
n_S	1.525718	$1.52542 - 1.23 \cdot 10^{-6} T$	[147]

The values of t_F and n_F measured at steady temperatures were fitted as a function of temperature T (in °C) using the following expressions and the corresponding results are shown in Figure 4-3:

$$t_F(T) = 184.31 + 0.0096872T - 9.5054 \cdot 10^{-6}T^2$$
$$n_F(T) = 1.7881 - 2.7434.10^{-5}T - 2.2582.10^{-7}T^2 \qquad (4.2)$$

A similar magnitude of the change in the waveguide thickness and refractive index with temperature was also measured in the presence of pure water, in agreement with previous results [147]. When the waveguide was cooled back to the ambient temperature, a change of about Δn_f=0.001 in the waveguide refractive index was observed. This observation was made for several waveguides exposed to the HEPES solution at pH between 5.5 and 7.4. In all cases the temperature response of the bare waveguide to the buffer solution revealed gradual modification of the waveguide optical properties at elevated temperatures. The same effect was also observed for silica and niobia coated waveguides. Coating of waveguide surfaces (i.e., by polymer or protein) can be used to effectively suppress this effect, by providing a barrier between the waveguide and the liquid solution. In particular, a primary protein layer adsorbed at ambient temperature can stabilize the waveguide at elevated temperatures, as will be discussed shortly.

4.3.2.2 The temperature stability of primary protein layers in pure buffer

Before discussing thermally driven deposition of β-LG, we address the issue of durability of irreversibly bound primary protein layers deposited at ambient temperature, when exposed to the buffer solution at elevated temperatures. A typical experiment is shown in Figure 4-4, starting with the protein layer deposited at 25°C from 10mg.ml^{-1} β-LG solution.

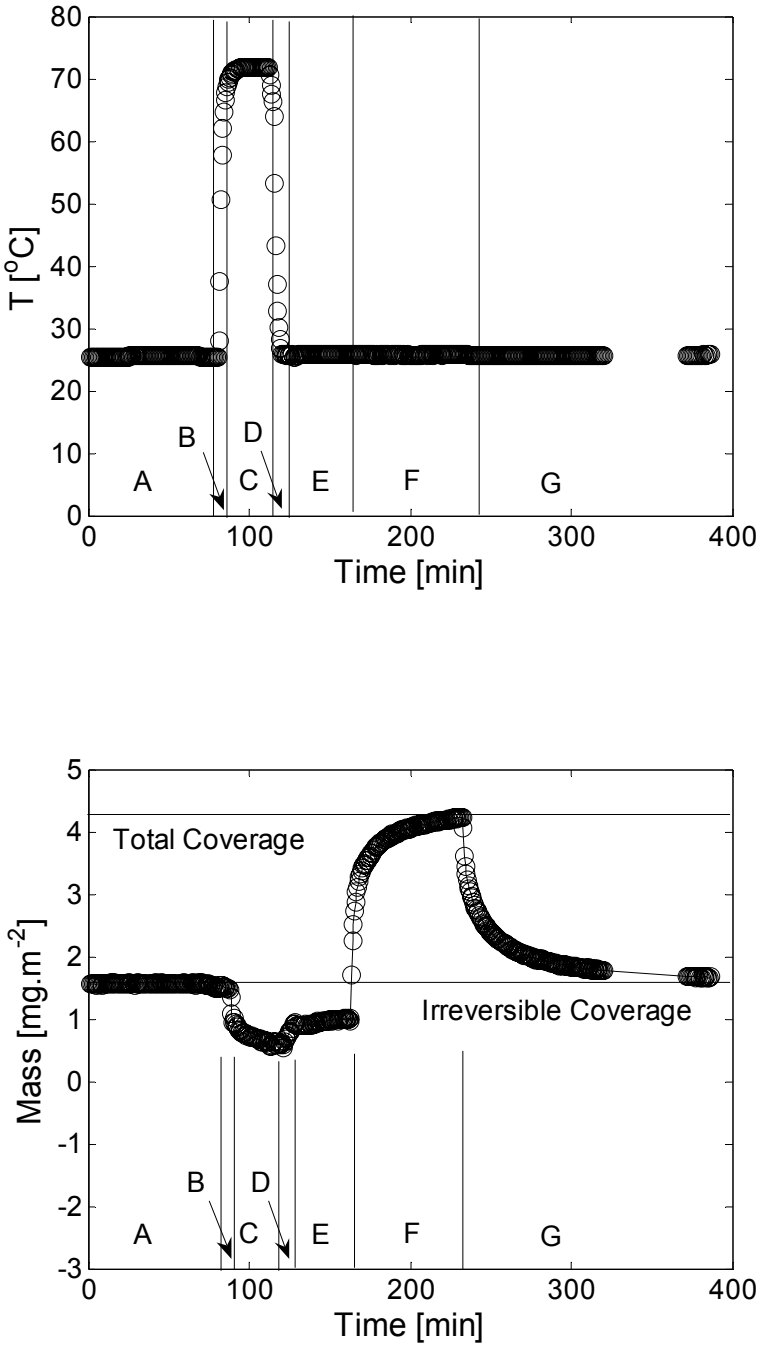

Figure 4-4. *Temperature exposure of the thin protein layer in 10mM HEPES solution, pH 5.5 at 72°C. The protein layer was resaturated in 10mg.ml^{-1} β-LG solution.*

Table 4-2. *Experimental procedure for temperature stability of primary protein layer at 72°C shown in* Figure 4-4.

Period	Time	Bulk Solution	Flow Rate	Temperature
	[min]		[ml.hr^{-1}]	[°C]
A	0-81	buffer	2	25
B	81-89	buffer	2	heating
C	89-112	buffer	2	72
D	112-129	buffer	2	cooling
E	129-163	buffer	2	25
F	163-230	β-LG in buffer	2	25
G	230-400	buffer	2	25

The detailed experimental conditions are summarized in Table 4-2. At ambient temperature the irreversibly deposited protein amount was 1.6mg.m^{-2} (period A). After 30 minutes of heat treatment at 72°C in 10mM HEPES solution at pH 5.5 (period C) and cooling back to the ambient temperature (period D), the measurement becomes steady at the end of period E. Here, the layer exhibits a partial loss of deposited mass being the protein coverage decreased to 1.0mg.m^{-2}. Subsequent resaturation of the protein layer by native β-LG solution for 60 minutes (period F) at ambient temperature resulted in the complete recovery of the total coverage (4.2mg.m^{-2}) reached in the saturation step at ambient temperature (not shown in Figure 4-4) preceding the heat treatment. Subsequent rinsing with the blank buffer (period G) resulted in the recovery of the same irreversible coverage (1.6mg.m^{-2}) as observed before the thermal treatment.

The same observation was made for repeated thermal exposures of the same deposited protein layer at six different temperatures between 60°C and 80°C. Irreversibly deposited amounts measured before temperature exposure (period A) and at the end of buffer washing (period G) were always very similar (difference ±20%). These experiments showed that the protein layer, which partially degrades during the thermal treatment, can be fully recovered by subsequent resaturation at ambient temperature. Moreover, it has been observed that the optical properties of the waveguide covered by the primary protein layer are stable in the buffer solution at the temperatures considered in this work. Since this was not the case for bare surfaces as mentioned above, it is apparent that the protein layer effectively protects the waveguide beneath it from heated buffer solutions.

4.3.2.3 Secondary deposition of β-LG on thin protein layers at elevated temperature

As discussed above, the first step in the β-LG deposition process is the formation of a primary layer, which occurs spontaneously even at ambient temperature. This primary layer is irreversibly bound to the original surface of the sensor, resulting in a significant modification of its surface properties. Further deposition at elevated temperature is then essentially driven by interactions between the deposited proteins and the proteins in the bulk. In order to decouple the interaction between surface-protein (initial deposition) and protein-protein (secondary deposition) we measured the secondary deposition rates always starting with protein layer several nanometers thick. In Figure 4-5 we show results from a typical secondary deposition experiment from 10mg.ml^{-1} β-LG solution at 75°C. The detailed experimental conditions are reported in Table 4-3. A previously deposited layer (13mg.m^{-2}) was present on the top of the waveguide (period A), so that the influence of the original waveguide surface on the deposition rate is expected to be negligible. After the system was heated to the desired temperature (periods B and C), the β-LG solution was injected. After a very short transition time (in this case about one minute) the rate of change of the deposited mass became constant and the deposition rate at the given temperature could be determined from the slope of the linear growth observed in period D.

It is worth noting that the deposited mass shown by the circles in Figure 4-5 was calculated using the temperature correction of the optical properties described above in section 4.3.2.1 using the temperature measured on-line by a thermocouple located close to the deposition cell. It can be seen that the apparent deposited mass with temperature correction exhibits a small peak soon after the temperature started to increase at the beginning of period B. By the time the system reached a steady temperature (period C), this transient effect disappeared. This is an artifact due to the fact that in the non-steady state regime the temperature measured by the thermocouple does not correspond to the real waveguide temperature. Therefore, the temperature correction used in period B of the experiment does not accurately represent the optical parameters of the system and incorrect values of the deposited mass are obtained.

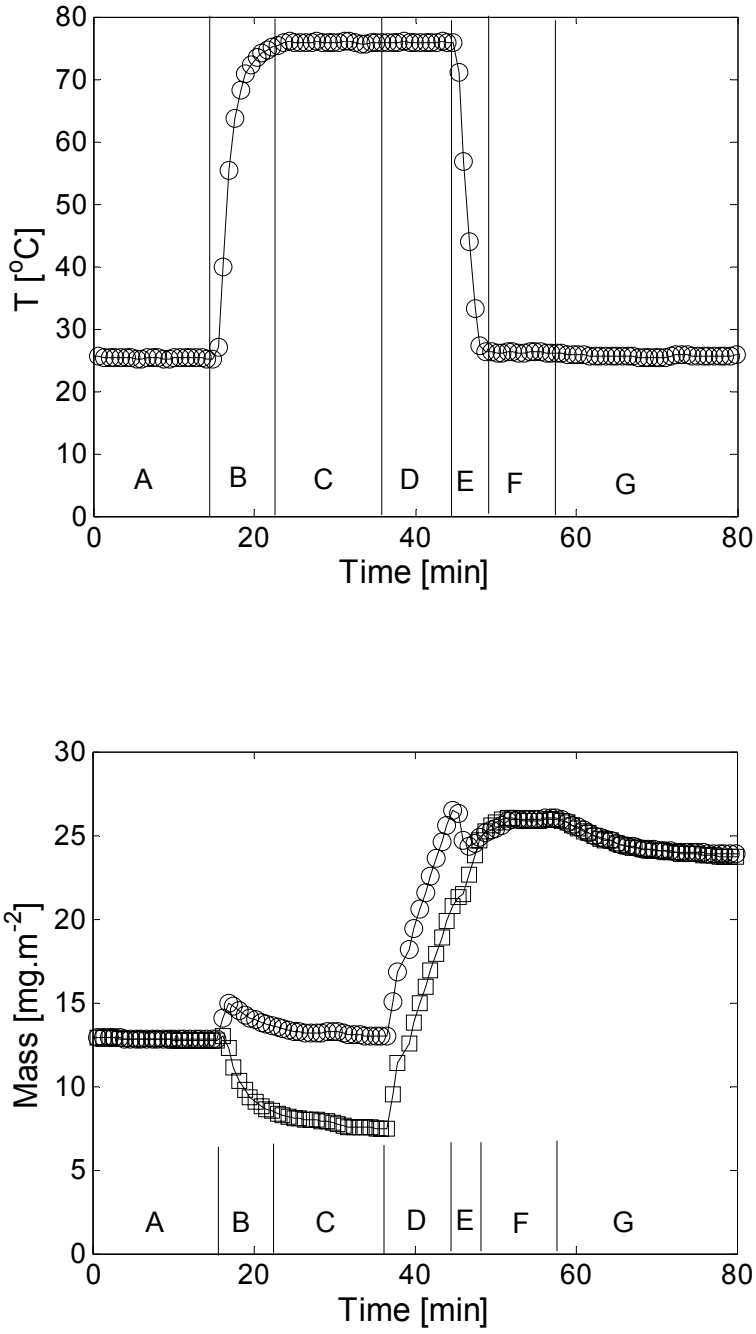

Figure 4-5. *Secondary deposition from a 10mg.ml^{-1} β-LG solution at, pH 5.5 and 75°C on previously deposited protein layer. Values computed with temperature correction for the optical properties (circles) and without correction (squares).*

Table 4-3. *Experimental procedure for secondary deposition experiment at 75°C shown in Figure 4-5.*

Period	Time	Bulk Solution	Flow Rate	Temperature
	[min]		[ml.hr^{-1}]	[°C]
A	0-15	buffer	2	25
B	15-22	buffer	2	heating
C	22-36	buffer	2	75
D	36-45	β-LG in buffer	2	75
E	45-48	buffer	0	cooling
F	48-57	buffer	0	25
G	57-80	buffer	2	25

For the sake of illustration, the squares in Figure 4-5 show the values of the deposited mass calculated without applying the temperature correction. In this case, the calculated apparent deposited mass is significantly lower than the actual one represented by the circles in the same figure. However, the deposition rates (corresponding to the slope in region D) determined from the data calculated with and without temperature correction are very similar.

It is worth noting, that an alternative simplified approach to the evaluation of the deposition rates can be used, based on treating the previously deposited layer of protein as part of the waveguide. In this case, apparent optogeometric parameters of the so modified waveguide (consisting of waveguide and thin protein layer) n_F and t_F are determined using Eq. (1.12) at the relevant deposition temperature just before the injection of β-LG. We have seen that this approach yields very similar deposition rates as the more rigorous one based on the temperature correction of the waveguide parameters.

The values of mass deposited during the secondary deposition from 10mg.ml^{-1} β-LG solution (10mM HEPES, pH 6.4) at various temperatures are shown in Figure 4-6 as a function of time. The deposition below 60°C was so slow that it was not detectable with our instrumentation. The linearity of the mass growth in time was confirmed by long experiments lasting up to two hours. Of course, such long experiments are only possible for conditions where the deposition rate is slow enough so as to avoid the saturation of the waveguide evanescence region, which occurs at mass coverage of about 35mg.m^{-2}.

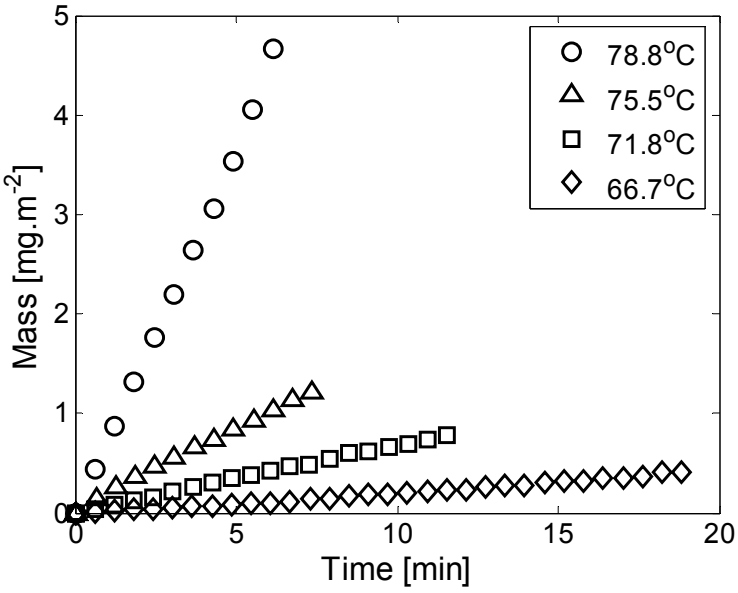

Figure 4-6. *Growth of protein mass during secondary deposition from a 10mg.ml^{-1} β-LG solution in 10mM HEPES at pH 6.4 and various temperatures.*

The deposition rates were found to increase exponentially with the temperature over the range of temperatures considered here. They were highest at pH 5.5 (close to the isoelectric point of β-LG) and decreased as pH was increased from 5.5 to 7.4. This pattern of dependence on pH is consistent with the trend observed for the growth of large aggregates in β-LG solutions [132, 149]. When pH is above the isoelectric point of β-LG, increasing pH results in increasing negative charge on β-LG, which implies increasing electrostatic repulsion and thus slowing down of aggregation as well as deposition kinetics.

It is worth noting that the residence time of the protein inside the deposition cell at elevated temperature is around 30 seconds. Based on previous experimental studies on β-LG aggregation [136] it is expected that growth of protein aggregates due to non-covalent (physical) aggregation is not significant for such short times, especially at higher pH (i.e., higher charge and thus stronger electrostatic repulsion) and lower temperatures (i.e., slower denaturation). On the other hand, at higher pH values and higher temperatures (where denaturation is faster), formation of small covalently bound clusters observed in bulk solutions [136] can not be excluded before proteins are transported to the surface.
In Figure 4-7 we show the Arrhenius plots for secondary deposition rates at various pH values. From these the activation energy E_a for the secondary deposition process can be

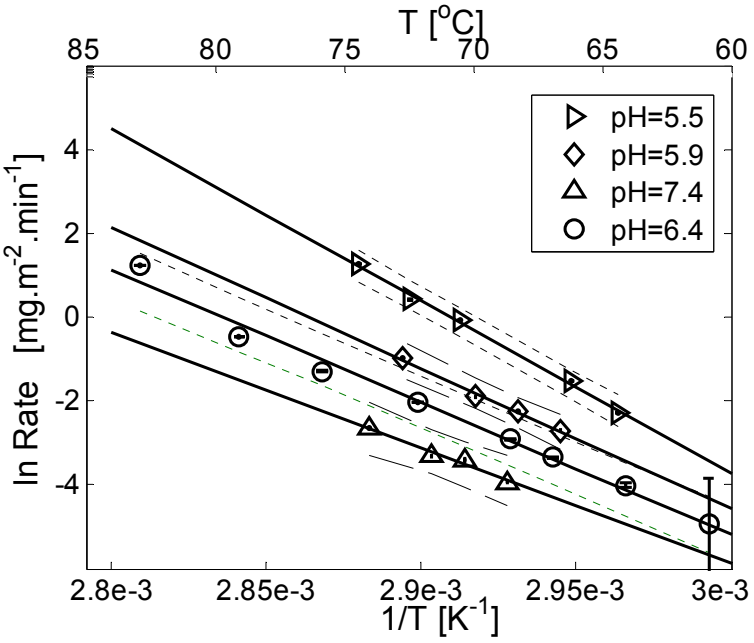

Figure 4-7. *Arrhenius plot for the deposition rate from a 10mg.ml^{-1} β-LG solution in 10mM HEPES. Points are the experimental values, the solid lines represent the linear fit and the doted lines are the upper and lower estimates corresponding to a 95% confidence level.*

estimated, and the obtained values are shown in Figure 4-8 as a function of pH. These activation energies for β-LG deposition are similar to those previously reported for β-LG denaturation at comparable pH values found in the literature [29, 132, 137, 140]. On the other hand, the denaturation kinetics itself becomes faster as pH increases [131, 132, 150, 151], which is opposite to the trend observed here for the deposition kinetics.

A possible explanation for the observed dependence of deposition rates and activation energies on pH is as follows. Let us consider that the deposition process consists of two steps in series. Unfolding and denaturation of β-LG (facilitated by covalent binding of unfolded proteins) with the denaturation kinetics according to Eq. (4.1) with rate constant k_{den}, is followed by deposition of denatured β-LG, with the first order kinetics and the deposition rate constant k_{dep}. Assuming that the conversion of the native protein is quite small within a short residence time in the deposition cell, so that the extent of both denaturation reaction and the subsequent deposition step stays small (i.e., only small proportion of protein denatures and only small proportion of denatured protein is deposited), it is easy to see that the overall rate of β-LG deposition R_{dep} would be proportional to the product of the two rate constants k_{den}

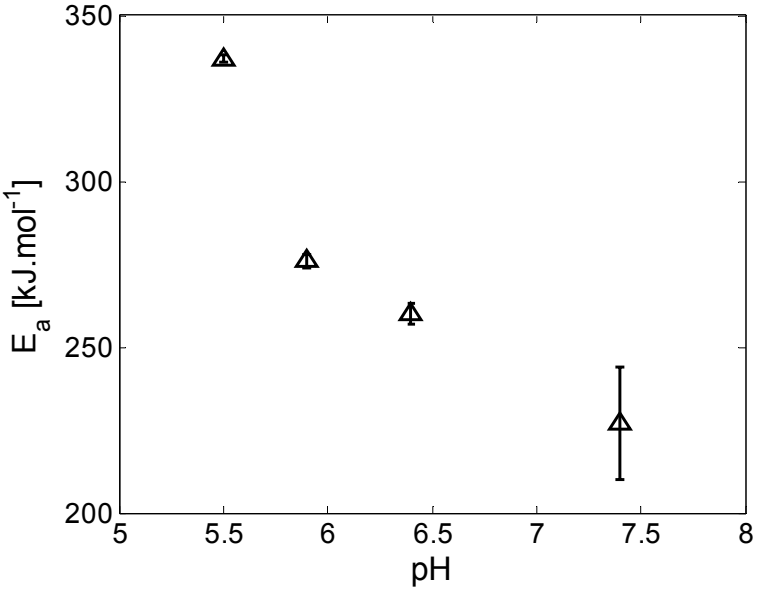

Figure 4-8. *pH dependence of the activation energy for β-LG deposition.*

and k_{dep}. Let us now consider the two rate constants written as the usual Arrhenius-type expression:

$$k_{den} = k_{den}^{0} e^{-\frac{E_a^{den}}{kT}}$$
$$k_{dep} = k_{dep}^{0} e^{-\frac{E_a^{dep}}{kT}} \qquad (4.3)$$

where k^0 and E_a are corresponding prefactors and activation energies, respectively. The overall rate of deposition R_{dep} is then proportional to

$$R_{dep} \sim k_{den}^{0} k_{dep}^{0} e^{-\frac{E_a^{den}+E_a^{dep}}{kT}} \qquad (4.4)$$

Now we can see that the activation energy corresponding to the deposition rates observed in our experiments is actually the sum of the two activation energies for the denaturation and the deposition step of the denatured proteins. On the other hand, the prefactor is given by the product of the two prefactors for the two steps. If the activation energy for denaturation is much larger than the activation energy for deposition of denatured protein, then the activation energy of the overall deposition step will be close to the activation energy for denaturation, as observed in our experiments. This is a reasonable assumption, since typical energy barriers for reaction limited aggregation of charge stabilized colloids are not more than 10-20kT [6], which translates into the activation energy of 25-50 kJ/mol, which is only about 10-20% of the activation energy values for the deposition rates in Figure 4-8. On the other hand, if the prefactor for the denaturation rate constant increases moderately with pH, while the prefactor

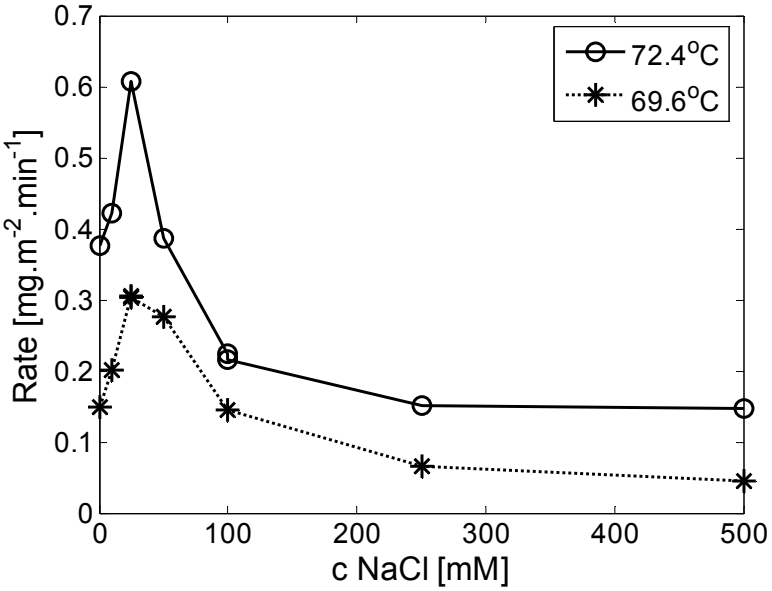

Figure 4-9. *Deposition rates as a function of NaCl concentrations at two temperature values. 10mg.ml^{-1} β-LG solution in 10mM HEPES at pH 5.9.*

for the deposition rate constant of denatured proteins decreases strongly with pH (as expected for aggregation in reaction limited aggregation regime [6]), then the prefactor for the deposition rate given by the product of the two decreases with pH, as observed in our experiments. It can then be concluded that the activation energy for the overall deposition rate follows the trend of the activation energy for denaturation, i.e. decreases with increasing pH, while the deposition rate follows the trend opposite to that of denaturation, but consistent with aggregation, i.e. decreasing with increasing pH.

Finally, we analyze the effect of salt concentration on the deposition kinetics of β-LG. In Figure 4-9 we show the measured deposition rates as a function of NaCl concentration for two temperature values. A maximum in the deposition rate was observed at a concentration of the NaCl in the 10mM HEPES buffer equal to about 30mM. After reaching the maximum, deposition rate decreases when further increasing the salt concentration. This qualitative behavior follows the well-known pattern of protein solubility in electrolyte solutions [29]. In general, the salt concentration influences both steps described in the deposition mechanism above. The observed maximum is caused by the combined effect of a reduced denaturation rate and an increased aggregation rate which follow an increase of salt concentration. NaCl belongs to the salting-out class of salts and thus stabilizes the native protein conformation thus decreasing the denaturation rate [152].

On the other hand, when increasing the salt concentration the charge of the protein is screened, and therefore the non-covalent aggregation is enhanced. Thus the maximum in the overall deposition rate with increasing NaCl concentration, observed in Figure 4-9, is related to the simultaneous decrease in the rate of the denaturation reaction and increase in the rate of aggregation.

4.4 Conclusions

Deposition of thin β-LG layers at the surface of silica-titania waveguides was monitored on-line by OWLS, an optical reflection technique related to ellipsometry and reflectometry. This is the first time that OWLS was used to quantitatively monitor kinetics of temperature driven deposition. The initial step in β-LG deposition is the primary coverage of the bare surface, which is partially reversible at ambient temperature. Primary coverage density at ambient temperature depends on β-LG concentration and pH. The irreversibly bound part of the primary layer is partially desorbed when exposed to pure buffer at elevated temperatures, but can be resaturated to its original density from the protein solution at ambient temperature. The temperature driven secondary deposition of β-LG is strongly dependent on temperature and pH. Deposition rates were decreasing with increasing pH from 5.5. to 7.4, in a trend similar to that for non-covalent aggregation of β-lactoglobulin in the bulk solution. Activation energies for deposition rates were decreasing with increasing pH, from 340kJ/mol at pH=5.5 to 230kJ/mol at pH=7.4, and were similar to the activation energies for denaturation of β-lactoglobulin in the bulk solution. This is consistent with the fact that protein deposition is the result of two independent processes occurring in series: protein denaturation followed by deposition of the denaturated protein. The effect of NaCl concentration on the deposition rate at elevated temperatures follows the inverse of a well-known pattern of protein colloidal stability, with a maximum deposition rate at moderate salt concentrations.

5 Investigation of thermally induced deposition from coffee extracts using optical waveguide lightmode spectroscopy

Abstract

Optical waveguide lightmode spectroscopy (OWLS) was used to monitor the formation of nanometer scale biomolecular layers on surfaces exposed to coffee extracts at temperatures up to 70°C, leading to macroscopic surface fouling over extended periods of time. OWLS measurements provided in situ characterization of the deposition process, and were complemented by scanning electron microscopy imaging and gravimetry measurements and by light scattering characterization of the extract solutions. The extracts were darkly colored mixtures containing proteins, polysaccharides and organic acids in both soluble and insoluble (colloidal) form suspended in an aqueous matrix, obtained in industrial conditions from ground roasted coffee beans. The first stage of deposition was fast adsorption of the soluble components leading to the formation of a primary molecular-scale layer. These primary deposits preconditioned the surface for the subsequent secondary deposit buildup. The secondary deposit thickness grew linearly in time, with a deposition rate strongly depending on the extract composition and temperature. Deposition rates at ambient temperature were largely independent of the extract concentration, although they increased moderately with decreasing extract pH between 6.5 and 4. Activation energies for deposition kinetics were determined for both original and diluted coffee extracts. The activation energy for the original extract (solid concentration 13.3% in weight) was found to be about 130 kJ/mol between 25 and 65°C. However, the activation energy for diluted extracts (solid concentrations up to 1.3% in weight) was only about 30 kJ/mol. A physical justification of these observations is attempted also through a comparison with the rate of cluster aggregation in aqueous dispersions measured by light scattering.

5.1 Introduction

Deposition and fouling play an important role in various industrial and biomedical applications, such as filtration, heat exchange, evaporation, deposition in blood vessels, implant biocompatibility and others. There are instances where deposition is desired, as long as it can be controlled, but others where it is not. A typical example is in food processing industries, where various liquids (solutions or dispersion) are treated in falling film evaporators in order to produce more concentrated solutions. Extensive fouling of evaporator surfaces can occur over a period of hours to days, depending on properties of a particular system. Fouling leads to build-up of a thick layer deposited on the evaporator surface, which causes a gradual decrease in the efficiency of the heat transfer and the eventual interruption of the production process in order to proceed to surface cleaning.

To study the kinetics of fouling various methods have been used. However, none of them can be considered as fully satisfactory. Conventional methods like gravimetry, have the advantage of relative simplicity and direct data interpretation. Another technique widely used in fouling studies is optical microscopy, providing visual characterization down to the micrometer scale. Scanning electron microscopy or atomic force microscopy are very powerful techniques, providing details in the nanometers range, but they often require sample manipulations, which lead to significant changes with respect to its original morphology. This especially concerns biological colloids, which are very sensitive to changes in the environment.

On the other hand, spectroscopic characterization methods can provide molecular level insight into the mechanisms governing the deposition process. Surface spectroscopic techniques, such as Optical Waveguide Lightmode Spectroscopy (OWLS), have the advantage of non-destructive, in situ monitoring of solid-liquid interfaces and provide a very useful tool to study surface adsorption and deposition. Their limitation is on the extent of the deposit that can be measured, which typically does not exceed a few tens of nanometers.

Most of previous studies about surface fouling refer to the deposition of proteins, mostly of animal origin. When protein solutions come into contact with an interface a spontaneous deposition is typically observed [153]. Published studies have been mostly focused on protein-surface interactions, mainly at ambient temperature. Protein deposition is affected by

pH, electrolyte concentration and temperature, which may specifically affect the protein functional groups or change its geometrical arrangement. Polysaccharides, which represent a significant component of the coffee extracts, tend to copolymerize with proteins at elevated temperatures (Maillard reaction), and the resulting copolymers are also expected to be subject to fouling.

Considering interphase interactions of deposited entities with solid surfaces, we can divide the deposition processes into two main groups:
i) The first group involves monolayer systems, where the main driving force for the deposition is due to the interaction potential difference between a bulk solution and a solid surface. Electrostatic double layer repulsion prevents charged polymer colloids from aggregating to each other, resulting in a stable deposited monolayer on the solid surface, which is made resistant against further deposition by the same electrostatic repulsive forces which keep suspended colloids stable in the bulk solution.
ii) The second group involves multilayer systems, where the repulsive interactions between the primary deposited layer and the bulk solution entities are reduced, so that subsequent deposition on the top of the primary layer can proceed. Multilayer growth can be achieved by altering the bulk solution composition, mainly through changes of pH and/or electrolyte concentration or, as in the system studied here, by increasing the temperature. Typically, fouling phenomena occur through the multilayer deposition. In this case the deposition is driven by interactions of previously deposited entities with those in the bulk, similar to aggregation in the bulk solution itself, so that fouling becomes independent from surface properties of the original substrate after the first few layers are deposited.

Multilayer film deposition at ambient temperature was studied by Picart et al. and Lavalle et al. [122, 154], where well defined polyelectrolyte multilayers and multilayer polyelectrolyte/protein films were investigated by OWLS and scanning angle reflectometry. It was shown that OWLS was able to monitor the deposition process from the initial deposited layer up to a thickness of more than 40 nm, while reflectometry could be used only after a few nanometers have been deposited up to about the same maximum thickness. This study of polyelectrolyte multilayer growth pointed out the important role of solution pH and charge distribution inside the film on the layer buildup mechanism.

Studies of Griesser et al. [155] on the deposition of complex protein mixtures (differing in the isoelectric point) for different bulk solution electrolyte concentrations on variously grafted polysaccharide layers and polymer coatings showed that coatings with substantial surface charge can be resistant to protein adsorption of the same charge, although they cannot be considered as a universal protein-resistant surface for all protein mixtures.

The effect of temperature, particularly at elevated temperature, on the deposition process has been rarely investigated. As reported in the review by Nakanishi et al. [34], this may be in part related to the associated experimental difficulties. The most commonly temperature driven fouling system studied in the literature is milk [138, 156-158]. This is a complex mixture of proteins, fats, carbohydrates, minerals and enzymes. There are two major components playing a role in milk fouling. Deposits formed between 60°C and 100°C are predominantly proteinaceous (with β-lactoglobulin as the dominant protein), while deposits formed above 100°C are rich in minerals. Thermal properties and aggregation and deposition behavior of proteins are in general strongly dependent on pH and on the presence of other components, such as calcium ions, lactose or casein. Upon heating at neutral pH, the proteins initially unfold and expose their inner hydrophobic cores and free thiol groups. This initiates the spontaneous aggregation of the proteins and also leads to their deposition on surfaces. At ambient temperature β-lactoglobulin forms monolayer due to its interaction with the bare surface, which is the typical behavior observed for various different proteins [29, 56, 137, 145].

The main scope of this paper is to investigate the mechanism of surface deposition from coffee extract induced by temperature increase. The developed temperature control setup for the OWLS provides unique insights into the deposition process in these systems. A better qualitative and quantitative understanding of the deposition process provides a rational basis for choosing possible process modifications leading to decreased fouling, and thus improves the heat transfer in evaporators used for the production of concentrated extracts.

In the following we investigate the primary layer formation on several different surfaces at ambient temperature and at various pH and electrolyte concentrations. Next, we investigate the secondary deposition driven by temperature on the primary layers previously deposited on a silica surface. The structure of deposited layers is also analyzed using scanning electron microscopy while the macroscopic deposition kinetics at longer times is measured by

gravimetry. Light scattering is used to monitor the corresponding aggregation processes, in the bulk of the liquid suspension for variously diluted extracts at various temperatures.

5.2 Experimental

5.2.1 Materials

The dry solid content of the coffee extract considered in this work is 13.3 wt% and the pH is 5.0. The dry mass of the suspension is constituted of 7.4% proteins, 35% carbohydrates, 3.2% minerals and 54.4% other organic molecules like melanoidines, organic acids and ash. At the natural pH of the coffee extract (pH 5) most of the proteins are negatively charged (36%), 1.2% are positively charged, 30% are polar uncharged (mainly aliphatic), 23% are aromatic and the rest is not determined. The sediments constitute 2% of the overall dry content. All solutions were prepared with ultra pure water (Millipore, 18MΩ) degassed under vacuum before use in order to reduce bubble formation in the spectroscopy cell.

Silica-Titania planar waveguides (OW 2400) were purchased from Microvacuum Ltd. (Budapest, Hungary). They consist of a 1-mm-thick AF45 glass substrate and a 180-nm thick $Si_{0.75}Ti_{0.25}O_2$ waveguiding surface layer, with dimensions of 1.2x0.8x0.1cm. The isoelectric point (IEP) of silica is 3.0 and of titania around 5.5 [37]. The waveguide layer has an approximate thickness of t_F~180nm and a refractive index of n_F~1.76. Five different surfaces have been used in this study to investigate the ambient temperature deposition process. These include the negatively charged silica and niobia surfaces, the positively charged alumina surface, and the hydrophobic polystyrene (PS) and poly(ethylene glycol)-3.5-poly(L-lysine) (PEG-3.5-PLL) surfaces. At elevated temperature only the silica modified surface has been used.

All the surfaces mentioned above have been obtained through a suitable coating procedure, covering the original waveguide film with layers 10-15 nm thick. The silica and alumina coated waveguides were purchased from Microvacuum Ltd. (Budapest, Hungary). The IEP of alumina is 8 [37]. The niobia coated waveguides were sputter coated on the original waveguide, using reactive magnetron sputtering (PSI, Villigen, Switzerland). The IEP of niobia is 4.3. Before each deposition experiment, all oxide surfaces were activated in NaOH solution at pH 11 for 3 hours. Afterwards, the waveguides were rinsed with Millipore water

and dried with nitrogen. This procedure activates the hydroxyl groups on the accessible surface.

A polystyrene (PS) layer approximately 15 nm thick was coated on the silanized original waveguide using 1% polystyrene dissolved in toluene at rotation speed 3000 rpm for 1 minute [38, 39]. PS used in this study was PS Standard 30'000 from Sigma-Aldrich (Product Number 81408) with M_p=32500, M_n=31000, M_w=32000, M_w/M_n=1.02. Silanization by hexamethyldisilazane, from Fluka, (Lot. No. 427155/1 44601) was used to make the originally hydrophilic oxide surface hydrophobic. PEG-3.5-(PLL) modified surface, a polycationic co-polymer positively charged at neutral pH [159], was spontaneously adsorbed on the negatively charged original surface from aqueous solution. PEG-3.5-(PLL) modified waveguides were obtained from the Laboratory of Surface Science and Technology, Department of Materials, ETH Zurich.

Prior to the SLS measurements the coffee extract was filtered with a 0.8 μm filter (Millipore) in order to remove bigger aggregates from the coffee extract. This does not change significantly the overall dried mass of the filtrate compared to the original extract. The removal of these particles is needed to reduce skewing of the measurements caused by big aggregates.

5.2.2 OWLS

Deposition experiments were performed in OWLS apparatus type OWLS 110 made by Micro Vacuum Ltd, Budapest, Hungary with integrated temperature control unit OWLS™ TC. Details about the technique, as well as physical principles and model used to calculate the signal can be found in the background section 1.4.1.1.

The waveguide is placed in a measuring cell, which is a channel 8mm long with rectangular cross section (0.8mm high and 2 mm wide) with a volume of 12.8μl, with entrance and exit ports to allow for continuous flow through. All delivery tubes and the measuring cell are made of Teflon®. The flow through operation mode has been selected in order to guarantee exposure to a fresh extract with constant composition over time. The waveguide parameters n_f and t_f are measured through a preliminary set of experiments where water is flushed through the deposition cell at ambient temperature.

In the deposition experiments at ambient temperature the waveguide surface was exposed to the coffee extract for at least one hour leading to completion of the primary deposited layer on the bare surface. The flow rate is held constant at 1ml.min^{-1} by the programmable syringe pump Vit-Fit (Lambda, Czech Republic), which provides a steady injection with strongly dumped flow rate pulses. After deposition, the sample is washed with water for at least 1 hour at ambient temperature. This was found sufficient to wash out all the electrolytes adsorbed on the deposition process.

For the runs at higher temperatures, a specific experimental procedure has been developed in order to preserve the reliability of the obtained results. All experiments were performed starting with a waveguide where a primary layer had been deposited at ambient temperature as described above. The problem is to heat such a waveguide to the desired temperature, without causing deposition. A solution could be to fill the measuring cell with water during heating, but this was found to lead to undesired degradation of primary deposits, particularly above 65°C. This does not occur if during heating the cell is filled with a diluted extract (0.034 wt%). This apparently protects the deposited layer from degradation, while the amount deposited from it is not significant compared to the amount deposited subsequently from a concentrated extract.

It is worth noting that to achieve a constant and steady operating temperature, the depositing solution was preheated in a separate pre-heating chamber to the target temperature. The temperature measurements were made in the temperature range 25 to 70°C.

Thus summarizing all the experiments at elevated temperature, which are presented in the result section, were performed according to the following protocol:

a) After the deposition of the primary layer at ambient temperature, the sample was washed with pure water, until the system reached steady state.
b) The measuring cell was filled with a diluted extract and the system was heated to the desired temperature in about five minutes.
c) When the requested temperature was achieved the depositing solution was injected in the measuring cell at a flow rate of 1ml.min^{-1} for the desired time.
d) Before cooling back to the ambient temperature, the diluted extract was re-injected in the measuring cell and the flow rate was stopped. As the temperature drops below 35°C (less than 3 minutes), washing with pure water was started. At this temperature

the deposited layer is stable in water. Within another 10 minutes the system reached the reference ambient temperature.

e) As a final normalizing step, the deposited sample was washed with water at constant flowrate 1ml.min^{-1} for one hour.

It is worth noting that in this procedure we take care to have equal and well defined conditions (pure water at 25°C) at the beginning and at the end of each deposition. This is achieved by measuring steps with pure water indicated in the points (a) and (e) above. This is particularly needed to equilibrate small electrolytes which are present in the extract and have to be removed from the final deposit. This guarantees that this waveguide is in the same conditions at the end of the experiment as at the beginning, and therefore, the difference in mass measured in these two conditions can entirely be attributed to the deposited solid layer.

After each deposition experiment the waveguide was cleaned by a short exposure to a strong oxidizing agent (3 seconds in chromic acid), followed by water rinsing. After the cleaning procedure, the position of the resonance spectra was checked and compared with the initially measured one to check that no waveguide damage occurred during cleaning.

5.2.3 Gravimetry

Gravimetry measurements were used as complementary experiments for OWLS measurements. Gravimetry is probably the most conventional method to study macroscopic deposition. It is based on weighing the difference between adsorbent weight before and after the adsorption process, and therefore its sensitivity is limited by the accuracy of the weighting procedure. The silica plate was placed into a gravimetry cell, constituted by a channel 180 mm long, with rectangular cross-section 0.5 mm high and 18 mm wide. All delivery tubes were made of stainless steel and the gravimetry cell was made of alumina. The channel geometry has been selected so that we can use the hydrodynamic model for laminar flow between two infinite parallel plates to calculate the hydrodynamic regime inside the channel. Using this model we can determine the flow rate to be fed to the channel so that the velocity gradient at the surface of the waveguide is equal to that in the OWLS cell [102]. The calculated velocity gradient in the OWLS cell is about 500 s^{-1}, which corresponds to a volume flow rate in the channel of 32ml.min^{-1}. A peristaltic pump was used to deliver the extract preheated to the desired temperature shortly before entering the measurement cell. The entire

gravimetry cell was held at constant temperature. Washing with pure water was performed for one hour after the cooling step as in the OWLS experiments.

5.2.4 Light scattering

Light scattering experiments were performed on coffee extract in order to compare the aggregation in the liquid bulk with the surface deposition. All measurements have been taken with a small angle light scattering instrument (Mastersizer 2000 by Malvern) after preliminary filtration with 0.8μm filter. The original extract was heated and kept for one hour at constant temperature in the range 25-80ºC so as to undergo Brownian aggregation. Samples were withdrawn at fixed times and quickly diluted 200 times with pure water in order to stop aggregation and avoid multiple scattering in the light scattering measurements. Alternatively, the extract was immediately diluted and then heated at the desired temperature so as to monitor directly in-situ the aggregation process by light scattering without any sampling procedure.

5.3 Results and discussion

5.3.1 Estimation of OWLS parameters

In order to evaluate the deposited mass from the measured *N(TE)* we need to supply to Eq. (1.13) and (1.15) the proper optical parameters, which correspond to the conditions inside the deposition cell. The refractive indices n_S and n_C, for the waveguide support and the cover liquid, respectively have been taken from the literature or measured independently at various temperatures and are summarized in Table 5-1. The waveguide thickness t_F and refractive index n_F may vary slightly depending on the measurement conditions and therefore have been evaluated before each experiment as discussed in the context of Eq. (1.12).

Let us now consider the evolution of the derivative of the dielectric constant with respect to the mass concentration of deposit $dc/d\varepsilon$ which appears in Eq. (1.15) . For this the refractive indices of variously diluted coffee extracts were measured by refractometer at wavelength 632.8nm for four different temperatures (20, 25, 40, 60°C). The measured values are provided in Table 5-1 where x_E represents the weight concentration of solid content in coffee extract suspension. Since the relative dielectric constant can be computed from the refractive indices in the table as $\varepsilon = n_C^2$, the derivative $dc/d\varepsilon$ (where c=x_E) can be readily obtained. This procedure has been repeated at the four considered temperatures and obtained values are fitted by following expression, where T is given in ºC:

$$\left(\frac{dc}{d\varepsilon}\right)_T = -3.47\cdot10^{-6}T^2 + 4.028\cdot10^{-3}T + 1.642 \quad [g/cm^3] \qquad (5.1)$$

As can be seen for this particular case, the term $dc/d\varepsilon$ changes just very little within measured temperature range 20-60°C (i.e. a temperature change of 40°C leads to an increase of 3%). Here we can notice that the value determined experimentally at ambient temperature for the coffee extract (1.74 g.cm^{-3}) is similar to the value conventionally used to determine the deposited mass from various biomolecular systems (~1.89 g.cm^{-3}) [160].

Table 5-1. *Refractive indices as a function of temperature. T denotes temperature in °C and* x_E *is the weight concentration of solid content in coffee extract suspension (in g.cm*$^{-3}$*),* $n_{C,E}$ *denotes refractive index of coffee extract and* n_{C,H_2O} *denotes refractive index of water.*

Parameter	25°C	T [°C]	Source
n_{C,H_2O}	1.331144	$n_{C,H_2O}^{25^oC} - \frac{75453.41\Delta T + 2340.431\Delta T^2 + 6.363191\Delta T^3}{T.10^7 + 65.7081.10^7}$; *where* $\Delta T = T - 25$	[147]
$n_{C,E}$	$0.2090x_E + n_{C,H_2O}^{25^oC}$	$(4.2725.10^{-6}T^2 - 4.665.10^{-4}T + 2.1795.10^{-1})x_E + n_{C,H_2O}^{T}$	measured by refractometer
n_S	1.525718	$n_S = n_S^{25^oC} - 1.23.10^{-6}T$	[147]

5.3.2 Deposition at ambient temperature

A typical result of the OWLS measurement is shown in Figure 5-1 in terms of mass deposited during a primary exposure of two waveguides, the silica and the polystyrene coated ones, to the coffee extract (solid concentration 13.3 wt%). After equilibration with pure water the extract was pumped at constant flow rate through the measuring cell, and at the end of the deposition process the flow was switched back to pure water and the washing process started. These two times are indicated by arrows in the figure. Typical deposition coverage was about 1 mg.m^{-2} after washing with pure water for one hour at ambient temperature.

It can be seen that in the case of the hydrophobic polystyrene coated waveguide the deposited mass increased almost instantaneously to about 2 mg.m^{-2}, and then under very slow growth, which in the following we refer to as the secondary growth. During washing there was a rapid decrease of the deposited mass to about 1 mg.m^{-2}, followed by a period of time where the mass decrease was so slow that we can consider the deposit as stable in time. When the silica surface was exposed to the extract, the deposited mass was growing rapidly for a longer time, i.e. about half an hour, followed again by a steady but very slow increase corresponding to the so-called secondary growth. Also in this case washing starts very fast and then slows down considerably, leading to a stable deposit. The mass measured at this point represents the amount of material irreversibly deposited on the surface, since the waveguide is at the same conditions as at the beginning of the experiment (in contact with pure water at ambient temperature). And this will be referred to in the following as irreversible primary layer.

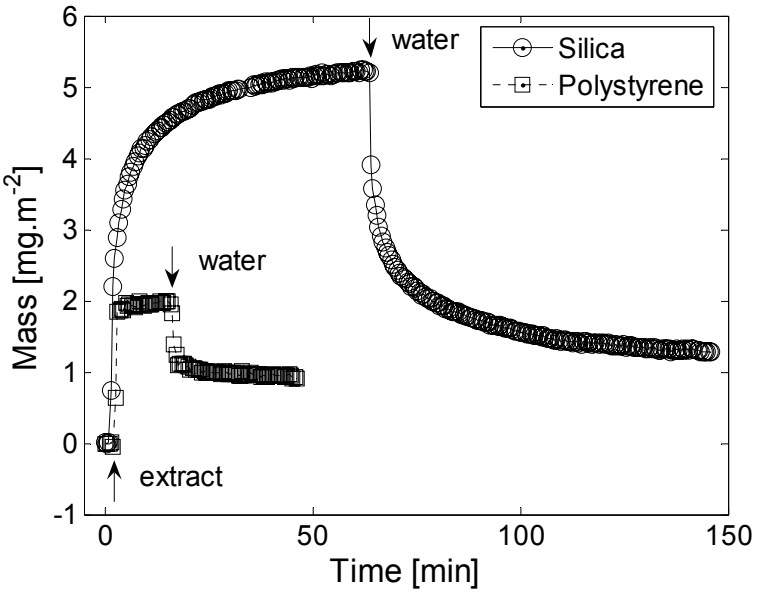

Figure 5-1. *Primary exposure of silica and polystyrene surfaces to the original extract (13.3 wt%), pH 5.5 at 25ºC.*

It is worth noting that while the response of the neutral polystyrene surface is almost instantaneous, the one of the charged silica surface is slower and more pronounced. This is due to the fact that in the second case not only the extract material, but also all the various electrolytes present in the solution are adsorbed or deposited on the surface. These species are however removed during washing, so that it can be observed that the irreversibly deposited amount is very close to that obtained for polystyrene. This can be confirmed by the data reported by Nellen et al. [119] for simple electrolyte solutions, which indicate typical saturation times of about 40 min.

The sensitivity of the silica waveguide to electrolytes is well known and the usual way to eliminate it is to use a background medium with the same electrolyte composition as the covering liquid under examination. Since the coffee extract used here was a complex buffering mixture, it was not possible to prepare a matching background medium. Therefore, in addition to the deposition of the extract components, we need to take into account the partitioning equilibrium between the solution and the solid surface. The closer the solution pH is to the isoelectric point of a given surface, the less significant the adsorption of electrolytes is [110]. When the silica surface is exposed to an electrolyte solution at pH=3, which corresponds to its isoelectric point, there is no charging response from the waveguide surface, similarly to the case of neutral polystyrene surface.

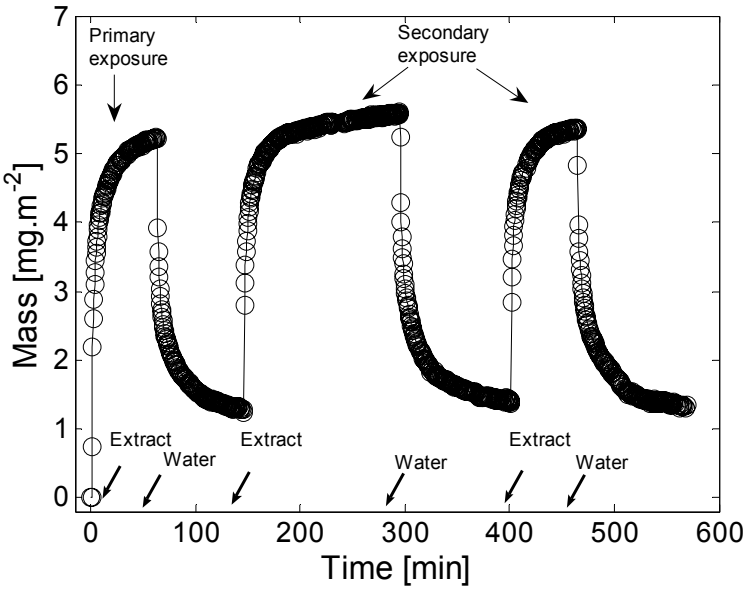

Figure 5-2. *Three subsequent exposures of silica surface to the original extract at ambient temperature.*

In Figure 5-2 we show the results of deposition measurements for multiple subsequent exposures of a silica coated waveguide to the coffee extract. The first exposure leads to the formation of an irreversible primary layer of about 1.2 $mg.m^{-2}$ as shown in Figure 5-1. The second and third exposures exhibit a very similar behavior. It is worth noticing that for all three subsequent exposures, although the secondary growth region was extended over different times, the final irreversible deposit was substantially the same. This indicates that the material deposited during secondary growth is weakly bounded to the surface and is easily removed by washing with water.

The values of the irreversibly deposited mass obtained after the primary exposure to the extract on various surfaces are summarized in Table 5-2. Note that the obtained values are in the same range as those observed for pure proteinaceous solutions deposited on silica surfaces [34]. Silica and niobia surfaces (isoelectric point at pH 3 and 4, respectively) are negatively charged in contact with the extract at its native pH 5 and exhibit the same thickness of the deposit. A comparable deposited mass was observed on polystyrene (neutral hydrophobic surface) after 15min of exposure, thus confirming that the irreversible primary layer builds up almost completely after quite a short time. The amounts deposited on PEG-3.5-PLL (positively charged at pH 5 since it contains sterically isolated carboxyl groups) and alumina surfaces (positively charged) were smaller than those in the previous cases.

Table 5-2. *Deposited amount of the irreversible primary layer from the coffee extract on various surfaces at ambient temperature.*

Surface	Extract Solid Content [wt%]	Deposited Mass [mg.m^{-2}]
Silica	13.3	1.2
Silica	1.33	1.1
Silica	0.034	1.1
Niobia	13.3	1.2
Alumina	13.3	0.7
PEG-3.5-PLL	13.3	0.4
Polystyrene	13.3	0.90

It is remarkable that the extract dilution does not lead to any substantial difference in the deposited amount of primary layer, as shown by data in Table 5-2 for silica coated waveguide. These data confirm the result reported by Paschke et al. [86] that the electrostatic potential of the waveguide surface has only a moderate influence on the secondary deposition and can be efficiently screened by the thin primary irreversible layer, whose properties govern the following deposition process. This can be justified by the fact that the extracts considered here contain a substantial amount of soluble ions so that the expected electrical double layer thickness is below 1 nm. Therefore electrostatic surface effects act only over a very short range, which is moreover further screened by the irreversible primary layer.

5.3.3 Deposition at elevated temperatures

Prior to the deposition measurements, the temperature response of the bare waveguide in pure water was investigated. The waveguide thickness t_F and refractive index n_F were evaluated using Eq. (1.12), with the n_C and n_S values reported in Table 5-1. As shown in Figure 5-3, an increase in the waveguide thickness and a decrease in refractive index were observed with increasing temperature. We note that the temperature response slightly varies between individual waveguides, although the general trend is always the same and relative changes in waveguide properties are very similar. As indicated by Saini et al. [147] the change in the waveguide thickness can be attributed to thermal dilatation of the waveguide material.

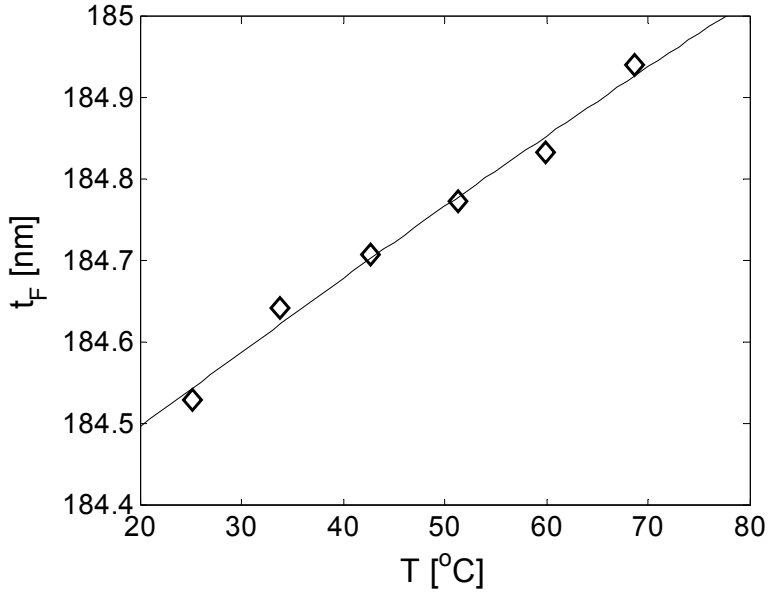

Figure 5-3a. *Waveguide thickness as a function of temperature.*

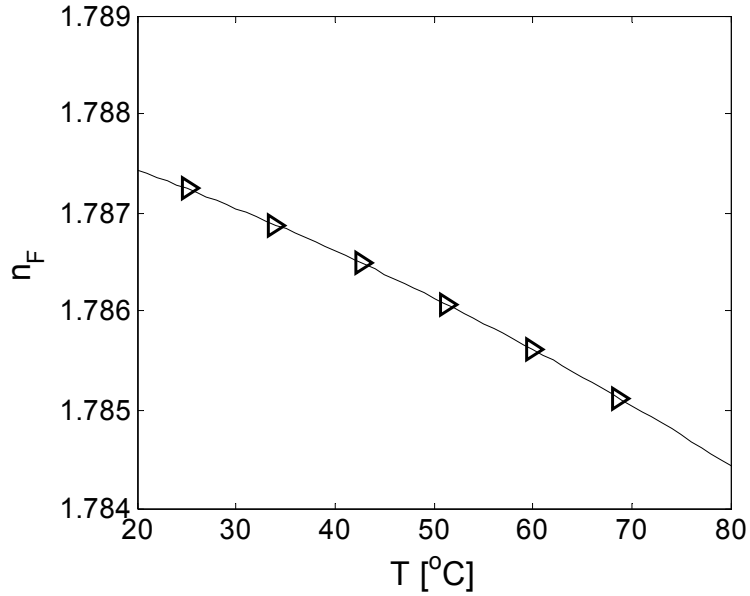

Figure 5-3b. *Waveguide refractive index as a function of temperature.*

It is worth noting that in the temperature response experiments conducted in pure water, when the waveguide was cooled down to ambient temperature, the waveguide parameters were slightly different compared to those before heating. This may indicate a gradual hydrolysis and possibly dissolution of the silica coated waveguide, particularly at higher temperatures. Therefore we minimized the heat exposure of the waveguide in water to a minimum necessary time.

Table 5-3. *Experimental procedure for secondary deposition experiment at 60°C (see Figure 5-4a, b).*

Period	Time [min]	Bulk Solution	pH	Flow Rate [ml.min^{-1}]	Temperature [°C]
A	0-11	water	6.5	1	25
B	11-17	0.034 wt% extract	5.6	0	heating
C	17-27	13.3 wt% extract	5	1	60
D	27-32	0.034 wt% extract	5.6	0	cooling
E	32-90	water	6.5	1	25

On the other hand, changes of the waveguide optical parameters were not observed during the extract deposition runs. The thin layer deposited from the extract can effectively protect the waveguide from hydrolysis and dissolution reactions in two ways. First, it can partially isolate the oxide surface from contact with the solution and secondly it reduces the mass transfer from the oxide surface to the bulk liquid. All the other parameters needed to estimate the deposited mass from Eqs. (1.13) and (1.15) are reported in Table 5-1 or Eq. (5.1).

In Figure 5-4a and Figure 5-4b we show a typical deposition experiment for the coffee extract at 60°C. All deposition runs started from a waveguide which had already undergone a primary deposition at ambient temperature, and therefore was covered by an irreversible primary layer. Accordingly, we refer to these experiments as secondary deposition runs in the following sections. The adopted experimental procedure is described in the experimental section and in the case of the experiment in Figure 5-4 is reported in detail in Table 5-3. The last column in the table refers to the temperature which is shown in Figure 5-4a.

In Figure 5-4b the deposited mass is given as a function of time for silica coated waveguide for the different periods listed in Table 5-3. It is seen that as soon as the extract enters the measuring cell (period C) the deposited mass increases abruptly while at later times it follows an almost linear, relatively slow, increase which constitutes the secondary growth of the deposit. The first jump in deposited mass is due to the adsorption of the small electrolytes on the primary irreversible layer. This is a rather fast process and the deposition of large molecules in such a small time is probably negligible for the secondary deposition runs. In

order to determine the deposited mass it is necessary to bring the surface of the waveguide after deposition at the desired temperature back to its initial state, i.e. in the presence of pure water at 25ºC. The total irreversibly deposited mass of the coffee extract is then computed as the difference between the mass measured at ambient temperature in water before the deposition (point M_1) and after water washing for one hour (point M_2). The corresponding average deposition rate is given as the increment of deposited mass divided by the exposure time at the elevated temperature.

It is worth noting that the average deposition rate determined by this method agrees well with the one obtained from the slope of the deposited mass curve as a function of time during period C in shown in Figure 5-4b. This is further supported by data collected for a moderately diluted extract over a range of temperatures shown in Figure 5-5. This confirms that the two ways of measuring the deposition rate, referred to as online and off-line respectively, are comparable. Therefore the solid layer deposited on the waveguide at the end of the process corresponds to the secondary growth measured during period C. The electrolytes and other reversibly adsorbed species responsible for the sudden jump in the adsorbed mass at the very beginning of period C are all removed during the washing period E.

As can be seen from the semi logarithmic plot in Figure 5-6, the deposition rate of the original extract (solid circles) gradually increases by over two orders of magnitude when the temperature increases from 25°C to 65°C, beyond which the deposition rate does not increase any further. The apparent plateau in the deposition rate above 65°C was also confirmed by gravimetry measurements (see section 5.3.5) and it could be due to a diffusion limited regime for the transport from the bulk to the deposited layer.

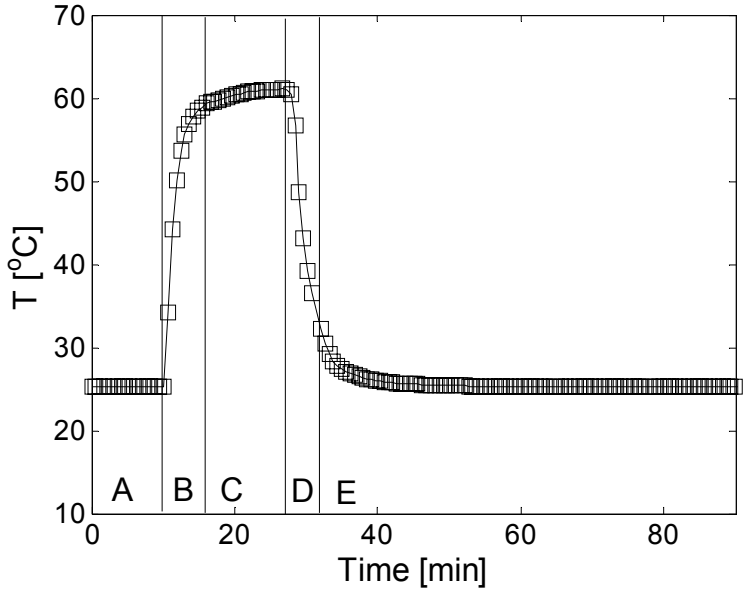

Figure 5-4a. *Cell temperature for secondary deposition experiment at 60°C.*

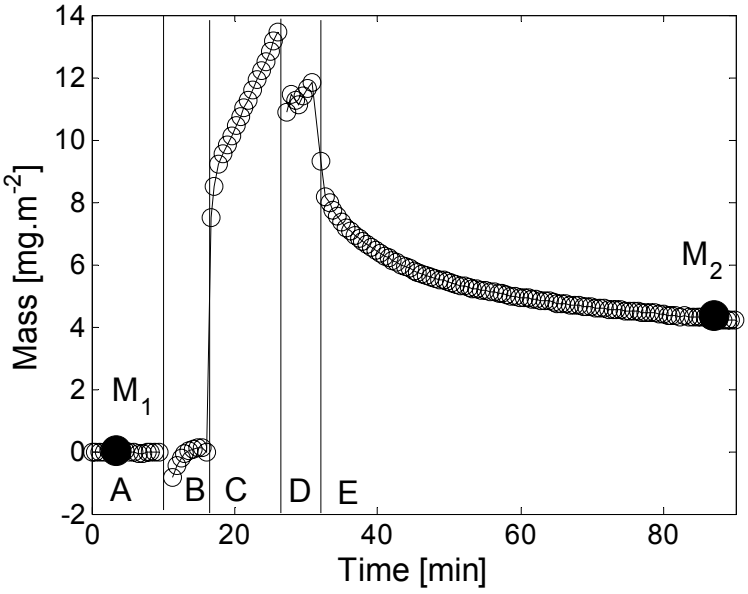

Figure 5-4b. *Deposited mass for secondary deposition experiment at 60°C.*

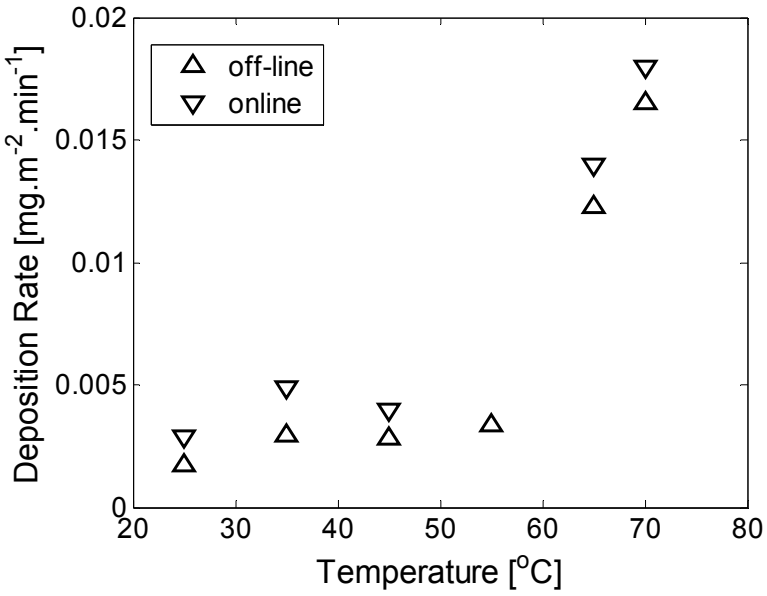

Figure 5-5. *Comparison between deposition rates determined online and off-line for diluted extract (1.3 wt%) as a function of temperature.*

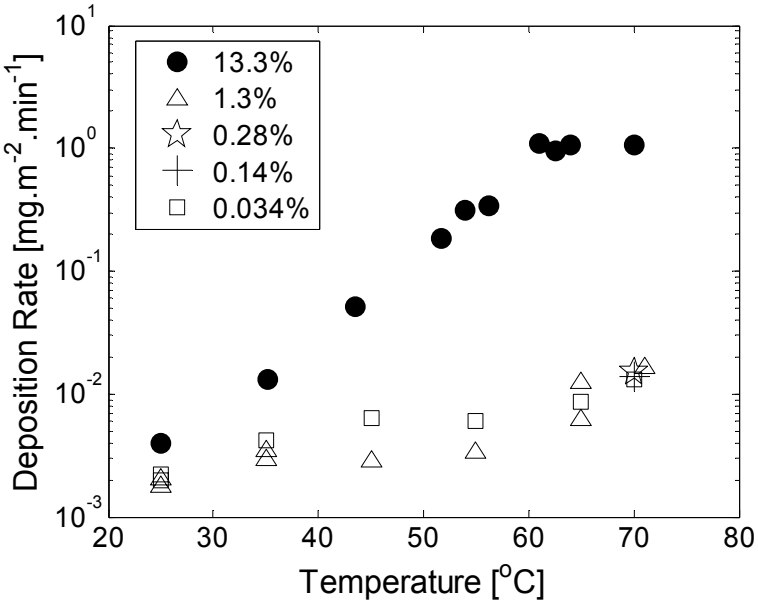

Figure 5-6. *Deposition rates for the original extract as a function of temperature.*

5.3.4 Effect of extract composition on deposition kinetics

The assembly of molecules and particles among themselves as well as at interfaces is controlled by their mutual interactions. Repulsive interactions, typically electrostatic or steric, between depositing entities are required in order to prevent mutual aggregation as well as surface fouling. Electrostatic interactions between colloidal particles are modulated most readily by solution pH and electrolyte concentration. Coffee extracts considered here contain molecules and colloidal particles with dissociable groups which are negatively charged at the normal extract pH values ~5, as indicated by electrophoretic mobility measurements of diluted extracts (zeta potential –15 mV).

Table 5-4. *Influence of pH on secondary deposition rates of concentrated coffee extract.*

Temperature [°C]	pH	Deposition Rate [$mg.m^{-2}.min^{-1}$]
25	4	0.006
	5	0.003
	6.5	0.003
65	4	1.6
	5	1.2
	6.5	0.3

In an attempt to control deposition kinetics through electrostatic interactions, we studied deposition by modifying pH to values 4.0 and 6.5 (from the natural pH of 5) at ambient temperature and at 65°C. As expected, by increasing pH the negative charges on the colloids increase, thus leading to slower deposition. In particular, the data reported in Table 5-4 show that the increase of pH from 4 to 6.5 results in a decrease of the secondary deposition rate by a factor of 2. An even more pronounced decrease was observed at 65°C, with a reduction of the secondary deposition rate by a factor of 5 when increasing pH from 4 to 6.5.

The measured secondary deposition rates as a function of temperature are shown in Figure 5-6 for extracts at various solid concentrations: the original extract at 13.3 wt% and those diluted with pure water to 1.3, 0.28, 0.14 and 0.034 wt%. We note that due to a strong buffering effect of the coffee extract, the pH values of the diluted extracts were close to that of the

original extract (pH 5), with the highest value of pH 5.5 for the most diluted extract (0.034 wt%). From the data in the figure we observe that the rate of secondary deposition at the ambient temperature is only little sensitive to the extract concentration. Dilution of the original extract by a factor of up to 400 results in not more than a two fold decrease in the deposition rate, which at ambient temperature is only barely distinguishable from the experimental error. In particular, we see that the deposition rate for diluted extracts (solid concentration below 1.3 wt%) is largely independent of the extract concentration. This could be explained by recalling that there is always a reversibly deposited layer present at the surface in contact with the extract. Let us assume that this reversible layer is dense enough at all concentrations considered here so as to effectively saturate the underlying irreversibly bound layer. Then the rate of growth of the irreversible layer may be simply driven by incorporation of the loosely deposited material saturating the interface, and hence it would be essentially independent from the solution composition. However, this does not explain why the deposition rates at elevated temperatures from the original extract are much higher than from diluted ones.

In Figure 5-7 we show the Arrhenius plot for deposition rates, where the data for the original (13.3 wt%) and the most diluted extract (0.036 wt%) are compared. The activation energy for deposition of the original extract was found to be about 130 kJ/mol, corresponding to an increase of the deposition rate by more than two orders of magnitude between 25 and 65°C. However, the deposition rate for the diluted extract, increased by less than 10 fold between 25 and 70°C corresponding to an activation energy of about 30 kJ/mol. The difference in activation energies between the original and diluted extracts indicates that there is a different deposition mechanism operating in the two cases. In order to consider this in more detail, let us look first at aggregation in bulk coffee extracts upon their heating.

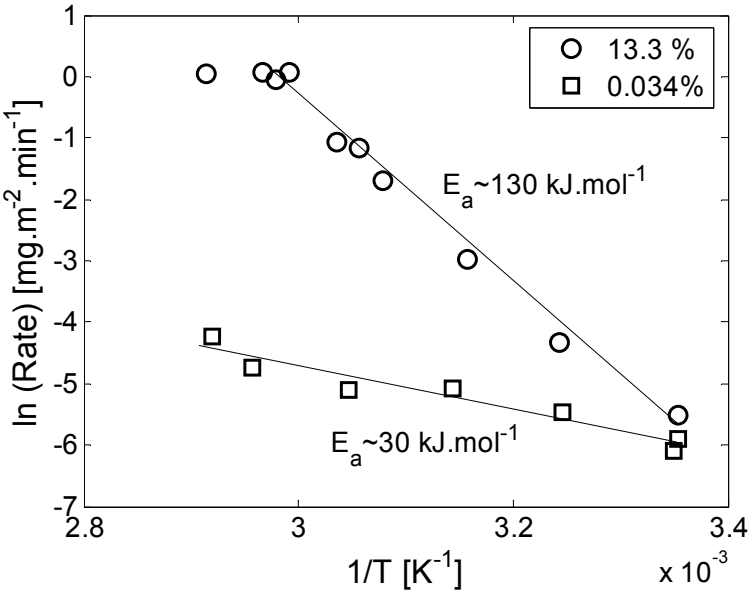

Figure 5-7. *Arrhenius plot of the deposition rates.*

As fouling is primarily driven by interactions between depositing entities themselves rather than between depositing entities and the original surface, it is instructive to consider a possible relationship between surface deposition and aggregation in the bulk suspension. Here we used static light scattering to investigate the Brownian aggregation of colloidal particles in the bulk extracts at various dilutions and temperatures. In Figure 5-8a we show the measured scattered light intensity for the 200 times diluted extract after heating for 1 hour at the indicated temperatures. The pattern corresponds to gradual aggregation of smaller particles to larger clusters. There is a strong increase in the mean radius of gyration with increasing temperature, as can be seen in Figure 5-9. The observed behavior is very similar to the one found in Figure 5-6 for the rate of deposition. The fast increase at about 60°C suggests that the underlying mechanism for the two processes may be the same.

This is further supported by the fact that the activation energy for deposition from diluted extracts observed in Figure 5-7 is of the same order of magnitude of the so-called reaction limited aggregation, where a typical energy barrier for aggregation is on the order of 10kT [6], corresponding to the activation energy of 25 kJ/mol. These results indicate a correlation between irreversible aggregation in solution at elevated temperatures and secondary surface deposition in diluted coffee extracts.

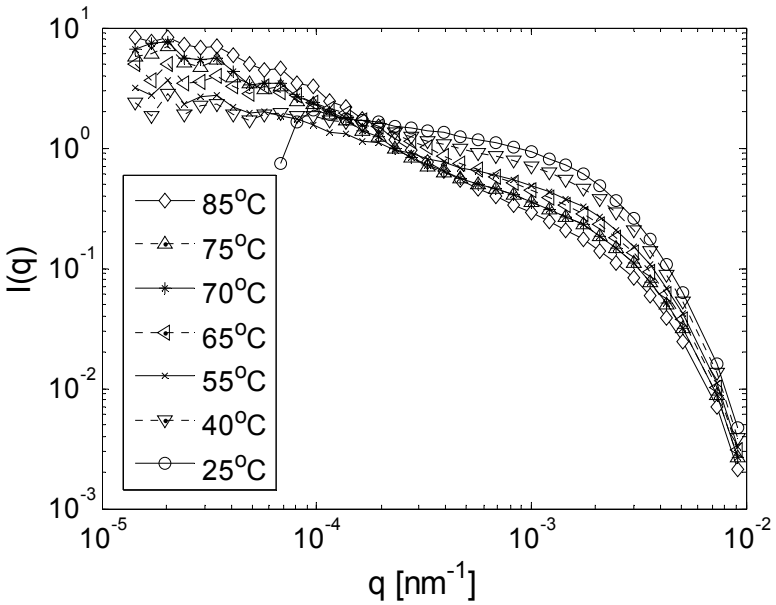

Figure 5-8a. *Scattered light intensity measured by SLS in 200 times diluted extract after aggregation at the indicated temperatures.*

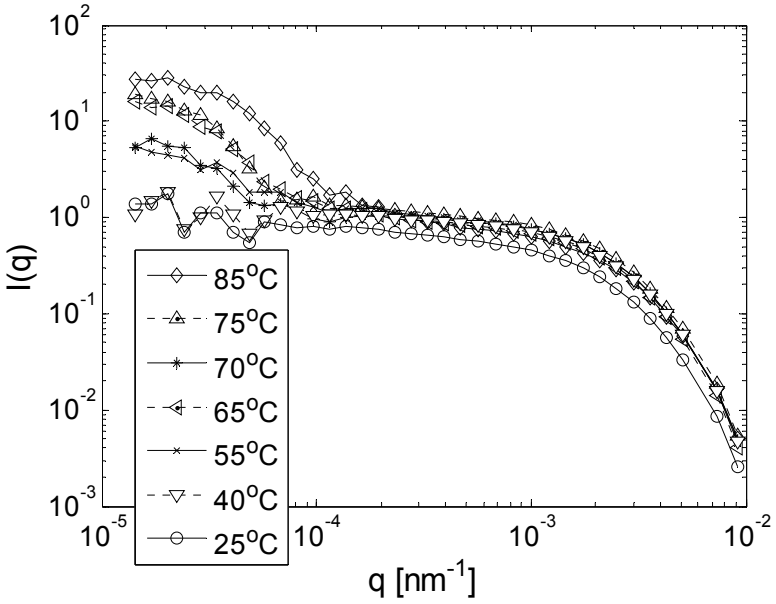

Figure 5-8b. *Scattered light intensity measured by SLS in the original extract after aggregation at the indicated temperatures.*

A scattered intensity pattern very different from the one observed in diluted extracts was found when the original extract was heated at higher temperatures, as shown in Figure 5-8b. It appears that large particles of the order of tens of microns emerge after heating at elevated temperatures, although a good portion of the original colloidal particles is still present in the system. This indicates that in the original extract there is an irreversible formation of large

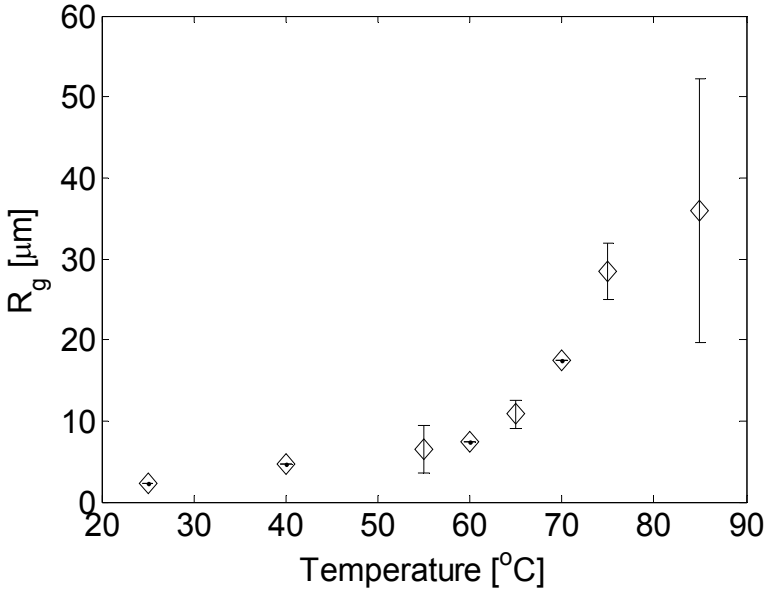

Figure 5-9. *Radius of gyration measured by SLS for the 200 times diluted extract as a function of the aggregation temperatures.*

aggregates upon heating, indicative of an association or a phase transition, as opposed to the gradual cluster-cluster aggregative growth seen in diluted extracts. These larger aggregates can then either directly assemble at the surface, or be deposited from the solution, in either case leading to much higher deposition rates compared to diluted extracts. These results suggest that the aggregation and deposition mechanisms in coffee extracts are strongly dependent on their concentration. It is worth noting that concentration driven association phenomena have been observed using light scattering in moderately concentrated solutions of proteins [161] and polysaccharides [162], as well as in coffee extracts using viscosimetry [163].

5.3.5 Microscopy and gravimetric study

Scanning electron microscopy images of surfaces before and after deposition were taken in order to complement the information obtained by OWLS. Images of bare silica surface are flat and featureless down to resolution length scales of tens of nanometers, as shown in Figure 5-10a. The primary layers detected by OWLS are not visible by SEM and the corresponding image looks like those of the bare surface, even when a scratch to the primary layer is done. Missing contrast between the original surface and the deposited layer indicates information that the primary layer is uniform and homogeneous at the used resolution.

a)

b)

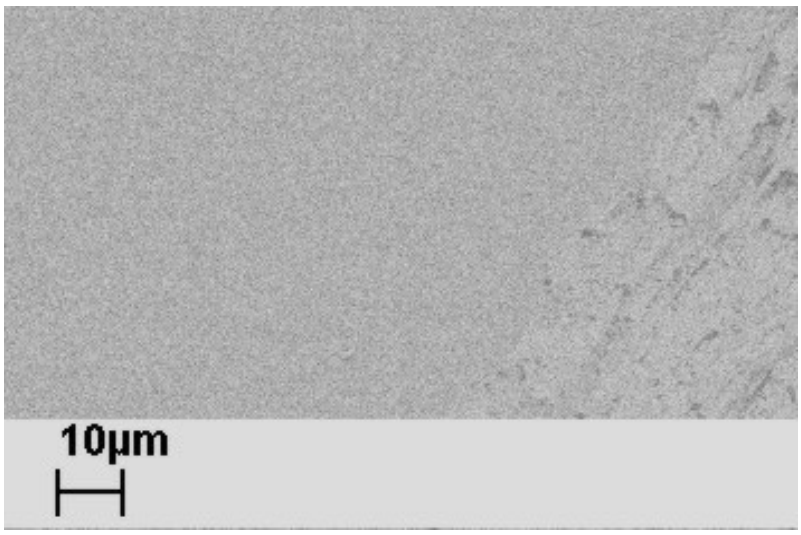

c)

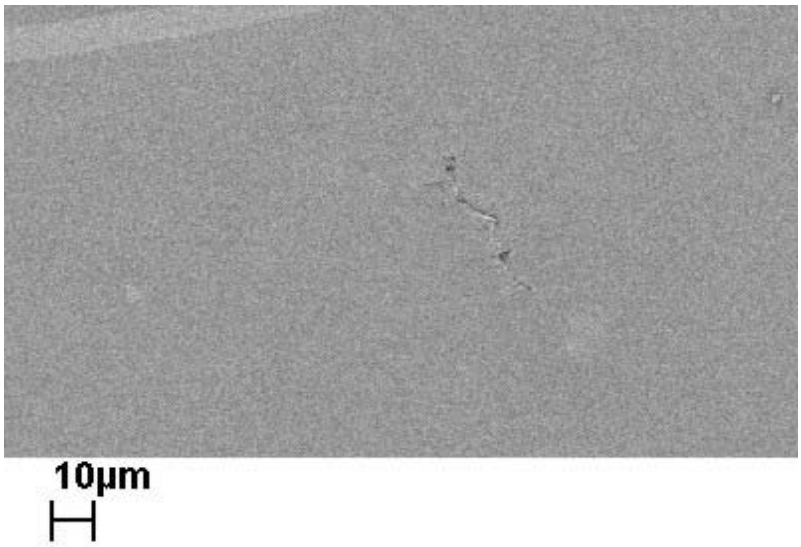

Figure 5-10. *a) SEM images of silica surfaces taken before deposition, b) after secondary exposure at 50°C for 5 minutes, c) after secondary exposure at 70°C for 5 minutes.*

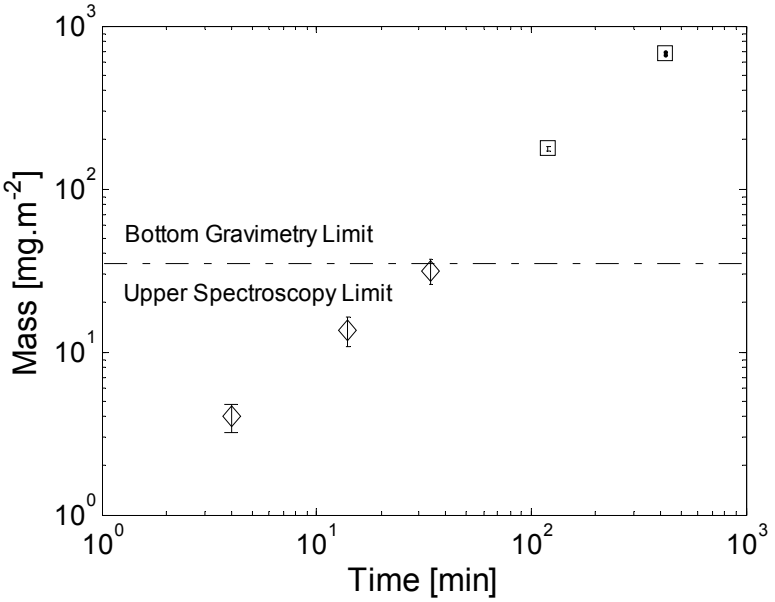

Figure 5-11. *Deposited mass as a function of time at 65°C for the original extract. Diamonds: OWLS; squares: gravimetry.*

The secondary deposited layer on silica surface exposed to the extract at 50°C for 5 minutes can be made visible through SEM by scratching it to enhance the contrast between the layer and the surface (Figure 5-10b). The mass of the secondary deposit measured by OWLS for these conditions was about 1mg.m^{-2} which was on the top of the primary layer constituted approximately by another 1 mg.m^{-2}. The contrast between surface and deposited layer was stronger in the case where the surface was exposed to the extract at 70°C for five minutes, as shown in Figure 5-10c. In this case the mass measured by OWLS during the secondary deposition was 6 mg.m^{-2}, again on top of 1mg.m^{-2} of primary layer. Visual inspection of the SEM pictures indicates that in all cases the deposited layers were homogeneous and uniformly covering the exposed surfaces.

We further used gravimetry in order to measure the deposition rates at longer deposition times, and therefore for thicker deposited layers. As mentioned above, the gravimetry measurements can be performed only after an appreciable amount of mass has been deposited, which imposes a lower limit to the applicability of this method, which happens to be very close to the upper limit of OWLS. Therefore with this technique one can compare the deposition rates and deposited mass over longer time for dense, concentrated extracts and follow the history of the deposition process beyond the limits of OWLS. This also gives us the opportunity to verify the compatibility between these two techniques.

One important aspect in the design of these experiments is that in the measurement cells used for gravimetry and OWLS the hydrodynamic conditions at the deposition surface should be similar. As described in the experimental section this is obtained by a proper design of the gravimetric cell which in the experiments discussed in the following led to a velocity gradient at the surface equal to about $500s^{-1}$. Measurements were performed for the coffee extract at 65°C. The results in Figure 5-11 show that the deposited mass as a function of time increases in a log-log plot in a consistent manner going from the short time OWLS measurements (diamonds) to the long-time gravimetric measurements (squares). This leads us to comparable deposition rates as determined by the two methods equal to about 1 $mg.m^{-2}.min^{-1}$.
Gravimetric experiments have been performed using the original extract to measure the deposition rates at higher temperatures, i.e. 73 and 83°C.The obtained values are very similar to the one measured at 65°C, thus confirming the plateau in the deposition rate shown in Figure 5-6 which was obtained by OWLS.

5.4 Conclusions

The deposition kinetics of an industrial coffee extract at wide range of temperatures was studied by OWLS and gravimetry. The first step in deposition formed a primary layer of about 1 $mg.m^{-2}$ on all the considered surfaces. At ambient temperature the secondary exposure of the primarily covered surface leads to reversible deposition, attributed to the electrolyte adsorption. Temperature and concentration were found to be the main operating parameter driving deposition, which reached a maximum rate in the original extract at 65°C. Gravimetry was used as an independent method to measure the deposition rates. A comparison of the deposition rates, measured by gravimetry at longer times and by OWLS at shorter times, shows a very good consistency between the two methods. Deposition rates at ambient temperature were only little dependent on extract concentration, although they increase moderately with decreasing extract pH between 6.5 and 4. Activation energies for deposition kinetics were determined for both the original and diluted extracts. The activation energy for the original extract (solid concentration 13.3 wt%) was found to be about 130 kJ/mol between 25 and 65°C. However, the activation energy for diluted extracts was only about 30 kJ/mol. This can be due to the fact that the surface in contact with the diluted extracts is saturated with a loosely bound layer of material, which gradually becomes incorporated into irreversibly bound deposits. Therefore the buildup of the irreversibly bound deposit is independent of the

extract concentration, provided that it is sufficient to reversibly saturate the available surface. In contrast, the original concentrated extract exhibits an irreversible association of suspended entities to large clusters at elevated temperatures, as indicated by static light scattering, leading to a different deposition mechanism with much higher deposition rates at higher temperatures.

6 Conclusion and Outlook

In this thesis a novel approach to measure on-line and in-situ deposition kinetics of various colloidal systems at elevated temperatures has been developed. Optical waveguide lightmode spectroscopy, which is based on the interaction of standing electromagnetic waves reflected from an optical interface with deposited material accumulated at the interface, was used for deposition kinetics measurements.

Scope is to investigate the mechanism of deposition of complex colloidal systems at a solid-liquid interface. A systematic investigation of the collected data revealed the need of a better understanding of the oxide sensor response to changes in the electrolyte composition as well as in the role of temperature.

Since the electrolyte an effect is related to the changing of the oxide sensor surface, one possibility to avoid it is to spin-coat the sensor with a polymer. The applicability of this approach is practically determined by two considerations. One is the thickness of a coating, which has to stay below a certain level in order for the sensor to provide internal reflection. On the other hand a minimum thickness is required by the film stability and the coverage homogeneity. Often in fact, the presence of the electrolyte and too high temperatures caused the layer instability or even its destruction.

A major part of the thesis was devoted to characterize the initial interaction mechanism between temperature sensitive solution of depositing biomolecules and variously modified sensor surfaces. The correct understanding of the sensor response allowed us to measure and validate the deposition kinetics using various biological suspensions, which were subsequently compared with other independent measurements. From this clear picture of the deposition mechanism and of the role played by the temperature has been drawn.

Monitoring deposition using a planar waveguide sensor is based on measuring the optical properties of the deposited layer, accumulated on the top of the sensor waveguide, by very small time steps. The advantages of this method can be summarized as follows:

- high accuracy, sensitivity and resolution
- relatively simple handling
- easy to maintain
- on-line, in-situ monitoring of deposition
- ability to monitor deposition at elevated temperature
- ability to probe very concentrated colloidal suspensions

- low sample consumption

Furthermore, the measurements made by OWLS were verified by other independent methods and the kinetics correspond to the results obtained through other conventional laboratory experiments.

On the basis of our present knowledge the following improvements of the developed technique can be proposed:

- A better isolation of the thermostatic deposition cell from the rest of the instrument. Inspiration can be taken from methods like FTIR, where the measurement cell is isolated and independent from the detection unit, light source and hardware of the apparatus. This may allow heating the OWLS cell even above 90°C.
- There is room to reduce the duration of the heating and cooling periods. The design of the measurement cell can in fact be optimized to reduce the transition time needed for temperature adjustment.
- Consider to use as a waveguiding material other than the conventional one based on titania-silica mixture. Some polymers have also the ability to guide light. Despite of the higher losses of the guided light intensity, the polymer materials may provide interesting features related to their different chemical properties. In particular they would allow overcoming the various problems related to the sensor sensitivity to the change in electrolyte concentration.
- Currently produced waveguides contain a significant amount of micropores. The reduction of such porosity would reduce the accessible waveguide surface, and thus all the side effects related to the interaction with the electrolytes. It is known that microporosity of the titania-silica mixtures can be significantly reduced by annealing it above 800°C, while the current waveguides are treated only at 500°C.

Nomenclature

a	radius of interacting colloid
A_{HAM}	Hamaker constant
C	liquid bulk
c	concentration
D	diffusion coeficient
d_p	penetration depth
e	electron charge
F	waveguide film
g	gravitational acceleration
h	surface to surface separation distance
H	height
I	intensity of scattered light
IEP	isoelectric point
k_B	Boltzman constant
l	diffraction order
L	length
M	mass
N	effective refractive index
n	refractive index
$N(TE)$	effective refractive index for transverse electric mode
$N(TM)$	effective refractive index for transverse magnetic mode
n_A	refractive index of deposit
n_{air}	refractive index of air
n_C	refractive index of liquid bulk
n_{C,H_2O}	refractive index of water
$n_{C,Extract}$	refractive index of coffee extract
n_F	refractive index of waveguide film
n_S	refractive index of waveguide substrate
OWLS	optical waveguide lightmode spectroscopy
$P(q)$	form factor
PEG-3.5-(PLL)	poly(ethylene glycol)-3.5-poly(L-lysine)
PS	polystyrene
q	scattering vector amplitude
Re	Reynolds number
R_g	root mean square radius of gyration
S	substrate
$S(q)$	structure factor
SEM	scanning electron microscopy
SLS	static light scattering
T	absolute temperature
t_F	thickness of waveguide film
v	liquid velocity
V_A	van der Walls interaction potential energy
V_R	electrical double layer repulsion energy
V_T	total interaction potential energy
W	width

x_E	weight concentration of solid content in coffee extract suspension
z_i	valence of ion i
α	incoupling incidence angle of a laser beam
αi	electronic polarizability
δ	thickness of free falling film
ε	dielectric constant
ε_0	permittivity of free space
$\Phi_{F,S}$	phase shifts upon reflection from interface F,S
$\Phi_{F,C}$	phase shifts upon reflection F,C
γ	surface excess polarization density
φ_0	surface potential
φ	electrical potential
κ	Debye-Hückel parameter
λ_0	wavelength of laser beam in vacuum
Λ	grating period
μ	dynamic viscosity
θ	scattering angle
ρ	volume charge density or liquid density
$\tau_{x,y}$	shear force per unit area

List of Used Chemicals

Sodium hydroxide solution, concentration 0.1M, from MERCK, (Lot. No. 0C182488)
Hydrochloric Acid, analytical grade, concentration 37%, from MERCK, (Lot. No. K27791817 019)
Tetrapropylammonium bromide, from Aldrich, (Lot. No. 06712ES)
Sodium Dodecyl Sulfate, from Fluka, (Lot. No. 410767/1)
Tetrapropylammoniumhydroxide, concentration 1M, from Aldrich, (Lot. No. S00363-021)
Magnesium chloride hexahydrate, from Fluka, (Lot. No. 399432/1)
Hexamethyldisilazane, from Fluka, (Lot. No. 427155/1 44601)
Polystyrene Standard 30 000, from Fluka, (Lot. No. 440166/1 12802)
HEPES, 99%, from ACROS ORGANICS, (Lot. No. A019289801)
β-lactoglobulin from bovine milk, from Fluka, (Lot. No. 1087564 51904191)
Sodium Chloride, from J.T. Baker, (Lot. No. 0213310006)
Toluene, from J.T. Baker, (Lot. No. 0100410001)
TEFLON AF®, from DuPont, type 1601
perfluortributylamine from DuPont (type AF)

Bibliography

1. Derjaguin, B.V. and L.D. Landau, *Theory of the stability of strongly charged lyophobic sols and of the adhesion of strongly charged particles in solutions of electrolytes.* Acta Physicochim. URSS, 1941. **14**: p. 733-762.

2. Verwey, E. and J. Overbeek, *Theory of the stability of lyophobic colloids, the interaction of sol particles having an electric double laye*, ed. Elsevier. 1948, Amsterdam.

3. Hamaker, H.C., *The London-van der Waals Attraction Between Spherical Particles.* Physica, 1937. **4**: p. 1058-1072.

4. Lifshitz, E.M., *Theory of molecular attractive forces.* Soviet Phys. JETP, 1956. **2**: p. 73-83.

5. Elimelech, M., et al., *Particle Deposition & Aggregation*. Colloid and Surface Engineering, ed. P.R.A. Williams. 1995, Exter, UK.

6. Hunter, R.J., *Foundations of Colloid Science*, ed. O.U. Press. 2001: Oxford University Press.

7. Israelachvili, j.N., *Intermolecular and Surface Forces*. 1992, London: Academic Press Limited.

8. Litton, G.M. and T.M. Olson, *Particle size effects on colloid deposition kinetics: Evidence of secondary minimum deposition.* Colloids and Surfaces a-Physicochemical and Engineering Aspects, 1996. **107**: p. 273-283.

9. Litton, G.M. and T.M. Olson, *Colloid Deposition Rates on Silica Bed Media and Artifacts Related to Collector Surface Preparation Methods.* Environmental Science & Technology, 1993. **27**(1): p. 185-193.

10. Vaidyanathan, R. and C. Tien, *Hydrosol Deposition in Antigranulocytes Media under Unfavorable Surface Conditions.* Chemical Engineering Science, 1991. **46**(4): p. 967-983.

11. Elimelech, M. and C.R. Omelia, *Kinetics of Deposition of Colloidal Particles in Porous-Media.* Environmental Science & Technology, 1990. **24**(10): p. 1528-1536.

12. Elimelech, M. and C.R. Omelia, *Effect of Particle-Size on Collision Efficiency in the Deposition of Brownian Particles with Electrostatic Energy Barriers.* Langmuir, 1990. **6**(6): p. 1153-1163.

13. Sjollema, J. and H.J. Busscher, *Deposition of Polystyrene Latex-Particles toward Polymethylmethacrylate in a Parallel Plate Flow Cell.* Journal of Colloid and Interface Science, 1989. **132**(2): p. 382-394.

14. Tobiason, J.E. and C.R. Omelia, *Physicochemical Aspects of Particle Removal in Depth Filtration.* Journal American Water Works Association, 1988. **80**(12): p. 54-64.

15. Kallay, N., J.D. Nelligan, and E. Matijevic, *Particle Adhesion and Removal in Model Systems .6. Kinetics of Deposition of Hematite Particles on Steel.* Journal of the Chemical Society-Faraday Transactions I, 1983. **79**: p. 65-74.

16. Nelligan, J.D., N. Kallay, and E. Matijevic, *Particle Adhesion and Removal in Model Systems .5. Interpretation of the Kinetics of Particle Detachment.* Journal of Colloid and Interface Science, 1982. **89**(1): p. 9-15.

17. Gregory, J. and A.J. Wishart, *Deposition of Latex-Particles on Alumina Fibers.* Colloids and Surfaces, 1980. **1**(3-4): p. 313-334.

18. Bowen, B.D. and N. Epstein, *Fine Particle Deposition in Smooth Parallel-Plate Channels.* Journal of Colloid and Interface Science, 1979. **72**(1): p. 81-97.

19. Bowen, B.D., S. Levine, and N. Epstein, *Fine Particle Deposition in Laminar-Flow through Parallel-Plate and Cylindrical Channels.* Journal of Colloid and Interface Science, 1976. **54**(3): p. 375-390.

20. Fitzpatr, J. and L.A. Spielman, *Filtration of Aqueous Latex Suspensions through Beds of Glass Spheres.* Journal of Colloid and Interface Science, 1973. **43**(2): p. 350-369.

21. Hull, M. and Kitchene.Ja, *Interaction of Spherical Colloidal Particles with Planar Surfaces.* Transactions of the Faraday Society, 1969. **65**(563P): p. 3093-&.

22. Elimelech, M., *Effect of Particle-Size on the Kinetics of Particle Deposition under Attractive Double-Layer Interactions (Vol 164, Pg 190, 1994).* Journal of Colloid and Interface Science, 1994. **166**(1): p. 266-266.

23. Elimelech, M., *Kinetics of Capture of Colloidal Particles in Packed-Beds under Attractive Double-Layer Interactions.* Journal of Colloid and Interface Science, 1991. **146**(2): p. 337-352.

24. Adamczyk, Z., et al., *Enhanced Deposition of Particles under Attractive Double-Layer Forces.* Journal of Colloid and Interface Science, 1989. **130**(2): p. 578-587.

25. Semmler, M., J. Ricka, and M. Borkovec, *Diffusional deposition of colloidal particles: electrostatic interaction and size polydispersity effects.* Colloids and Surfaces a-Physicochemical and Engineering Aspects, 2000. **165**(1-3): p. 79-93.

26. Brange, J. and L. Langkjaer, *Chemical-Stability of Insulin .3. Influence of Excipients, Formulation, and pH.* Acta Pharmaceutica Nordica, 1992. **4**(3): p. 149-158.

27. Brange, J., et al., *Chemical-Stability of Insulin .1. Hydrolytic Degradation During Storage of Pharmaceutical Preparations.* Pharmaceutical Research, 1992. **9**(6): p. 715-726.

28. Sato, S., C.D. Ebert, and S.W. Kim, *Prevention of Insulin Self-Association and Surface-Adsorption.* Journal of Pharmaceutical Sciences, 1983. **72**(3): p. 228-232.

29. Relkin, P., *Thermal unfolding of beta-lactoglobulin, alpha-lactalbumin, and bovine serum albumin. A thermodynamic approach.* Critical Reviews in Food Science and Nutrition, 1996. **36**(6): p. 565-601.

30. Kessler, H.G. and H.J. Beyer, *Thermal-Denaturation of Whey Proteins and Its Effect in Dairy-Technology.* International Journal of Biological Macromolecules, 1991. **13**(3): p. 165-173.

31. Dannenberg, F. and H.G. Kessler, *Thermodynamic Approach to Kinetics of Beta-Lactoglobulin Denaturation in Heated Skim Milk and Sweet Whey.* Milchwissenschaft-Milk Science International, 1988. **43**(3): p. 139-142.

32. Anema, S.G. and A.B. McKenna, *Reaction kinetics of thermal denaturation of whey proteins in heated reconstituted whole milk.* Journal of Agricultural and Food Chemistry, 1996. **44**(2): p. 422-428.

33. Matsumura, Y., et al., *Competitive Adsorption of Alpha-Lactalbumin in the Molten Globule State.* Food Hydrocolloids, 1994. **8**(6): p. 555-566.

34. Nakanishi, K., T. Sakiyama, and K. Imamura, *On the adsorption of proteins on solid surfaces, a common but very complicated phenomenon.* Journal of Bioscience and Bioengineering, 2001. **91**(3): p. 233-244.

35. Jeurnink, T.J.M., P. Walstra, and C.G. deKruif, *Mechanisms of fouling in dairy processing.* Netherlands Milk and Dairy Journal, 1996. **50**(3): p. 407-426.

36. Santos, O., et al., *Effect of surface and bulk solution properties on the adsorption of whey protein onto steel surfaces at high temperature.* Journal of Food Engineering, 2006. **73**(2): p. 174-189.

37. Kosmulski, M., *Chemical properties of Material Surfaces*, ed. A. Hubbard. Vol. 102. 2001: Dekker.

38. Schubert, D.W., *Spin coating as a method for polymer molecular weight determination.* Polymer Bulletin, 1997. **38**(2): p. 177-184.

39. Extrand, C.W., *Spin-Coating of Very Thin Polymer-Films.* Polymer Engineering and Science, 1994. **34**(5): p. 390-394.

40. Hall, D.B., P. Underhill, and J.M. Torkelson, *Spin Coating of Thin and Ultrathin Polymer Films.* Polymer Engineering and Science, 1998. **38, No 12**: p. 2039-2045.

41. Shapovalov, V., V.S. Zaitsev, and Y. Strzhemechny, *Nanostructure formation in spin-cast polystyrene films.* Polymer International, 2000. **49**(5): p. 432-436.

42. Mattsson, J., J.A. Forrest, and L. Borjesson, *Quantifying glass transition behavior in ultrathin free-standing polymer films.* Phys. Rev. E, 2000. **62**: p. 5187.

43. Stamm, M., *Decay of Interface Correlation in Thin Polymer Films.* Macromolecules, 1988. **31(26)**: p. 9265-9272.

44. Rehse, N., C. Wang, and M. Hund, *Stability of thin polymer films on a corrugated substrate.* The European Physical Journal E, 2001. **4**: p. 69-76.

45. Fukao, K. and Y. Miyamoto, *Glass Transition Temperature and Dynamics of Alfa-proces in Thin Polymer Films.* Europhysics Letters, 1999. **46**(5): p. 649-654.

46. Fukao, K. and Y. Miyamoto, *Glass transitions and dynamics in thin polymer films: Dielectric relaxation of thin.* Phys. Rev. E 61, 2000: p. 1743.

47. Forrest, J.A. and J. Mattsson, *Reductions of the glass transition temperature in thin polymer films: Probing the.* Phys. Rev. E, 2000. **61**: p. R53.

48. Keddie, J.L. and R.A.L. Jones, *Glass Transition Behaviour in Ultra-Thin Polystyrene Films.* Israel Journal of Chemistry, 1995. **35**: p. 21-26.

49. Zhao, J.H., et al., *Thermal stress and glass transition of ultrathin polystyrene films.* Appl. Phys. Lett., 2000. **77**: p. 2843.

50. Mounir, E.S.A., A. Takahara, and T. Kajiyama, *Effecty of Chain End Group-Substrate Interaction on Surface Molecular Motion of Polystirene Ultrathin Films.* Polmer Journal, 1999. **31**(6): p. 550-556.

51. Ramsden, J.J., *Review of New Experimental-Techniques for Investigating Random Sequential Adsorption.* Journal of Statistical Physics, 1993. **73**(5-6): p. 853-877.

52. Malmsten, M., *Biopolymers at interfaces*. Surfactant Science Series, ed. A.T. Hubbard. 2003, Basel, Switzerland.

53. Adamczyk, Z., *Particle Deposition from Flowing Suspensions.* Colloids and Surfaces, 1989. **39**(1-3): p. 1-37.

54. Adamczyk, Z., et al., *Kinetics of particle deposition in the radial impinging-jet cell.* Journal of Colloid and Interface Science, 2001. **242**(1): p. 14-24.

55. Adamczyk, Z., P. Weronski, and E. Musial, *Particle adsorption under irreversible conditions: kinetics and jamming coverage.* Colloids and Surfaces a-Physicochemical and Engineering Aspects, 2002. **208**(1-3): p. 29-40.

56. Voros, J., *The density and refractive index of adsorbing protein layers.* Biophysical Journal, 2004. **87**(1): p. 553-561.

57. Semmler, M., et al., *Diffusional deposition of charged latex particles on water-solid interfaces at low ionic strength.* Langmuir, 1998. **14**(18): p. 5127-5132.

58. Tiefenthaler, K. and W. Lukosz, *Grating Couplers as Integrated Optical Humidity and Gas Sensors.* Thin Solid Films, 1985. **126**(3-4): p. 205-211.

59. Tiefenthaler, K. and W. Lukosz, *Integrated Optical Humidity and Gas Sensors.* Proceedings of the Society of Photo-Optical Instrumentation Engineers, 1984. **514**: p. 215-218.

60. Tiefenthaler, K., U. Keller, and W. Lukosz, *Integrated Optical Humidity and Gas Sensors.* Helvetica Physica Acta, 1984. **57**(6): p. 765-765.

61. Tiefenthaler, K. and W. Lukosz, *New Switching Effects in Planar Optical-Wave Conductors.* Helvetica Physica Acta, 1984. **57**(2): p. 289-289.

62. Seifert, M., et al., *An Integrated Optical Biosensor (Iobs).* Analytical Letters, 1986. **19**(1-2): p. 205-216.

63. Tiefenthaler, K. and W. Lukosz, *Sensitivity of Grating Couplers as Integrated-Optical Chemical Sensors.* Journal of the Optical Society of America B-Optical Physics, 1989. **6**(2): p. 209-220.

64. Lukosz, W. and K. Tiefenthaler, *Sensitivity of Integrated Optical Grating and Prism Couplers as (Bio)Chemical Sensors.* Sensors and Actuators, 1988. **15**(3): p. 273-284.

65. Nellen, P.M., K. Tiefenthaler, and W. Lukosz, *Integrated Optical Input Grating Couplers as Biochemical Sensors.* Sensors and Actuators, 1988. **15**(3): p. 285-295.

66. Nellen, P.M. and W. Lukosz, *Integrated Optical Input Grating Couplers as Direct Affinity Sensors.* Biosensors & Bioelectronics, 1993. **8**(3-4): p. 129-147.

67. Lukosz, W., et al., *Output Grating Couplers on Planar Optical Wave-Guides as Direct Immunosensors.* Biosensors & Bioelectronics, 1991. **6**(3): p. 227-232.

68. Lukosz, W., D. Clerc, and P.M. Nellen, *Input and Output Grating Couplers as Integrated Optical Biosensors.* Sensors and Actuators a-Physical, 1991. **25**(1-3): p. 181-184.

69. Lukosz, W., et al., *Output Grating Couplers on Planar Wave-Guides as Integrated Optical Chemical Sensors.* Sensors and Actuators B-Chemical, 1990. **1**(1-6): p. 585-588.

70. Nellen, P.M. and W. Lukosz, *Integrated Optical Input Grating Couplers as Chemosensors and Immunosensors.* Sensors and Actuators B-Chemical, 1990. **1**(1-6): p. 592-596.

71. Voros, J., et al., *Feasibility study of an online toxicological sensor based on the optical waveguide technique.* Biosensors & Bioelectronics, 2000. **15**(9-10): p. 423-429.

72. Widmer, M.R., et al., *Influence of polymer surface chemistry on frictional properties under protein-lubrication conditions: implications for hip-implant design.* Tribology Letters, 2001. **10**(1-2): p. 111-116.

73. Hook, F., et al., *A comparative study of protein adsorption on titanium oxide surfaces using in situ ellipsometry, optical waveguide lightmode spectroscopy, and quartz crystal microbalance/dissipation.* Colloids and Surfaces B-Biointerfaces, 2002. **24**(2): p. 155-170.

74. Voros, J., et al., *Optical grating coupler biosensors.* Biomaterials, 2002. **23**(17): p. 3699-3710.

75. Rezwan, K., et al., *Bovine serum albumin adsorption onto colloidal Al2O3 particles: A new model based on zeta potential and UV-vis measurements.* Langmuir, 2004. **20**(23): p. 10055-10061.

76. Dalsin, J.L., et al., *Protein resistance of titanium oxide surfaces modified by biologically inspired mPEG-DOPA.* Langmuir, 2005. **21**(2): p. 640-646.

77. Ramsden, J.J., *Concentration Scaling of Protein Deposition Kinetics.* Physical Review Letters, 1993. **71**(2): p. 295-298.

78. Kurrat, R., J.J. Ramsden, and J.E. Prenosil, *Kinetic-Model for Serum-Albumin Adsorption - Experimental-Verification.* Journal of the Chemical Society-Faraday Transactions, 1994. **90**(4): p. 587-590.

79. Ramsden, J.J., *Experimental Methods for Investigating Protein Adsorption- Kinetics at Surfaces.* Quarterly Reviews of Biophysics, 1994. **27**(1): p. 41-105.

80. Ramsden, J.J. and J.E. Prenosil, *Effect of Ionic-Strength on Protein Adsorption-Kinetics.* Journal of Physical Chemistry, 1994. **98**(20): p. 5376-5381.

81. Ramsden, J.J., G.I. Bachmanova, and A.I. Archakov, *Immobilization of proteins to lipid bilayers.* Biosensors & Bioelectronics, 1996. **11**(5): p. 523-528.

82. Kurrat, R., J.E. Prenosil, and J.J. Ramsden, *Kinetics of human and bovine serum albumin adsorption at silica-titania surfaces.* Journal of Colloid and Interface Science, 1997. **185**(1): p. 1-8.

83. Ramsden, J.J., *OWLS: A versatile technique for sensing with bioarrays.* Chimia, 1999. **53**(3): p. 67-71.

84. VandeVondele, S., J. Voros, and J.A. Hubbell, *RGD-Grafted poly-l-lysine-graft-(polyethylene glycol) copolymers block non-specific protein adsorption while promoting cell adhesion.* Biotechnology and Bioengineering, 2003. **82**(7): p. 784-790.

85. Spencer, N.D., et al., *Poly((L)-lysine)-G-poly(ethylene glycol) layers on metal-oxide surfaces.* Abstracts of Papers of the American Chemical Society, 2000. **219**: p. U559-U559.

86. Pasche, S., et al., *Effects of ionic strength and surface charge on protein adsorption at PEGylated surfaces.* Journal of Physical Chemistry B, 2005. **109**(37): p. 17545-17552.

87. Kenausis, G.L., et al., *Poly(L-lysine)-g-poly(ethylene glycol) layers on metal oxide surfaces: Attachment mechanism and effects of polymer architecture on resistance to protein adsorption.* Journal of Physical Chemistry B, 2000. **104**(14): p. 3298-3309.

88. Huang, N.P., et al., *Biotin-derivatized poly(L-lysine)-g-poly(ethylene glycol): A novel polymeric interface for bioaffinity sensing.* Langmuir, 2002. **18**(1): p. 220-230.

89. Huang, N.P., et al., *Poly(L-lysine)-g-poly(ethylene glycol) layers on metal oxide surfaces: Surface-analytical characterization and resistance to serum and fibrinogen adsorption.* Langmuir, 2001. **17**(2): p. 489-498.

90. Heuberger, M., T. Drobek, and J. Voros, *About the role of water in surface-grafted poly(ethylene glycol) layers.* Langmuir, 2004. **20**(22): p. 9445-9448.

91. Faraasen, S., et al., *Ligand-specific targeting of microspheres to phagocytes by surface modification with poly(L-lysine)-grafted poly(ethylene glycol) conjugate.* Pharmaceutical Research, 2003. **20**(2): p. 237-246.

92. Bearinger, J.P., et al., *Electrochemical optical waveguide lightmode spectroscopy (EC-OWLS): A pilot study using evanescent-field optical sensing under voltage control to*

monitor polycationic polymer adsorption onto indium tin oxide (ITO)-coated waveguide chips. Biotechnology and Bioengineering, 2003. **82**(4): p. 465-473.

93. Brusatori, M.A. and P.R. Van Tassel, *Biosensing under an applied voltage using optical waveguide lightmode spectroscopy.* Biosensors & Bioelectronics, 2003. **18**(10): p. 1269-1277.

94. Brusatori, M.A., Y. Tie, and P.R. Van Tassel, *Protein adsorption kinetics under an applied electric field: An optical waveguide lightmode spectroscopy study.* Langmuir, 2003. **19**(12): p. 5089-5097.

95. Horvath, R., et al., *Effect of patterns and inhomogeneities on the surface of waveguides used for optical waveguide lightmode spectroscopy applications.* Applied Physics B-Lasers and Optics, 2001. **72**(4): p. 441-447.

96. Harrick, N.J., *Internal Reflection Spectroscopy*, ed. I. John Wiley & Sons. 1996: Interscience Publishers.

97. Picart, C., et al., *Measurement of film thickness up to several hundreds of nanometers using optical waveguide lightmode spectroscopy.* Biosensors & Bioelectronics, 2004. **20**(3): p. 553-561.

98. Haarmans, M.T. and D. Bedeaux, *Optical-Properties of Thin-Films up to 2nd-Order in the Thickness.* Thin Solid Films, 1995. **258**(1-2): p. 213-223.

99. Mann, E.K., *Evaluating optical techniques for determining film structure: Optical invariants for anisotropic dielectric thin films.* Langmuir, 2001. **17**(19): p. 5872-5881.

100. Sorensen, C.M., *Light scattering by fractal aggregates: A review.* Aerosol Science and Technology, 2001. **35**(2): p. 648-687.

101. Adamczyk, Z. and T.G.M. Vandeven, *Particle Transfer to a Plate in Uniform-Flow.* Chemical Engineering Science, 1982. **37**(6): p. 869-880.

102. Bird, R.B., W.E. Stewart, and E.N. Lightfoot, *Transport Phenomena*, ed. I. John Wiley & Sons. 1960.

103. Hul, H.J. and J.W. Vanderhoff. *Clean Monodisperse Latexes as Model Colloids*. in *American Chemical Society Symposium on Polymer Colloids*. 1971. Illinois.

104. Piirma, I. and R. Chen, *Adsorption of ionic surfactants on latex particles.* Journal of Colloid and Interface Science, 1980. **74**: p. 90-102.

105. Turner, S.F. and S.M. Clarke, *Adsorption of Sodium Dodecyl Sulfate to a Polystyrene/Water Interface Studied by Neutron Reflection and Attenuated Total Reflection Infrared Spectroscopy.* Langmuir, 1999. **15**: p. 1017-1023.

106. Velegol, S.B. and B.D. Fleming, *Counterion Effect on Hexadecyltrimethylamonium Surfactant Asorption and Self Assembly on Silica.* Langmuir, 2000: p. 2458-2556.

107. Bolze, J., K.D. Horner, and M. Ballauff, *Adsorption of the nonionic surfactant Triton X-405 on polystyrene latex particles as monitored by small-angle x-ray scattering.* Langmuir, 1996. **12**(12): p. 2906-2912.

108. Haarmans, M.T.B., D., *Thin Solid Films.* 1995.

109. Stange, T.G., R. Mathew, and D.F. Evans, *Scanning Tunneling Microscopy and Atomic Force Microscopy Characterization of Polystyrene Spin-Coated onto Silicon Surfaces.* Langmuir, 1992: p. 920-926.

110. Sefcik, J., M. Kroslak, and M. Morbidelli, *Optical response of porous titania-silica waveguides to surface charging in electrolyte filled pores.* Helvetica Chimica Acta, 2002. **85**(10): p. 3508-3515.

111. Verduyn, M.A., *Aggregation of Polymer Particles in Emulsion*, in *Diss. ETH Nr. 13435*. 1999, ETH: Zurich.

112. Jung, K.Y. and S.B. Park, *Anatase-phase titania: preparation by embedding silica and photocatalytic activity for the decomposition of trichloroethylene.* Journal of Photochemistry and Photobiology a-Chemistry, 1999. **127**(1-3): p. 117-122.

113. Beck, C., et al., *Nature of active sites in sol-gel TiO2-SiO2 epoxidation catalysts.* Journal of Catalysis, 2001. **204**(2): p. 428-439.

114. Lukosz, W., *Integrated Optical Chemical and Direct Biochemical Sensors.* Sensors and Actuators B-Chemical, 1995. **29**(1-3): p. 37-50.

115. Innocenzi, P., et al., *Optical and surface properties of inorganic and hybrid organic-inorganic silica-titania sol-gel planar waveguides.* Journal of Non-Crystalline Solids, 1999. **259**: p. 182-190.

116. Bradshaw, J.T., S.B. Mendes, and S.S. Saavedra, *A simplified broadband coupling approach applied to chemically robust sol-gel, planar integrated optical waveguides.* Analytical Chemistry, 2002. **74**(8): p. 1751-1759.

117. Brinker, C.J. and G.W. Scherer, *Sol-Gel Science*. 1990, San Diego: Academic Press.

118. Heuberger, K. and W. Lukosz, *Embossing Technique for Fabricating Surface Relief Gratings on Hard Oxide Wave-Guides.* Applied Optics, 1986. **25**(9): p. 1499-1504.

119. Nellen, M., *Integrated Optical Input Grating Couplers as Direct Chemo and Biosensors*. 1992, ETHZ: Zurich.

120. Ramsden, J.J., *Porosity of Pyrolyzed Sol-Gel Wave-Guides.* Journal of Materials Chemistry, 1994. **4**(8): p. 1263-1265.

121. Seco, A.M., M.C. Goncalves, and R.M. Almeida, *Densification of hybrid silica-titania sol-gel films studied by ellipsometry and FTIR.* Materials Science and Engineering B-Solid State Materials for Advanced Technology, 2000. **76**(3): p. 193-199.

122. Picart, C., et al., *Determination of structural parameters characterizing thin films by optical methods: A comparison between scanning angle reflectometry and optical*

waveguide lightmode spectroscopy. Journal of Chemical Physics, 2001. **115**(2): p. 1086-1094.

123. Calonder, C., Y. Tie, and P.R. Van Tassel, *History dependence of protein adsorption kinetics.* Proceedings of the National Academy of Sciences of the United States of America, 2001. **98**(19): p. 10664-10669.

124. *Handbook of Chemistry and Physics*. 81 ed, ed. R.L. David. 2000-2001.

125. Pyper, N.C., C.G. Pike, and P.P. Edwards, *The Polarizabilities of Species Present in Ionic-Solutions.* Molecular Physics, 1992. **76**(2): p. 353-372.

126. Behrens, S.H. and D.G. Grier, *The charge of glass and silica surfaces.* Journal of Chemical Physics, 2001. **115**(14): p. 6716-6721.

127. Iler, R.K., *The Chemistry of Silica*, ed. I. John Wiley & Sons. 1979.

128. Bourikas, K., T. Hiemstra, and W.H. Van Riemsdijk, *Ion pair formation and primary charging behavior of titanium oxide (anatase and rutile).* Langmuir, 2001. **17**(3): p. 749-756.

129. Goutev, N., Z.S. Nickolov, and J.J. Ramsden, *Waveguide Raman spectroscopy of Si(Ti)O-2 thin films with grating coupling.* Journal of Raman Spectroscopy, 1996. **27**(12): p. 897-900.

130. Laligant, A., et al., *Surface Hydrophobicity and Aggregation of Beta-Lactoglobulin Heated near Neutral pH.* Journal of Agricultural and Food Chemistry, 1991. **39**(12): p. 2147-2155.

131. Monahan, F.J., J.B. German, and J.E. Kinsella, *Effect of pH and Temperature on Protein Unfolding and Thiol-Disulfide Interchange Reactions During Heat-Induced Gelation of Whey Proteins.* Journal of Agricultural and Food Chemistry, 1995. **43**(1): p. 46-52.

132. Liu, T.X., P. Relkin, and B. Launay, *Thermal-Denaturation and Heat-Induced Gelation Properties of Beta-Lactoglobulin - Effects of Some Chemical-Parameters.* Thermochimica Acta, 1994. **246**(2): p. 387-403.

133. Baussay, K., et al., *Influence of the ionic strength on the heat-induced aggregation of the globular protein beta-lactoglobulin at pH 7.* International Journal of Biological Macromolecules, 2004. **34**(1-2): p. 21-28.

134. Pouzot, M., D. Durand, and T. Nicolai, *Influence of the ionic strength on the structure of heat-set globular protein gels at pH 7. beta-lactoglobulin.* Macromolecules, 2004. **37**(23): p. 8703-8708.

135. Tobitani, A. and S.B. RossMurphy, *Heat-induced gelation of globular proteins .1. Model for the effects of time and temperature on the gelation time of BSA gels.* Macromolecules, 1997. **30**(17): p. 4845-4854.

136. Le Bon, C., T. Nicolai, and D. Durand, *Kinetics of aggregation and gelation of globular proteins after heat-induced denaturation.* Macromolecules, 1999. **32**(19): p. 6120-6127.

137. Sava, N., et al., *The kinetics of heat-induced structural changes of beta-lactoglobulin.* Journal of Dairy Science, 2005. **88**(5): p. 1646-1653.

138. Anema, S.G., *Effect of milk concentration on the irreversible thermal denaturation and disulfide aggregation of beta-lactoglobulin.* Journal of Agricultural and Food Chemistry, 2000. **48**(9): p. 4168-4175.

139. Galani, D. and R.K.O. Apenten, *Heat-induced denaturation and aggregation of beta-Lactoglobulin: kinetics of formation of hydrophobic and disulphide-linked aggregates.* International Journal of Food Science and Technology, 1999. **34**(5-6): p. 467-476.

140. Tolkach, A. and U. Kulozik, *Effect of pH and temperature on the reaction kinetic parameters of the thermal denaturation of beta-lactoglobulin.* Milchwissenschaft-Milk Science International, 2005. **60**(3): p. 249-252.

141. de la Fuente, M.A., H. Singh, and Y. Hemar, *Recent advances in the characterisation of heat-induced aggregates and intermediates of whey proteins.* Trends in Food Science & Technology, 2002. **13**(8): p. 262-274.

142. Hoffmann, M.A.M. and P. vanMil, *Heat-induced aggregation of beta-lactoglobulin: Role of the free thiol group and disulfide bonds.* Journal of Agricultural and Food Chemistry, 1997. **45**(8): p. 2942-2948.

143. Gotham, S.M., P.J. Fryer, and A.M. Pritchard, *Beta-Lactoglobulin Denaturation and Aggregation Reactions and Fouling Deposit Formation - a Dsc Study.* International Journal of Food Science and Technology, 1992. **27**(3): p. 313-327.

144. Elofsson, U.M., et al., *Adsorption during heat treatment related to the thermal unfolding aggregation of beta-lactoglobulins A and B.* Journal of Colloid and Interface Science, 1996. **183**(2): p. 408-415.

145. Van Tassel, P.R., *Statistical mechanical modeling of protein adsorption.* Materialwissenschaft Und Werkstofftechnik, 2003. **34**(12): p. 1129-1132.

146. Szollosi, G.J., I. Derenyi, and J. Voros, *Reversible mesoscopic model of protein adsorption: From equilibrium to dynamics.* Physica a-Statistical Mechanics and Its Applications, 2004. **343**: p. 359-375.

147. Saini, S., et al., *Temperature-Dependence of Pyrolyzed Sol-Gel Planar Wave-Guide Parameters.* Journal of Physics D-Applied Physics, 1994. **27**(6): p. 1134-1138.

148. MicroVacuum, *OWLS Biosence 2.2 Software Database*. 2003: Budapest, Hungary.

149. Hoffmann, M.A.M., et al., *Aggregation of beta-lactoglobulin studied by in situ light scattering.* Journal of Dairy Research, 1996. **63**(3): p. 423-440.

150. Verheul, M., S. Roefs, and K.G. de Kruif, *Kinetics of heat-induced aggregation of beta-lactoglobulin.* Journal of Agricultural and Food Chemistry, 1998. **46**(3): p. 896-903.

151. Law, A.J.R. and J. Leaver, *Effect of pH on the thermal denaturation of whey proteins in milk.* Journal of Agricultural and Food Chemistry, 2000. **48**(3): p. 672-679.

152. Vonhippe, P. and T. Schleich, *Ion Effects on Solution Structure of Biological Macromolecules.* Accounts of Chemical Research, 1969. **2**(9): p. 257-&.

153. Bailey, J.E., *Biochemical-Engineering Fundamentals*, ed. M.-H.B. Co. 1986, Singapore.

154. Lavalle, P., et al., *Modeling the buildup of polyelectrolyte multilayer films having exponential growth.* Journal of Physical Chemistry B, 2004. **108**(2): p. 635-648.

155. Griesser, H.J., et al., *Interfacial properties and protein resistance of nano-scale polysaccharide coatings.* Smart Materials & Structures, 2002. **11**(5): p. 652-661.

156. Changani, S.D., M.T. BelmarBeiny, and P.J. Fryer, *Engineering and chemical factors associated with fouling and cleaning in milk processing.* Experimental Thermal and Fluid Science, 1997. **14**(4): p. 392-406.

157. Jong, P., *Impact and Control of Fouling in Milk Processing.* Trends in Food Science & Technology, 1997. **8**: p. 401-405.

158. Visser, J. and T.J.M. Jeurnink, *Fouling of heat exchangers in the dairy industry.* Experimental Thermal and Fluid Science, 1997. **14**(4): p. 407-424.

159. Huang, N.-P., *Biochemical Interactions of Surface-Bound PEG Copolymers*. 2002, ETHZ: Zurich.

160. Defeijter, J.A., J. Benjamins, and F.A. Veer, *Ellipsometry as a Tool to Study Adsorption Behavior of Synthetic and Biopolymers at Air-Water-Interface.* Biopolymers, 1978. **17**(7): p. 1759-1772.

161. Le Bon, C., T. Nicolai, and D. Durand, *Growth and structure of aggregates of heat-denatured beta-Lactoglobulin.* International Journal of Food Science and Technology, 1999. **34**(5-6): p. 451-465.

162. Burchard, W., *Structure formation by polysaccharides in concentrated solution.* Biomacromolecules, 2001. **2**(2): p. 342-353.

163. Redgwell, R.J., et al., *Hydrocolloids from coffee: physicochemical and functional properties of an arabinogalactan-protein fraction from green beans.* Food Hydrocolloids, 2005. **19**(6): p. 1005-1015.

Curriculum Vitae

Marek Kroslak

1976	Born on December, 5th , Bratislava, Slovakia.
1991-1995	Secondary Grammar School, Bratislava, Slovakia.
1995-1998	Slovak University of Technology, Bratislava, Slovakia, Bachelor's degree in Chemical Engineering.
1998-2000	Slovak University of Technology, Bratislava, Slovakia, Department of Chemical and Biochemical Engineering, M.Sc. degree in Chemical Engineering and Management of Processes.
2001-present	Doctoral studies at the Institute of Chemical and Bioengineering, Swiss Federal Institute of Technology (ETH), Zurich, Switzerland.

Publications

Klein J, Rosenberg M, Markoš J, Dolgoš O, Krošlák M and Krištofíková Ľ: *Biotransformation of glucose to gluconic acid by Aspergillus niger - study of mass transfer in an airlift bioreactor*. Biochemical Engineering Journal, 2002. **10**(3): p. 197-205.

Sefcik J, Kroslak M, Morbidelli M: *Optical response of porous titania-silica waveguides to surface charging in electrolyte filled pores*, Helvetica Chimica Acta, 2002. **85**(10): p. 3508-3515.

Kroslak M, Sefcik J, Morbidelli M: Effect of temperature, pH and salt concentration on β-lactoglobulin deposition kinetics studied by optical waveguide lightmode spectroscopy. Submitted to Biomacromolecules.

Kroslak M, Sefcik J, Liardon R, Morbidelli M: Investigation of thermally induced deposition from coffee extracts using optical waveguide lightmode spectroscopy. Submitted to Food Hydrocolloids.

Presentations

SSCHI 2000 Dolgos O, Klein J, Kroslak M, Rosenberg M, Markos J: Fermentation Produced Gluconic Acid in Airlift Bioreactors, Poster section, SSCHI, Tatranske Matliare, 2000

SSCHI 2001 Kroslak M, Sefcik J, Morbidelli M: On-line Monitoring of Adsorption and Desorption Using Optical Waveguide Lightmode Spectroscopy, Tatranske Matliare, May 21 – 25, 2001, Oral Presentation

AICHE 2001 Kroslak M, Sefcik J, Morbidelli M: Monitoring Adsorption and Desorption Using Optical Waveguide Lightmode Spectroscopy, ETH Zurich, AICHE-Reno, November 4-9 2001, Oral Presentation

SSCHI 2002 Kroslak M, Sefcik J, Morbidelli M: Charging of Aqueous Silica Surfaces Studied by Optical Waveguide Lightmode Spectroscopy, Tatranske Matliare, May 2002, Oral Presentation

ECIS 2002 Kroslak M, Sefcik J, Morbidelli M: Adsorption of Surfactant on Polymeric Film Monitored By Optical Waveguide Lightmode Spectroscopy, Poster Section, Paris, September 2002

ECIS 2003 Kroslak M., Sefcik J., Morbidelli M.: Surface Interactions and Ion Transport in Electrolyte Filled Nanopores, Poster Section, Florence, September 2003

SSCHI 2004 Kroslak M, Sefcik J, Morbidelli M: Measurements of Adsorption Isotherms and Adsorption Kinetics by Interfacial Spectroscopy, Tatranske Matliare, May 2004, Oral Presentation